# Differential Reactivity at Edge and Terrace Sites of Transition Metal Dichalcogenides

Thesis by

Joshua David Wiensch

In Partial Fulfillment of the Requirements for

the degree of

Doctor of Philosophy


CALIFORNIA INSTITUTE OF TECHNOLOGY

Pasadena, California

2017

(Defended February 15, 2017)

Joshua D. Wiensch
ORCID: 0000-0002-8235-6937

# Acknowledgements

First, I would like to thank my advisor, Nate, for welcoming me into his lab and for providing the freedom to chart my own course with my research. I have learned a tremendous amount from simply being an active member of the Lewis group. Nate, you do great science but what makes you special, and what I most want to emulate is how you value people. You value the science, unquestionably, but you also work hard to help people along the way and build strong connections within the community. Thank you for being supportive of me and of all your students.

My committee members, Harry Gray, Bob Grubbs, and Jonas Peters have been wonderfully supportive of me throughout my studies at Caltech. My committee meetings with all of you were consistently positive and supportive and I always left with great ideas and a renewed sense of vigor regarding my research. For this, I am grateful.

I would also like to say thank you to Theodore Agapie for the education you provided me while I was a part of your research group. I regard highly your continuing pursuit for greatness and the scientific excellence you demand from your students. Specifically, the respect for synthetic rigor I gained will serve me well into my career.

I am indebted to all of the graduate students who have contributed directly to my research projects, including Azhar Carim, Jimmy John, Adam Pieterick, Ellen Yan, and Victoria Dix. Additionally, Ron Grimm helped me get started in the Lewis group. Without him, I probably would have gotten off to a much slower start.

Both in and out of the lab, I was lucky to have many amazing friends and colleagues. Adam Nielander, thank you for the help in the laboratory as well as on the basketball court. Guy Edouard, thank you for being a good friend, teammate, and general partner in crime. To Jon Rittle, Justin Henthorn, and Kyle Horak, thanks for being good roommates. I hope we cross paths again soon. To all of the past and present members of the Caltech ultimate team, I spent way, way too much time and had excessive fun playing ultimate while at Caltech. Thank you all for being a part of that experience. Another thank you to the members of Skylife and the rest of the Pasadena ultimate crew.

Annelise Thompson, thank you for taking the helm of safety officer and for working so hard to prevent Noyes lab from becoming the jungle it would otherwise become. To Bruce Brunschwig, your insights into surface science have been very helpful. Thanks for always having great suggestions ready to help whenever I hit a roadblock. Thanks to Dan Torelli for being a great captain of Cold Fusion, and to all my teammates, thank you. To Barbara Miralles, thank you for keeping the Lewis group running. Your hard work is critical to the functioning of the group. To Kimberly Papadantonakis, thank you for helping to guide the group in the right direction.

Thank you to all members of the Lewis group, past and present who have had an effect on my time at Caltech. In no particular order, Mike Lichterman, Chance Crompton, JingJing Jiang, Ke Sun, Miguel Caban-Acevedo, Sisir Yalamanchili, Xinghao Zhou, Ethan Simanoff, Jonathan Thompson, Fadl Saadi, Katherine Rinaldi, Noah Plymale, Stefan Omelchenko, Paul Nunez, Ivan Moreno-Hernandez, Kyra Lee, Paul Kempler, Bryce Sadtler, Joseph Beardslee, Shane Ardo, Rob Coridan, Mita Dasog, Betar Gallant, Shu Hu, Matt McDowell, James McKone,

Chris Roske, Matt Shaner, Amanda Shing, Jesus Velazquez, Craig Wiggenhorn, and Keith Wong thanks to all of you for making the Lewis group what it is.

Thank you to my former colleagues in the Agapie group with whom I spent many good times: Dave Herbert, Madalyn Radlauer, Davide Lionetti, Sibo Lin, Jacob Kanady, Sandy Suseno, Paul Kelley, Emily Tsui, Josh Buss, Aya Buckley, Steven Chao, Christine Cheng, Nadia Lara, and Eva Nichols.

Thank you to my Mom and Dad, Julie and Dave Wiensch for always being loving and encouraging, and for supporting me in my decision to go to graduate school even when none of us really understood what I was getting myself into. Thank you to Eric Wiensch for being a great friend, hiking companion, video game partner, and overall fantastic brother. I hope the lessons I learned in graduate school can help you while you are in your PhD studies at Michigan.

Lastly, but certainly not least, I would like to thank my loving wife and partner, Qiao Li. You are the best companion and a wonderfully supportive spouse. Thank you for being there for me during the best times as well as lowest moments in graduate school. I look forward to all of the adventures we have yet to face together.

# Abstract

Humanity in the 21st century faces a challenge never before faced in the history of civilization. Either because of climate changing $CO_2$ emissions or because of the fundamental limits to the availability of fossil fuels, humanity needs to shift from a predominantly fossil fueled society to one powered mostly by renewable sources. Sunlight presents itself as the only renewable resource with the necessary abundance to enable the transition from fossil fuels to renewables. Modern photovoltaic technologies are highly efficient but do not readily enable the storage of electricity for use when the sun does not shine. Therefore, inexpensive and efficient methods for storing solar energy in a dense, easily transported medium are needed if the sun is going to provide the majority of humanities energy demands.

This dissertation describes efforts towards understanding the surface reactivity and catalytic properties of a promising class of materials, which have the potential to be integrated as part of a solar-fuels device and help usher-in the solar age. Because of their multifunctional behavior, transition metal dichalcogenides are potential candidates for not only light absorption in a solar fuels device, but also as catalysts for the hydrogen evolution reaction.

We begin in chapter one with an introduction related to global energy sources and trends, highlighting the motivation for the work performed in this dissertation. The second chapter describes a discovery into the interplay of pH and morphology for the hydrogen evolution reaction on $MoSe_2$. This discovery suggested a possibility for a different mechanism for the hydrogen evolution reaction being active in acidic and alkaline media. The third chapter describes an exploration into selective small molecule binding to macroscopic edge sites of $MoSe_2$ and $WSe_2$. The fourth chapter is a study of the protective effects of ALD-$TiO_2$ when

grown on a variety of $MX_2$'s. The inert nature of terrace sites in $MoSe_2$ and other $MX_2$'s prevented the growth of a conformal thin film of $TiO_2$ but yielded nanoparticles on the surface instead. Finally, in appendix A, I describe the work performed prior to joining the Lewis group relating to the design and synthesis of a binuclear titanium complex that was explored for its ability to copolymerize olefins and enable the incorporation of polar monomers.

# Published Content and Contributions

Radlauer, M., **Wiensch, J. D**., Buckley, A. K., Agapie, T., (2016) "Multi-metallic organometallic complexes, and related polymers, compositions, methods and systems" United States Patent 9,233,996 B2, Issued Jan. 12 2016. URL: https://patents.google.com/patent/US9233996B2/en

J.D.W participated in the conception of the project, synthesized several of the ligands and organometallic complexes, collected data, and participated in the writing of the patent.

**Wiensch, J. D**.; John, J.; Velazquez, J. M.; Pieterick, A.; McDowell, M. T.; Chatman, S.; Sun, K.; Saadi, F.; Zhao, X.; Soriaga, M.P.; Brunschwig, B. S.; Lewis, N. S. (2017). "A Comparative Study in Acidic and Alkaline Media of the Interplay of pH and Surface Morphology on the Hydrogen-Evolution Reaction on $MoS_2$ and $MoSe_2$" *In Preparation.*

J.D.W prepared $MoSe_2$ samples, collected and analyzed electrochemistry and characterization data, and co-wrote the manuscript with J. John.

# Contents

# List of Figures

**C h a p t e r 1**

# 1. Introduction

## 1.1. Global Energy Use

Certainly, civilization runs on energy. All preindustrial societies derived their energy from sources that were transformations of solar radiation in which the energy is harnessed almost immediately after solar influence. For example, harnessing wind is equivalent to harnessing the transformation of solar radiation from hours or days prior. Other preindustrial energy sources such as animal and human prime movers could be produced after several years of metabolism. Fossil fuel sources, in contrast, have times-to-availability which are many orders of magnitude longer than for other preindustrial energy sources. Figure 1.1 highlights the typical time to availability of various energy sources.

| Energy Source | Typical time to availability/ years |
|---|---|
| wind | < 1 |
| flowing water | < 1 |
| food crops | ~ 1 |
| domestic animals | 2-5 |
| human metabolism | 10-20 |
| phytomass accumulation | 50 |
| coal | $10^8$ |
| oil | $10^7$-$10^8$ |
| natural gas | $10^7$-$10^8$ |

Figure 1.1 Time separation between solar radiation influence and when it becomes available in a convenient form.

Postindustrial energy has come almost entirely from fossil fuel sources. In essence, while preindustrial societies relied on nearly instantaneous solar energy equivalents for use,

modern civilization is withdrawing from a stored account of solar energy at rates far faster than the rate of replenishment. Meanwhile, economic productivity is intimately connected to energy use and humanity is utterly dependent on energy sources that are fundamentally limited on the civilization timescale. The US energy information administration projects a global increase in energy use by 48 percent between 2012 and 2040 as seen in Figure 1.2.[1] Although renewable energy is the fastest-growing source of energy, at a rate of 2.6 percent per year, fossil fuels continue to provide most of the world's energy.

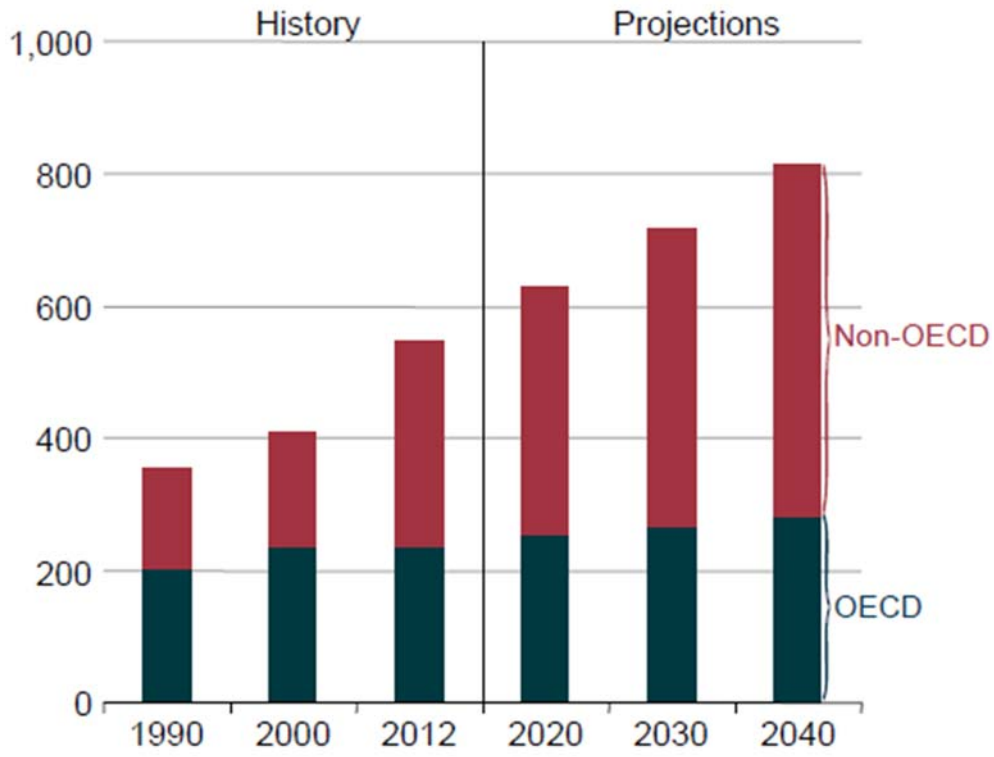


Figure 1.2 World energy consumption in quadrillion Btu, 1990-2040. Publicly available from US energy information administration[1]

A useful metric to estimate the lifetime of proven energy reserves can be done by taking the global ratio of proven reserves of a fuel to its annual production. This gives a rough estimate of how many years of current production could be supported by proven reserves.

Globally, for oil, proven reserves are 1.6976 trillion barrels and with production of ~ 92 million barrels per day the R/P ratio is 50.7.[2] It's important to point out that this value does not indicate the amount of time before humanity runs out of oil. Globally, the R/P ratio has remained relatively constant for decades as a result of the discovery of new reserves. However, most reserve increases in recent years have come from updated estimates from current oil fields and not new oil field discoveries.

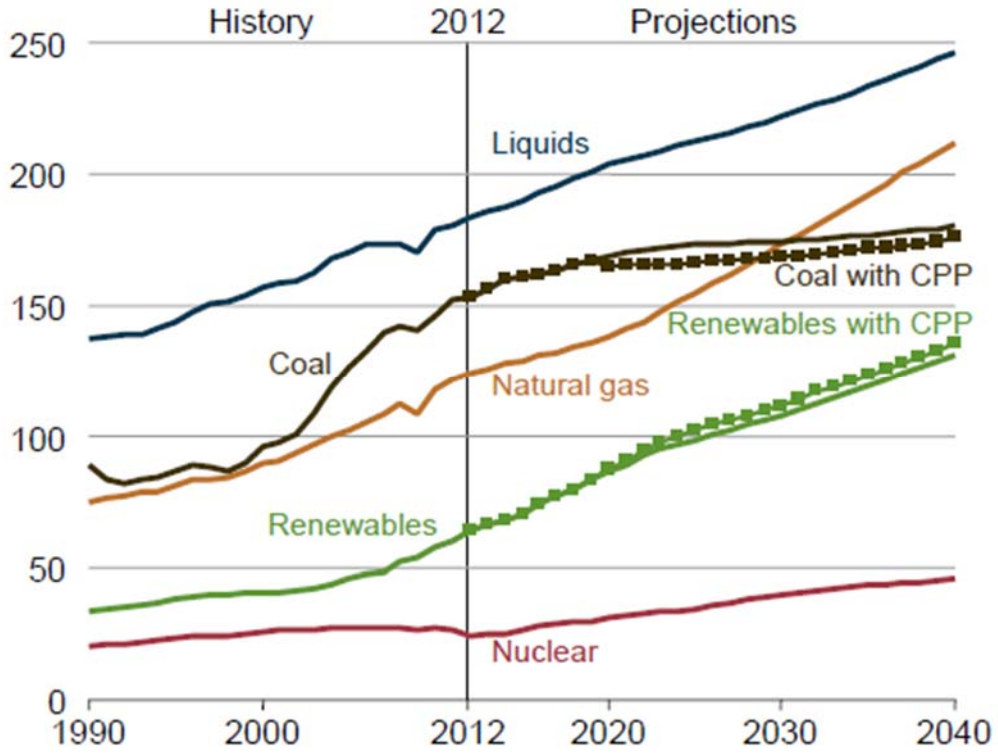


Figure 1.3 World energy consumption by energy source in quadrillion Btu, 1990-2040. Publicly available from US energy information administration[1]

Figure 1.3 shows worldwide energy consumption by fuel type from 1990 and projected to the year 2040. Fossil fuels currently dominate global energy consumption with 80 percent of all marketable energy coming from fossil fuels. This is expected to continue for decades and the US EIA projects that in 2040 fossil fuels will account for 78 percent of

global energy consumption. The anthropogenic carbon dioxide emissions associated with the consumption of fossil fuels was 32.3 billion metric tons in 2012 and is expected to rise to 35.6 billion metric tons in 2020 and reach 43.2 billion metric tons in 2040.[1] The majority of increased fossil fuel consumption and associated $CO_2$ emission is expected to come from developing nations outside the Organization for Economic Cooperation and Development (OECD), many of which continue to rely heavily on fossil fuels to meet the fast-paced growth of energy demand.

### 1.2. Climate Change

In its fifth report in 2013, the intergovernmental panel on climate change (IPCC) reported as a certainty that global mean surface temperature (GMST) has increased since the late 19$^{th}$ centrury.[3] The globally averaged combined land and ocean temperature data show a warming of 0.85 °C, over the period of 1880-2012. The cause of this warming is almost certainly anthropogenic radiative forcing, the bulk of which is the result of well mixed greenhouse gases such as $CO_2$ and methane. The radiative forcing of all well mixed greenhouse gases in 2011 is 2.83 W/m$^2$ with nearly all of the increase since 2005 due to an increase in the abundance of $CO_2$. When all anthropogenic radiative forcing agents such as aerosol-radiation interactions and surface albedo from land use change are included, total anthropogenic radiative forcing of climate between 1750 and 2011 is 2.25 W/m$^2$ with the lion's share of forcing coming from $CO_2$ emissions as a result of the combustion of fossil fuels.

There is a strong consensus in the global scientific communities that humans are causing a large and measureable change to the global climate of planet earth. With fossil fuel use predicted to continue to rise, and subsequent $CO_2$ emissions to rise 34% from 2012 to 2040, one can expect an increase in anthropogenic radiative forcing during this time. There is high confidence from the IPCC that the transient climate response to cumulative carbon emission is likely between 0.8 °C to 2.5 °C per 1000 petagrams of carbon (PgC).[3] For comparison, between 1750 and 2011, $CO_2$ emissions from fossil fuel combustion and cement production are estimated from energy and fuel use statistics to have released 375 PgC. During the same time period land use change emissions are estimated to have released 180 PgC.

The consequences of this increase in radiative forcing and global temperature rise have been studied as part of simple and complex climate models and the projections are largely dependent on the representative concentration pathways (RCPs) which are a set of four greenhouse gas concentration trajectories and are named after a possible range of radiative forcing values in the year 2100. The likely range of global mean surface temperature change from 2081-2100 is 1.1 °C - 3.1 °C for $RCP_{4.5}$. Global mean sea level rise corresponding to $RCP_{4.5}$ is likey 0.32 to 0.63 meters by 2100. Several other predicted phenomena are global lowering of ocean pH, a very likely continued decline in artic sea ice cover, and a virtual certainty that, in most places, there will be greater hot and fewer cold temperature extremes as global mean temperatures increase. What this ultimately means for humanity is uncertain. However, limiting cumulative total anthropogenic $CO_2$ emissions lowers the predicted mean surface temperature and related global climate effects. With this

knowledge, it is simple to see the benefits of increasing consumption of low-carbon or no carbon sources of energy.

### 1.3. Why Solar

There are many sources of low carbon energy from which to choose. Wind, tidal, geothermal, solar, and hydroelectric are all low to no carbon sources of energy. They are, however, not all created equal. Each source has a fundamental limit to its capacity and it is useful to compare these natural energy sources to the total primary energy supply (TPES), which was 14 terawatt years in 2006 and 17.5 terawatt years in 2011. Figure 1.4[4] shows how natural energy sources compare to the TPES from 2004.[4] It is clear that many of the natural sources can cover in theory the entirety of TPES. Upon closer inspection however, things are not as optimistic. Not all of the natural energy is readily accessible. We cannot absorb all of the wind without disastrous climate problems. Wind does not blow all of the time at any one place. If we use all of the photosynthesis, our environment would be decimated. Nearly all of the high quality hydroelectric power has already been installed and still only accounts for approximately 7% of the USs total energy production. Solar and potentially wind appear to be sources of energy which could supply the entirety of TPES without requiring the capture of a large portion of the total energy resource. Solar in particular stands out because its scale is greater than two orders of magnitude higher than the wind resource. Because of the sheer size of the solar resource, it has the potential to completely supply the world's energy needs.[5]

| Item | *Amount relative to TPES* |
|---|---|
| Total primary energy supply (TPES) | 1 |
| Solar input | 8000 |
| All the world's winds | 60 |
| All the ocean's waves | 4 |
| All the earths tides | 0.25 |
| Geothermal world potential | 2.3 |
| All photosynthesis | 6.5 |
| All the world's rivers | 0.5 |

Figure 1.4. Natural energy sources compared to the total primary energy supply of 2004

While the solar resource is massive, it is also spatially diffuse, with 170 W/m$^2$ of average solar power striking the earth's surface, compared to the richest oil fields, which can contain energy at 100 GJ/m$^2$.[5-6] If the well has a lifetime of 10 years, this comes to an intensity of 317 W/m$^2$. However, the oil coming out of the ground possesses significant advantages over the solar resource. Oil is already a stored form of energy and can be transported by rail or pipeline when and to where it is needed. The solar resource needs to be captured for use and industry leading commercial photovoltaic efficiencies are approximately 20%.[7] In addition, solar power is only available during the day, and the best locations for capturing the solar energy resource are often in extreme deserts such as the Sahara and Mojave, where few people live. Thus, we need to develop methods to efficiently capture and store solar energy, allowing delayed use of solar resources at night and across vast geographic distances.

## 1.4. Energy Storage and Artificial Photosynthesis

One of the most promising methods for addressing the issue of solar intermittency is using large-scale energy storage. Some forms of large-scale energy storage are already utilized as part of the electric grid. In 2016, the US had approximately 24.1 GW of grid

storage corresponding to approximately 2.3% of total electric production capacity for the country.[8] Of the total storage capacity, 93.8% came in the form of pumped hydroelectric storage (PHES) in which water is pumped uphill with excess grid electricity when renewables such as solar and wind provide excess power. To retrieve the stored energy, the water passes through a hydroelectric generator. PHES is the least expensive energy storage method, because most of the infrastructure is already in place at hydroelectric plants. The round-trip efficiency of energy storage using pumped water hydroelectric storage is 70-80%.[9]

Several other forms of energy storage currently being used are electrochemical energy storage, thermal storage, and compressed air storage.[10] Electrochemical storage takes the form mostly as battery technologies such as lithium-ion batteries and advanced lead-acid batteries. Ideally, a solar energy storage method would enable the capture of incident photons in an efficient manner and then convert the captured energy economically into an energy-dense material that can be easily transported and stored for use on demand. No current methods meet all of these requirements. Although, PHES is the cheapest form of storage, it requires either very large reservoirs or large elevation variations between lower and upper reservoirs and the number of natural sites suitable for PHES is limited.[11]

Another intuitive method of solar energy storage involves using photovoltaic arrays to charge batteries. On a small scale, these systems are already in use. The world's largest battery storage installation is located in Fairbanks AK and can provide 40 MW of power for 7 minutes or 26 MW of power for 15 minutes thus storing 6.5 MW·hr of energy. A solar battery could in-theory be developed to fit any needed scale. However, when comparing

current grid-tied battery systems to the largest PHES, the Bath county pumped storage station, the differences in scale become very noticeable. The bath county pumped storage station has a power capacity of 3003 MW and can generate power for approximately 11 hours. Thus, it is capable of storing 33,033 MW·hr of energy. This is over 5000 times the capacity of the world's largest battery.[12]

Arrays of batteries from electric vehicles or for permanent residential use could be installed in homes and businesses and charged with rooftop solar modules. Even larger battery arrays could be installed in industrial and commercial settings and charged from grid-tied photovoltaics to provide energy as needed for businesses. Small scale electrochemical storage is already used to smooth the supply from intermittent renewable power sources at several locations in the USA and one can envision a battery deployment on a scale that would allow integration on the scale of PHES. Unfortunately, current battery technologies are not yet energy-dense or inexpensive enough to allow for deployment as a part of large scale storage even though the resource base can likely handle the short to mid-term demand for battery raw materials.[13]

| Storage Material | *Specific energy (MJ/kg)* | *Energy Density(MJ/L)* |
|---|---|---|
| Hydrogen (700 bar) | 142 | 5.6 |
| Methane | 55.5 | 0.0364 |
| Gasoline | 46.4 | 34.2 |
| Methanol | 19.7 | 15.6 |
| Lithium-ion battery | 0.875 | 2.63 |
| Lead-acid battery | 0.17 | 0.56 |
| Electrical capacitor | 0.00002 | 0.001 |

Figure 1.5. Comparison of selected energy storage materials.

Another method of solar energy storage is commonly known as "artificial photosynthesis," and it is the primary driver of the research reported in this dissertation. Artificial photosynthesis is a process intermediate between photovoltaics and natural photosynthesis.[14] In artificial photosynthesis, incident photons from the sun are absorbed by synthetic light absorbing materials to generate high-energy electronic states. Then, as in natural photosynthesis, energetic charge carriers are spatially separated to prevent recombination and are converted ultimately to stored chemical energy by way of endothermic chemical reactions. The advantage of artificial photosynthesis over photovoltaics is the ability to generate high energy density fuels that can be integrated into current fossil fuel infrastructure. Several energy storage materials are listed in Figure 1.5, where they are compared based on their accessible stored energy densities. Fossil fuels, particularly oil, have high specific energies and high energy densities. This is one reason oil has been adopted so thoroughly around the world as a transportation fuel. Methanol, a potential solar fuel and another liquid energy storage medium, is approximately within a factor of two of oil for energy content. Hydrogen, another solar fuel, possesses extremely high specific energy but modest energy density. Hydrogen as a solar fuel has shown the most potential and is closest to commercialization because of numerous laboratory demonstrations showing the promise of the technology. Direct methanol generation by artificial photosynthesis is much less well developed and requires significant investment into basic scientific research in order to become viable.

Nearly, all of the research in this dissertation is centered around a concept developed by my research advisor Nate Lewis and ultimately refined by his research group during a group retreat.[15] The concept was then adapted into a schematic by Elizabeth Santori, at the time a Lewis group graduate student. Her schematic is shown in Figure 1.6.[16] This solar fuels device architecture consists of a complimentary set of semiconductor light-absorbing materials with high-aspect ratio geometries, separated by an ion permeable membrane. The top layer would consist of a stable light absorbing material capable of absorbing high-energy photons and coupled with a robust catalyst capable of generating oxygen from water. The bottom layer would consist of an additional stable semiconductor which when coupled with suitable catalysts would be capable of generating hydrogen from protons in water. Several devices have been demonstrated with roughly similar design.

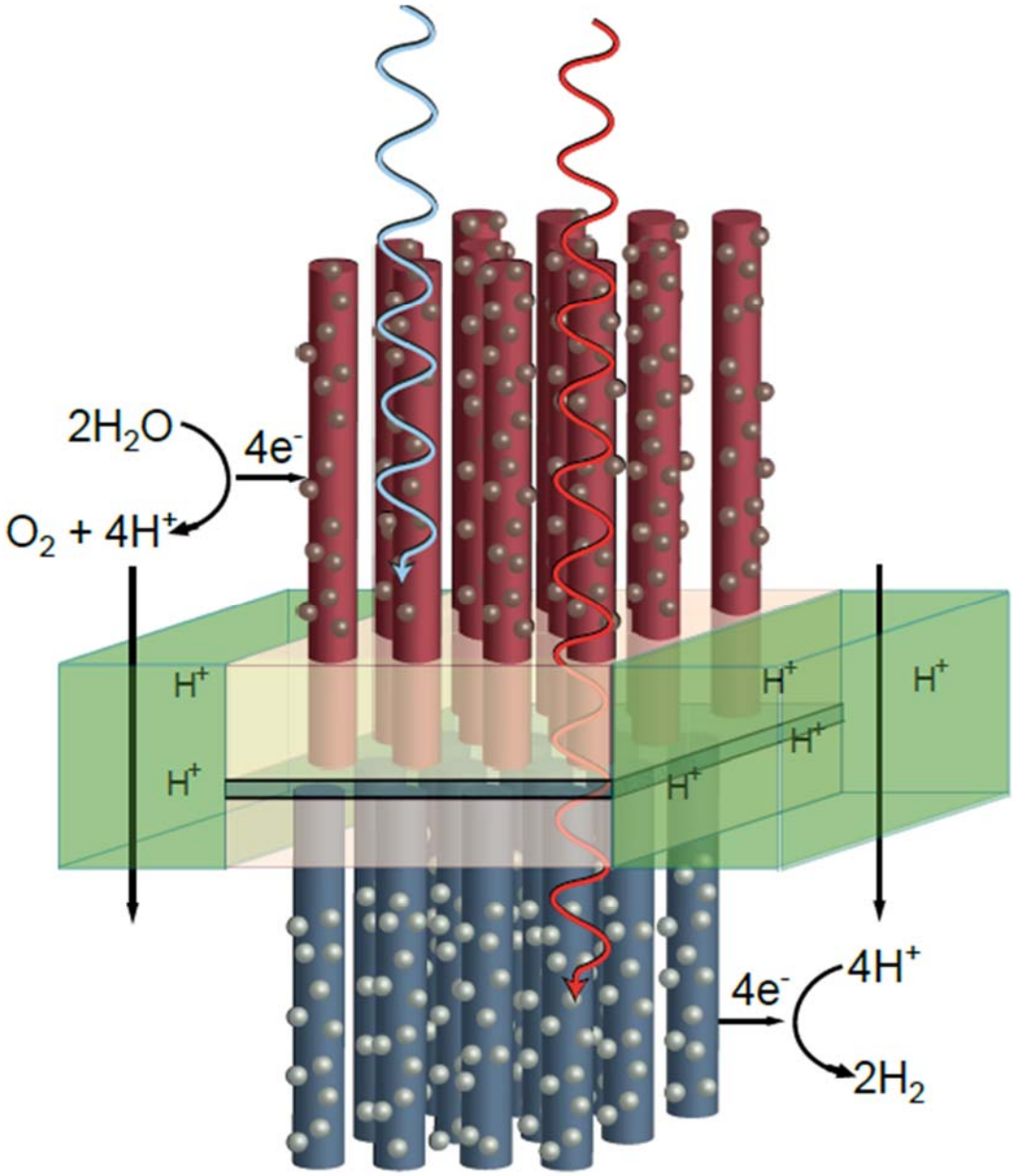


Figure 1.6 Schematic depiction of a solar water splitting device based on two parallel arrays of light absorbers with embedded catalysts, possessing an ion permeable membrane. Copyright 2013, Elizabeth A. Santori.[16]

The final component of the device, after light absorbers and catalysts, is the separating membrane layer. This layer serves several functions. First, it must be electrically conductive to connect the anode and cathode layers. It must also serve as a gas separator to prevent the formation of highly explosive mixtures of hydrogen and oxygen during device operation. Finally, the membrane must enable the transport of ions between the solutions surrounding both the anode and the cathode. Operation of the device generates a pH gradient between the anode and cathode as protons are consumed at the cathode, and generated at the anode. This pH gradient neutralization is necessary for continued operation of the device. The Lewis group has long had teams working on each of the necessary components of the solar fuels device. One subgroup focuses on catalysis, another on optimizing the efficiency and stability of light absorbing materials and yet a third subgroup has focused on total device integration with membranes and device design optimization. All of these teams together have made significant strides towards making a successful solar fuels generating device.

### 1.5.Chronological Research History

I joined Caltech in the fall of 2010 and spent the first 2 ½ years working with Theodore Agapie on developing bimetallic polymerization catalysts which would have the ability to copolymerize non-polar olefins such as hexane, ethylene, and propylene, with polar monomers. This work resulted in a patent, which was awarded in 2016 and is detailed in appendix A. I knew that my passions didn't lie with such work, and in the spring of 2013 made the transition into the Lewis group to work on renewable energy related projects.

At the time of my transition, recent work out of the Lewis group by James McKone and Adam Pieterick had highlighted some promising results from a class of semiconductors called the transition metal dichalcogenides (TMDCs). They had shown that the passivation of edge sites of single crystal samples of p-type $WSe_2$ was capable of sustained proton reduction, achieving solar to hydrogen efficiencies of greater than 7%.[17] After discussing possible research projects with Nate, we settled on me joining the transition metal dichalcogenide team (the chalcogenators) in exploring the differential reactivity of edge and terrace sites of TMDCs. A postdoc in the group, Jesus Velazquez, was exploring the edge-site differential reactivity for reduction of protons and fast redox couples by-way-of scanning probe electrochemical microscopy. I decided to study the nature of edge and terrace sites by exploring selective small molecule binding. We hypothesized that the improvement in charge carrier conversion efficiency when edge sites are blocked occurred as a result of preventing charge recombination at edge-sites. We also proposed that edge sites possessed open Mo or W coordination sites that serve as recombination centers. Thus I took on the task of synthesizing TMDC single crystals and performing experiments to probe small molecule binding to edge and terrace sites of synthetic single crystals. Although I was never able to show an improvement in photoelectrochemical properties because of covalent functionalization, I did find strong evidence for the localization of ortho-substituted aromatic dithiols to edge and defect sites of synthetic single crystals of $MoSe_2$ and $WSe_2$. This work is detailed in chapter 3 of this dissertation.

During the time I was exploring edge site reactivity, there was a huge uptick in research activity surrounding TMDCs. This was primarily a result of improved methods of

growth and techniques for the manipulation of layered materials coupled with the discovery of properties beneficial for their use as transistors, supercapacitors, and exciting properties relating to phase changes within the materials.[18-20] I embarked on a parallel path to explore the effects of terrace functionalization, which had been recently reported. An incoming graduate student, Ellen Yan, later picked up this project and she has already, at the time of writing this dissertation, made great progress towards understanding terrace functionalization as a method of tuning TMDC properties and expanding its breadth of uses. My discoveries of the reactivity surrounding terrace sites of synthetic single crystals of TMDCs are detailed in chapter four of this dissertation.

The final component of this dissertation is a short conclusion followed by appendices. Appendix A details the work completed while performing research as part of the Agapie group, before joining the Lewis group.

## 1.6.References

1. Conti, J.; Holtberg, P.; Diefenderfer, J.; LaRose, A.; Turnure, J. T.; Westfall, L. *International Energy Outlook 2016*; U.S. Energy Information Administration: May 2016, 2016.

2. BP *BP Statistical Review of World Energy 2016*; 2016.

3. Stocker, T. F., D. Qin, G.-K. Plattner, L.V. Alexander, S.K. Allen, N.L. Bindoff, F.-M. Bréon, J.A. Church, U. Cubasch,; S. Emori, P. F., P. Friedlingstein, N. Gillett, J.M. Gregory, D.L. Hartmann, E. Jansen, B. Kirtman, R. Knutti, K.; Krishna Kumar, P. L., J. Marotzke, V. Masson-Delmotte, G.A. Meehl, I.I. Mokhov, S. Piao, V. Ramaswamy, D.; Randall, M. R., M. Rojas, C. Sabine, D. Shindell, L.D. Talley, D.G. Vaughan and S.-P. Xie *Technical Summary. In: Climate Change 2013: The Physical Science Basis. Contribution of Working Group I to the Fifth Assessment Report of the Intergovernmental Panel on Climate Change*; Cambridge United Kingdom and New York, NY, USA, 2013.

4. Richter, B., *Beyond Smoke and MIrrors - Climate Change and Energy in the 21st Century*. Cambridge University Press: Cambridge, UK, 2014.

5. Blankenship, R. E.; Tiede, D. M.; Barber, J.; Brudvig, G. W.; Fleming, G.; Ghirardi, M.; Gunner, M. R.; Junge, W.; Kramer, D. M.; Melis, A.; Moore, T. A.; Moser, C. C.; Nocera, D. G.; Nozik, A. J.; Ort, D. R.; Parson, W. W.; Prince, R. C.; Sayre, R. T., Comparing Photosynthetic and Photovoltaic Efficiencies and Recognizing the Potential for Improvement. *Science* **2011,** *332* (6031), 805-809.

6. Smil, V., *Energy in Nature and Society : General Energetics of Complex Systems*. The MIT Press: Cambridge, Massachusetts, 2008; p 480.

7. SunPower Facts about Solar Technology from SunPower. https://us.sunpower.com/solar-panels-technology/facts/ (accessed December 12, 2016).

8. Laboratories, S. N. DOE Global Energy Storage Database. http://www.energystorageexchange.org/projects/data_visualization (accessed December 12, 2016).

9. Levine, J. G. Pumped Hydroelectric Energy Storage and Spatial Diversity of Wind Resources as Methods of Improving Utilization of Renewable Energy Sources. University of Colorado at Boulder, 2007.

10. Gyuk, I.; Johnson, M.; Vetrano, J.; Lynn, K.; Parks, W.; Handa, R.; Kannberg, L.; Waldrip, K.; Hearne, S.; Braccio, R. *Grid Energy Storage*; Department of Energy: December 2013, 2013.

11. Simbolotti, G.; Kempener, R. *Energy Storage - Technology Brief*; International Renewable Energy Agency: April 2012, 2012.

12. Dominion Bath County Pumped Storage Station. https://www.dom.com/corporate/what-we-do/electricity/generation/hydro-power-stations/bath-county-pumped-storage-station (accessed December 13, 2016).

13. Wadia, C.; Albertus, P.; Srinivasan, V., Resource constraints on the battery energy storage potential for grid and transportation applications. *Journal of Power Sources* **2011,** *196* (3), 1593-1598.

14. Tan, M. X.; Laibinis, P. E.; Nguyen, S. T.; Kesselman, J. M.; Stanton, C. E.; Lewis, N. S., Principles and Applications of Semiconductor Photoelectrochemistry. In *Progress in Inorganic Chemistry*, John Wiley & Sons, Inc.: 2007; pp 21-144.

15. McKone, J. R. Earth-Abundant Materials for Solar Hydrogen Generation. California Institute of Technology, Pasadena, CA, 2013.

16. Santori, E. Si Microwire Array Photoanodes for Artificial Photosynthetic Devices. California Institute of Technology, Pasadena, CA, 2013.

17. McKone, J. R.; Pieterick, A. P.; Gray, H. B.; Lewis, N. S., Hydrogen Evolution from Pt/Ru-Coated p-Type WSe2 Photocathodes. *Journal of the American Chemical Society* **2013,** *135* (1), 223-231.

18. Radisavljevic, B.; Radenovic, A.; Brivio, J.; Giacometti, V.; Kis, A., Single-layer MoS2 transistors. *Nature Nanotechnology* **2011,** *6* (3), 147-150.

19. Yin, Z. Y.; Li, H.; Li, H.; Jiang, L.; Shi, Y. M.; Sun, Y. H.; Lu, G.; Zhang, Q.; Chen, X. D.; Zhang, H., Single-Layer MoS2 Phototransistors. *Acs Nano* **2012,** *6* (1), 74-80.

20. Voiry, D.; Goswami, A.; Kappera, R.; SilvaCecilia de Carvalho Castro, e.; Kaplan, D.; Fujita, T.; Chen, M.; Asefa, T.; Chhowalla, M., Covalent functionalization of monolayered transition metal dichalcogenides by phase engineering. *Nat Chem* **2015,** *7* (1), 45-49.

**C h a p t e r 2**

# 2. Interplay of pH and Morphology in the HER Electrocatalysis on $MoSe_2$

## 2.1. Introduction

This chapter describes work on the synthesis and characterization of earth-abundant electrocatalysts for the HER. In these efforts, I collaborated with Jimmy John, a post-doctoral scholar in the Lewis group and Adam Pieterick, a graduate student in the Lewis group. We focused primarily on $MoS_2$ and $MoSe_2$ for our inquiries. Early on in our research, we observed an interplay between pH and morphology for $MoS_2$ and $MoSe_2$, which was largely unexpected. This interplay of pH and morphology is the focus of this chapter. Throughout this work, I focused on the optimization of the synthesis and study of large single crystal samples of $MoSe_2$. Jimmy and Adam together focused mostly on the synthesis and study of $MoS_2$.

## 2.2. Transition Metal Dichalcogenides for Hydrogen Evolution Reaction

$MoS_2$ and $MoSe_2$ are electrocatalysts for the hydrogen evolution reaction (HER).[1-2] Both compounds have been studied in detail for their electrocatalytic activities as part of an effort to identify a non-precious-metal alternative to Pt for use in water-splitting devices.[3-4] $MoSe_2$ and $MoS_2$ exist within a broader category of layered transition metal dichalcogenides. The transition metal dichalcogenides (TMDCs), or $MX_2$s (M = Mo, W; X = S, Se), are earth abundant semiconducting layered materials which possess suitable band gap energies (1.2-

2.0 eV) for solar energy applications.[5] TMDCs have a layered crystal structure, and the catalytically active sites for the HER in acidic solution are exposed step edges.[6] Since this finding, improvement of $MoS_2$ and $MoSe_2$ electrocatalysts has focused on increasing the electrochemically accessible step edges. This approach has resulted in synthetic attempts toward generating TMDC samples with decreasing crystallinity.[4] In the system where $MoS_2$ nanoparticles are optimally loaded onto a conductive electrode, an active electrode in contact with 0.5 M $H_2SO_4$ (aq) requires the application of an overpotential of ~ -150 mV in order to drive the HER to a current density of -10 $mA \cdot cm^{-2}$.[7] Similarly, $MoSe_2$ is a low overpotential hydrogen evolution electrocatalyst. In one study with an in situ generated $MoSe_2$ macroporous film, a steady state overpotential of ~250 mV was required to pass -10 $mA/cm^2$ of hydrogen evolution current.[1]

In the application space of electrolyzers and solar water-splitting cells, devices, which operate under alkaline conditions, are active areas of research and development.[8-9] In trying to develop a solar water-splitting device, it has been challenging to find semiconductors which are stable under oxygen-evolution conditions in acidic aqueous solution. This has presented a significant impediment to the development of a fully integrated solar water-splitting device.[10] However, there has been a recent development in protective coatings, which can incorporate a non-noble metal catalyst of the oxygen-evolution reaction while simultaneously stabilizing important semiconductors such as Si, GaAs, and CdTe while in contact with strongly alkaline electrolytes.[11-13] These discoveries help to further drive efforts to develop non-noble catalysts for the HER that are active and stable under alkaline conditions.

$MoS_2$ surfaces in contact with acidic solutions are well established as electrocatalysts for the HER. However, electrocatalysis of the HER by $MoS_2$ and $MoSe_2$ in contact with alkaline electrolytes remains mostly unexplored. Stable electrocatalysis of the HER has been demonstrated recently for amorphous molybdenum sulfides and $MoS_2$ nanoparticles in contact with 1M KOH which proceeded also with high catalytic activity.[14] While edge-sites have been established as the active electrocatalytic site for $MoS_2$ and $MoSe_2$ in contact with acidic aqueous solutions, the catalytic mechanism for the HER at $MoSe_2$ and $MoS_2$ surfaces in contact with aqueous alkaline solutions has not yet been established.

### 2.3. HER Catalysis on $MoS_2$ and $MoSe_2$ Single Crystals

Bulk single crystals of $MoSe_2$ and $MoS_2$ possess a high overpotential for the HER when in contact with acidic or neutral aqueous solutions and are thus poor catalysts for catalyzing the transformation of protons to hydrogen. $MoSe_2$ single crystals typically require the application of an overpotential in excess of -700 mV to drive the HER at a current density of -10 $mA/cm^2$. $MoS_2$ single crystals in contact with 1 M $H_2SO_4$ can often require the application of an overpotential in excess of -1.0 V to drive the HER at a current density of --10 $mA/cm^2$. Figure 2.1 shows a linear sweep voltammogram of a synthetic single crystal of $MoSe_2$ compared to a platinum mesh. This data was collected in a 1 M solution of aqueous $H_2SO_4$. One can observe the high overpotential of the single crystal $MoSe_2$ sample compared to platinum. Even though this particular $MoSe_2$ sample was one of the most effective single-crystal $MoSe_2$ samples from which data was collected for the HER, it still possesses an overpotential 500 mV greater than that of platinum. However, well-defined surfaces of single crystals provide unique opportunities for the rigorous study of electron-solution interfaces

and mechanisms of electrocatalysis. In this section, I will compare the electrocatalytic activity of single crystals of primarily $MoSe_2$ for the HER in aqueous and alkaline solutions, considering also $MoSe_2$ of differing morphologies and sources.

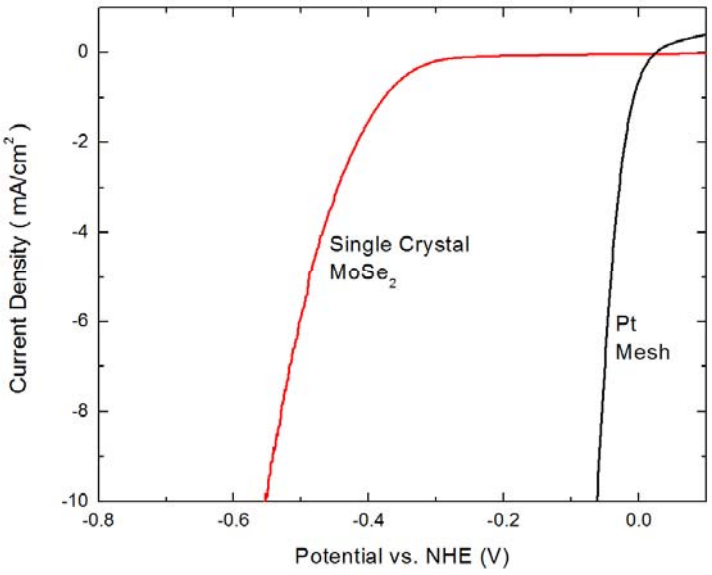


Figure 2.1. A linear sweep voltammogram of a synthetic single crystal of $MoSe_2$ compared to a platinum mesh in 1.0 M $H_2SO_4$.

## 2.4. Comparative Study of the HER in Acidic and Alkaline Solutions for differing Morphologies of $MoSe_2$

Respectively, the efficiency for catalyzing the hydrogen evolution reaction in acidic media with $MoSe_2$ increases as the crystallinity of the species decreases such that:

$$\sigma_{SC} > \sigma_{PC} > \sigma_{AM}$$

Where $\sigma_{SC}$ = the overpotential for the HER on a single crystal sample, $\sigma_{PC}$ is the overpotential for the HER on a polycrystalline sample, and $\sigma_{AM}$ is the overpotential for the HER on an amorphous sample. Generally, amorphous transition metal dichalcogenides materials are the most efficient for catalyzing the hydrogen evolution reaction. Figure 2.2 shows the current-voltage traces for typical amorphous, polycrystalline, and single-crystal samples of $MoSe_2$ in 1.0 M $H_2SO_4$. In these samples the potential required to drive 10 mA/cm$^2$ of reductive current is; $\sigma_{SC10}$ = -0.748 V versus RHE, $\sigma_{PC10}$ = -0.515 V versus RHE, and $\sigma_{AM10}$ = -0.227 V versus RHE for each sample respectively.

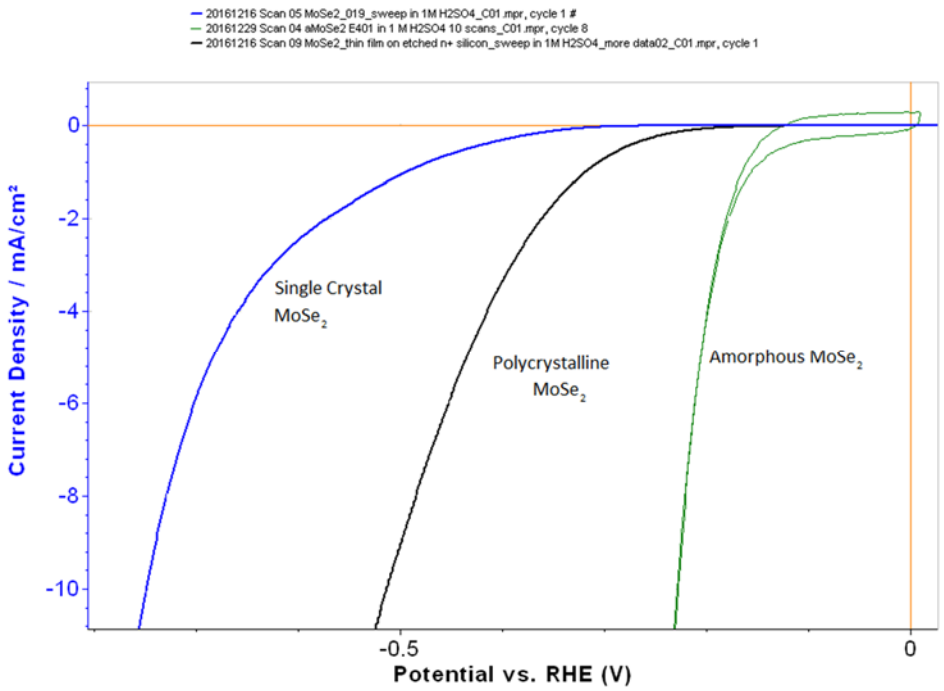


Figure 2.2. Cyclic Voltammetry traces of Amorphous $MoSe_2$ (green), polycrystalline $MoSe_2$ (black), and single crystal $MoSe_2$ (blue) in 1 M $H_2SO_4$. The potential is referenced to a reversible hydrogen electrode (RHE).

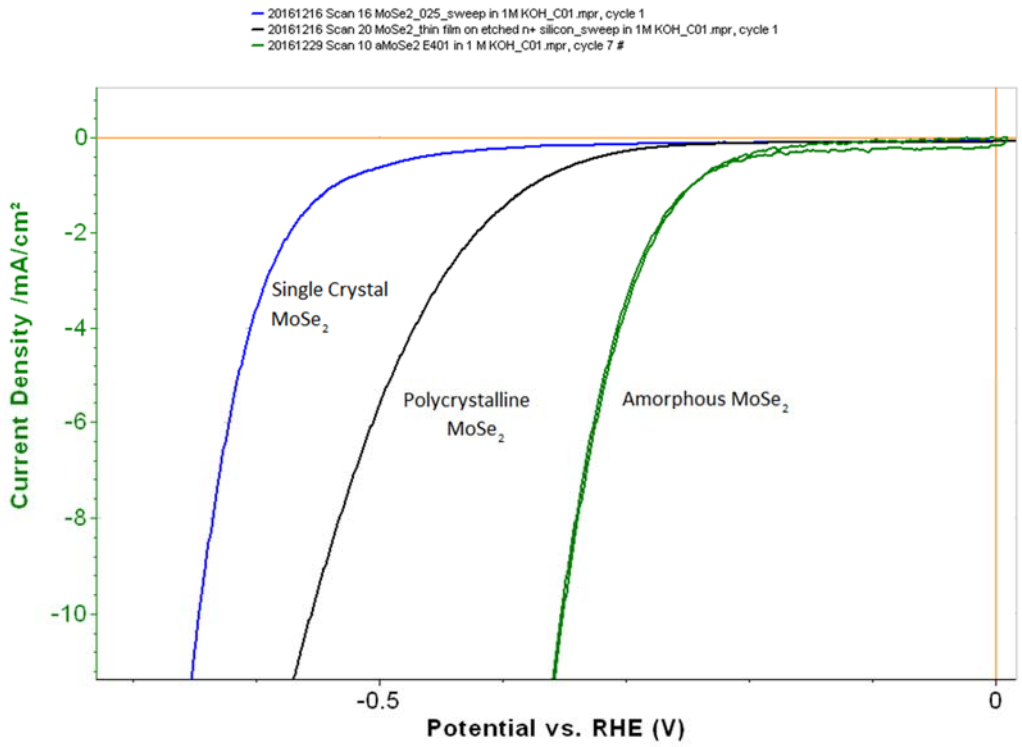


Figure 2.3 Cyclic Voltammetry traces of Amorphous $MoSe_2$ (green), polycrystalline $MoSe_2$ (black), and single crystal $MoSe_2$ (blue) in 1 M KOH. The potential is referenced to a reversible hydrogen electrode (RHE).

The trend of HER overpotential to crystallinity continues in alkaline solutions. Amorphous transition metal dichalcogenides materials are the most efficient for catalyzing the hydrogen evolution reaction. Figure 2.3 shows the current-voltage traces for typical amorphous, polycrystalline, and single-crystal samples of $MoSe_2$ in 1 M KOH. In these samples the potential required to drive 10 mA/cm$^2$ of reductive current is , $\sigma_{SC10}$ = -0.645 V versus RHE, $\sigma_{PC10}$ = -0.556 V versus RHE, and $\sigma_{AM10}$ = -0.351 V versus RHE for each sample respectively.

This would be rather an unremarkable finding, especially considering the result by Jaramillo in 2007 which presented a strong case for the edge sites of transition metal

dichalcogenides being the active sites for the HER. However, when one looks more closely at the relationship between pH, morphology, and activity for the HER, a more interesting picture emerges.

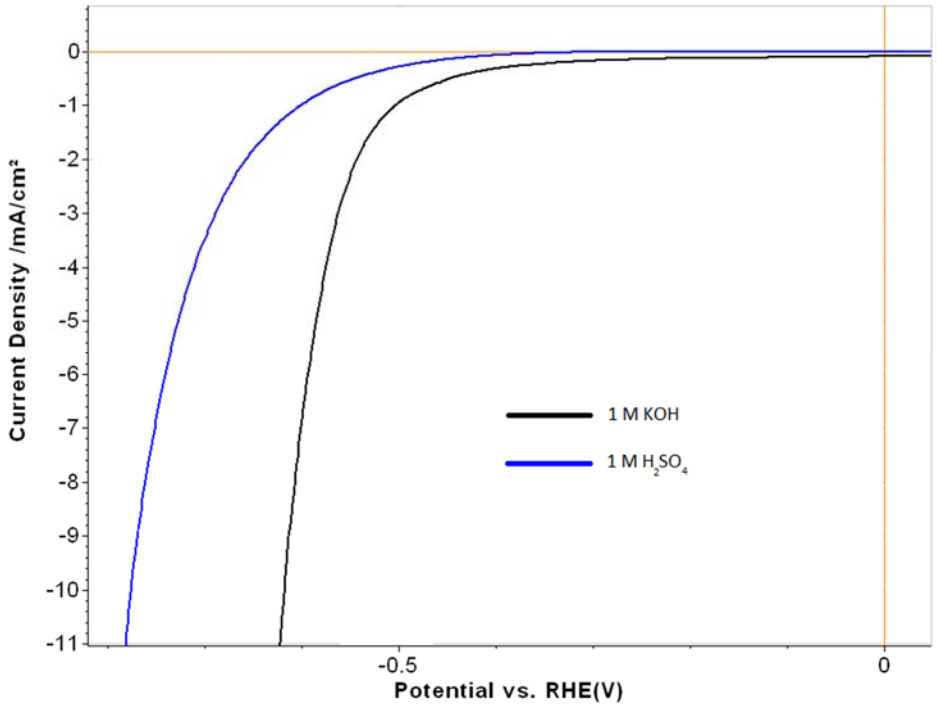


Figure 2.4. Linear sweep voltammogram of the same single crystal $MoSe_2$ sample first in 1 M $H_2SO_4$, (blue trace) and then in 1 M KOH (black trace). The potential required to drive -10 mA/cm$^2$ of current requires an overpotential ~150 mV higher for the same $MoSe_2$ crystal in acid than is required in base.

For single crystal samples of $MoSe_2$, the overpotential required to drive a current density of -10 mA/cm$^2$ is higher for 1 M $H_2SO_4$ than for 1 M KOH. Figure 2.4 shows a rather extreme example of the phenomenon with the $MoSe_2$ crystal in acid requiring nearly 150 mV additional overpotential to drive the same current density. This situation reverses with samples of

polycrystalline $MoSe_2$. The overpotential to drive -10 mA/cm$^2$ of current on a polycrystalline sample of $MoSe_2$ is lower in 1 M acid than in 1 M base.

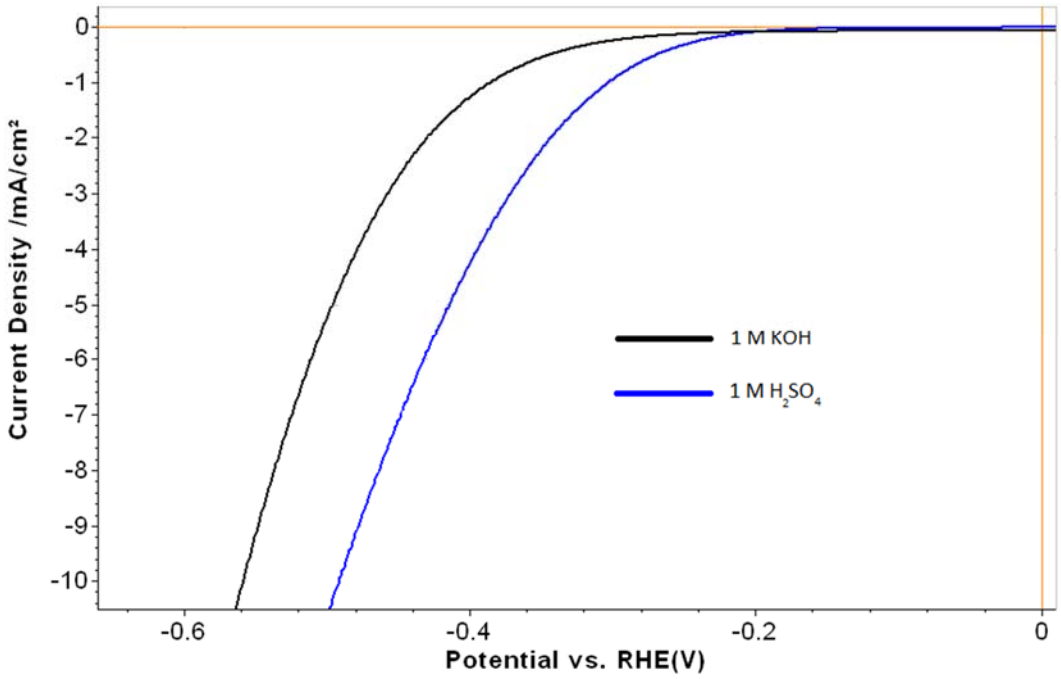


Figure 2.5 Linear sweep voltammogram of the same polycrystalline $MoSe_2$ on $n^+$ silicon sample first in 1 M $H_2SO_4$, (blue trace) and then in 1 M KOH (black trace). The potential required to drive -10 mA/cm$^2$ of current requires an overpotential ~70 mV higher for the same $MoSe_2$ sample in base than is required in acid.

In amorphous samples of $MoSe_2$ on highly oriented pyrolytic graphite, the behavior towards HER is most similar to that of polycrystalline $MoSe_2$. Overall, the working electrode potential required to drive -10 mA/cm$^2$ of current is less than for the polycrystalline sample. Also, the overpotential for the amorphous sample in acid is lower than the overpotential observed in basic solution. Figure 2.6 shows cyclic voltammetry of a sample of amorphous $MoSe_2$ in 1 M $H_2SO_4$ and also in 1 M KOH. The potential required to drive -10 mA/cm$^2$ in 1

M $H_2SO_4$ was -0.247 V versus RHE. The potential required to drive -10 mA/cm$^2$ in 1 M KOH was -0.403 V versus RHE, a difference of greater than 150 mV in overpotential when switching from acidic to basic solution.

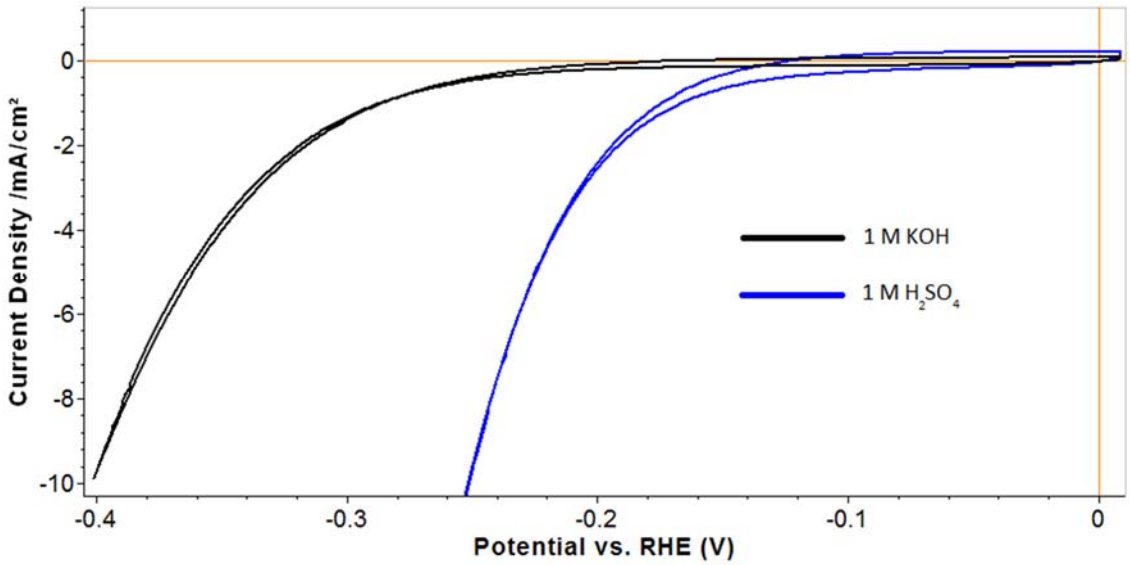


Figure 2.6. Cyclic voltammetry sweep of a sample of amorphous $MoSe_2$ on HOPG. Scans were first run in 1 M $H_2SO_4$, (blue trace) and then in 1 M KOH (black trace). The potential required to drive -10 mA/cm$^2$ of current requires an overpotential ~150 mV higher for the same $MoSe_2$ sample in base than is required in acid.

Figure 2.7 shows the summary of data collected on single crystal, polycrystalline thin film, and amorphous $MoSe_2$ materials. Data was collected from seven separate single crystal samples of $MoSe_2$, three polycrystalline thin film samples, and two amorphous $MoSe_2$ samples. There was a high degree of variation in overpotential for single crystal samples (standard deviation, SD = 50-73 mv) when compared to polycrystalline thin film samples (SD = 7 – 29 mV) and amorphous samples (SD = 11-21 mV). This is likely a result of slightly different growth

conditions during crystal synthesis, resulting in synthetic crystals with varying crystallinity, doping, and defect density.

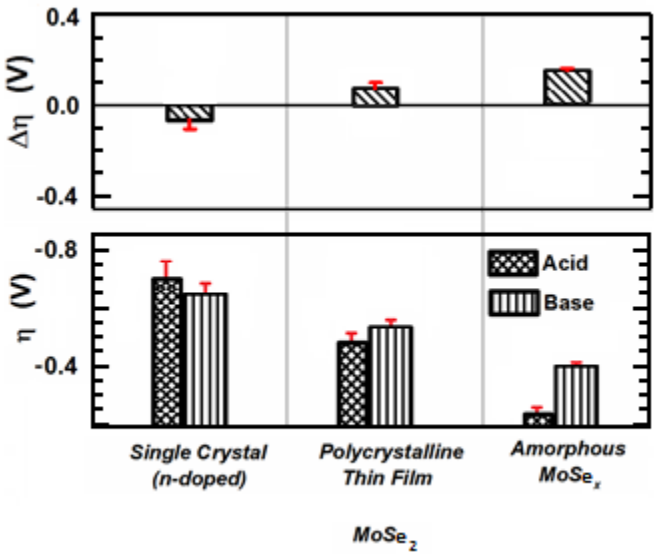


Figure 2.7. Effect of morphology on the kinetics for the hydrogen evolution reaction on $MoSe_2$-based materials in acid (1 M $H_2SO_4$) or base (1 M KOH). The Y-axis shows the overpotential relative to RHE needed to achieve -10 mA/cm$^2$. Error bars are shown at ± 1 standard deviation.

## 2.5. Conclusions

In summary, single crystals of $MoSe_2$ exhibited enhanced kinetics for the hydrogen-evolution reaction when in contact with alkaline solutions relative to the electrocatalytic activity observed in contact with acidic solutions. The hydrogen-evolution activity was highly sensitive to the crystallinity of $MoSe_2$ materials when in contact with acidic solutions. However, the electrocatalytic activity of $MoSe_2$ materials in contact with alkaline solutions was much less sensitive to the crystallinity of the materials. These results suggest that the active sites for HER on $MoSe_2$ in contact with strongly alkaline solutions may not be the step edges, as is has been

shown for acidic solutions. Therefore, the hydrogen-evolution reaction may proceed through a different mechanism than that which has been described for $MoS_2$ in contact with acidic solutions.

## 2.6. Experimental Synthetic Methods

Single crystal, polycrystalline, and amorphous $MoSe_2$ were used for this comparative study on the electrocatalysis for the HER. In the following sections the synthetic methods used to prepare each type of $MoSe_2$ sample are described.

### 2.6.1. Synthesis of Single Crystal $MoSe_2$

Single crystal samples of n-type $MoSe_2$ were grown using a chemical-vapor transport (CVT method). In detail, quartz ampoules prepared from various diameter quartz tubing, purchased from GM associates. Tubes were sealed at one end with a hydrogen/oxygen torch and then were soaked in a standard base bath (300g potassium hydroxide, 4 L isopropyl alcohol, 1 L water) for 12 hours to lightly etch the surface of the quartz to clean the ampoules. The ampoules were then washed with ultrapure water and acetone 5 times each.

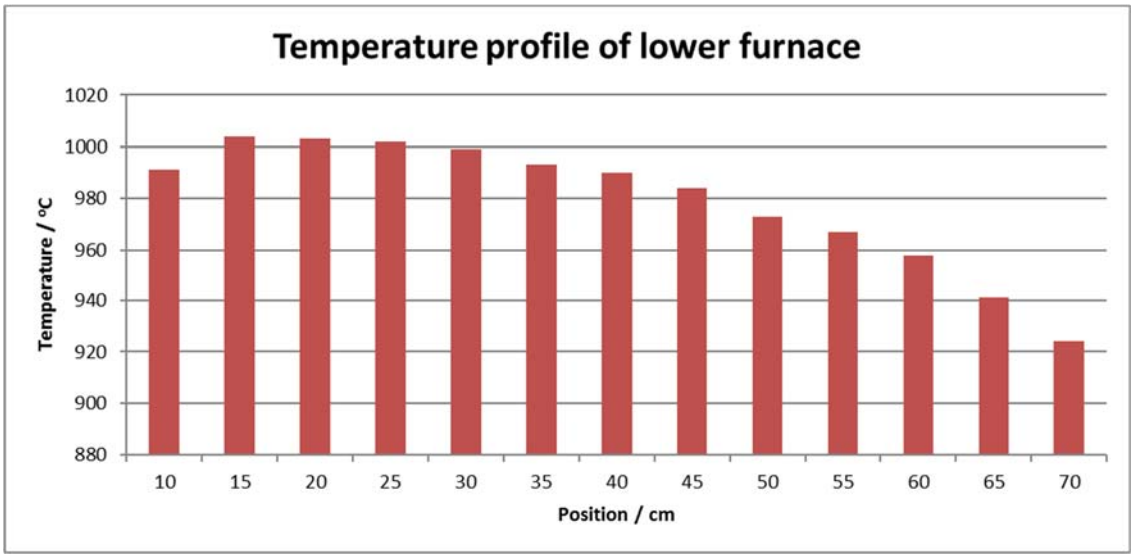


Figure 2.8. Typical temperature profile of the Carbolite tube furnace used for $MoSe_2$ crystal growth. Although the 2-zone furnace had nominal temperature settings of 1025°C and 975°C for each zone respectively, a probe of the two zones showed a charge zone of ~1005°C and a growth zone of ~960°C, approximately 20 degrees lower than the programmed temperature.

Polycrystalline $MoSe_2$ bulk powder was prepared by first loading a 25 mm inner diameter quartz ampule with a stoichiometric mixture of Mo and Se using 2.000 grams of molybdenum powder and 3.291 grams of selenium pellets. The ampoule was evacuated to less than $1.0 \times 10^{-3}$ torr and sealed with a natural gas/oxygen flame. The sealed ampule was then heated to 900°C for 24 hours in a single-zone Lindberg heavy-duty tube furnace.

Next, 1.000 grams of polycrystalline bulk $MoSe_2$ powder was placed in a quartz ampoule along with $SeCl_4$ and evacuated to less than $1.0 \times 10^{-5}$ torr. An effort was made to restrict the reagents to one end of the ampoule. The sealed ampoule was placed in a two-zone carbolite tube furnace and heated for 24 hours at 1025°C in the growth zone and 975°C in the charge zone to clean the growth zone to remove unwanted nucleation sites. Figure 2.8

shows a typical temperature profile inside of the tube furnace used for growth with each zone 15-20 °C below the desired temperatures. The temperature gradient was then reversed, producing a nominal temperature of 975°C in the growth zone and 1025°C in the charge zone with a gradient of ~2 °C $cm^{-1}$. Figure 2.9 shows a schematic of the ampoule used during the chemical vapor transport method. During crystal growth, the charge zone contains polycrystalline powder of the desired semiconductor crystal. In the lower temperature growth zone, single crystals nucleate and grow on the walls of the ampoule. After seven days, several smooth, hexagonal shaped platelets of crystalline $MoSe_2$ as large as 10mm on a side were obtained. Several growths of crystalline $MoSe_2$ were attempted using similar procedure but with variations in growth time, and transport agent concentration. Each growth yielded crystalline material, but only a few growths produced a large quantity of crystals that were of the appropriate size for study. Crystals, which were not fabricated into electrodes, were stored in an inert atmosphere glove box.

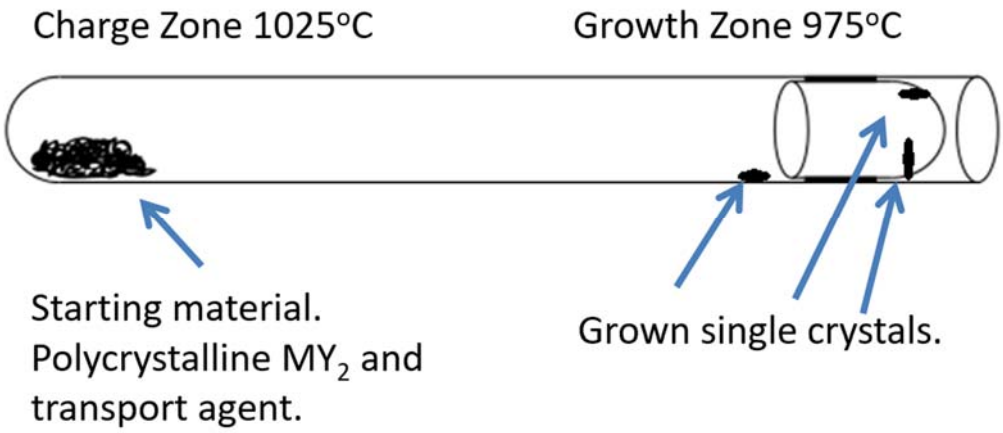


Figure 2.9 Schematic of chemical vapor transport method. During crystal growth, the charge zone contains polycrystalline powder of the desired semiconductor

crystal. In the lower temperature growth zone, single crystals nucleate and grow on the walls of the ampoule.

Crystals grown by this method without an additional dopant added to the ampoule during growth are consistently n-type. In order to achieve p-type crystals, additional dopants such as niobium are required. The n-type crystals are desirable for the study of the hydrogen evolution electrocatalysis because of the mobile majority carriers available for proton reduction. Crystals synthesized by the CVT method came in a variety of different morphologies. The most common type grown were what are best described as flowers. Layered crystals were like the petals of a rose, each arranged around a central point and sharing contact on at least one edge with other crystal flakes. These samples generated high quality sheets but were difficult to separate the individual crystal sheets. The next common morphology were individual crystals. These were the highest quality and easiest to work with. They consisted of a single crystal with clean edges. They were sometimes hexagonal in shape, and in other instances elongated and lacking a hexagonal shape. The crystal on the far-right in Figure 2.10 is a good example of the latter type. These crystals could be readily cut into the sizes desired for the fabrication of electrodes and could be easily exfoliated with adhesive tape to reveal pristine, $MoSe_2$ surfaces by removing damaged or oxide-rich surface layers.


Figure 2.10. Camera image of synthetic single crystal $MoSe_2$ grown by chemical vapor transport method.

Figure 2.11 shows a light microscope image of a synthetic single crystal of $MoSe_2$ after cleavage with adhesive tape. This region of the crystal highlights the layered structure of a transition metal dichalcogenides single crystal. This crystal was chosen because of its high number of optically visible step edges and was not used for electrochemical experiments. Figure 2.12 shows a different region on the same $MoSe_2$ crystal. This image focuses on a terrace domain, where few microscopic edge sites are visible. Some hairline step-edges are visible as well as a region which was partially exfoliated with adhesive tape during the exfoliation process. This region is visible in the left side of the image in Figure 2.12. In samples chosen for use in electrochemical experiments for the HER, the number of microscopically visible edge sites were minimized and the terrace sites were selected for.

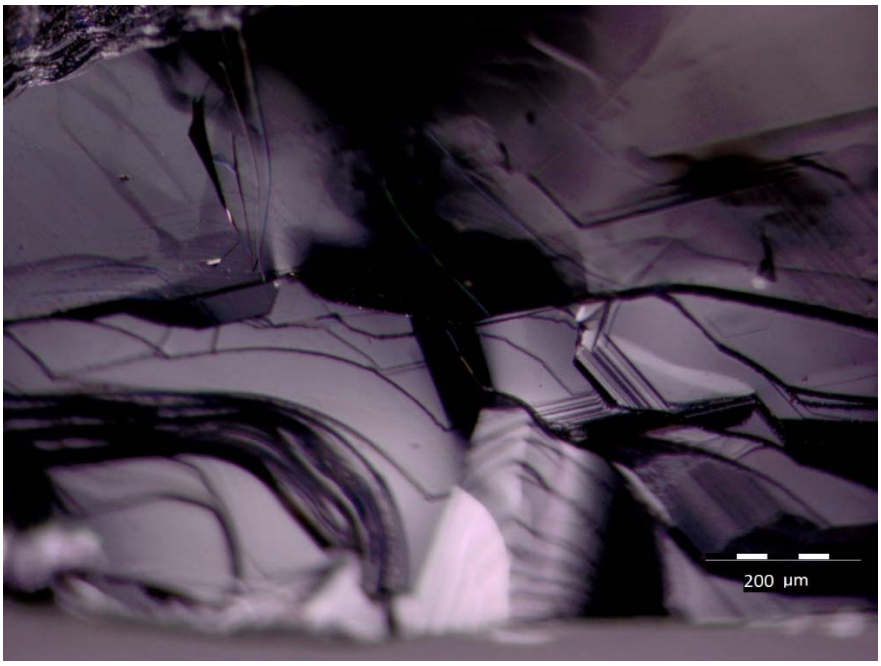


Figure 2.11. Light microscope image of the layered structure in a synthetic $MoSe_2$ crystal.

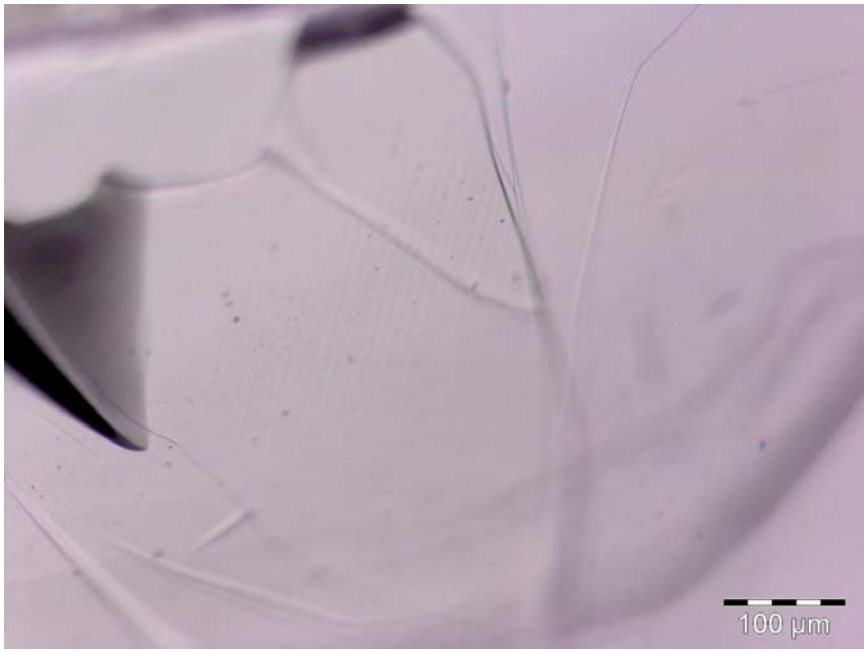


Figure 2.12. Light microscope image of a smooth terrace region of a synthetic $MoSe_2$ crystal. Several macroscopic edges remain visible.

### 2.6.2. Synthesis of Polycrystalline Thin Films of $MoSe_2$

Polycrystalline thin films were prepared on a number of substrates, including n+ silicon, p-type silicon, and highly oriented pyrolytic graphite. For the purposes of studying the electrocatalysis of $MoSe_2$ polycrystalline thin films, samples prepared on n+ silicon were used. First, n+ silicon, doped with phosphorus with a resistivity of < 0.002 Ω·cm first had its oxide etched away using a buffered HF solution (nominally 7% HF content and 35% $NH_4F$ content) for 5 minutes. During this process, the n+ silicon wafer became highly hydrophobic. The wafer was then washed three times with ultrapure water (18.3 MΩ resistivity). Next, the wafer is dried under a stream of nitrogen and transferred to an electron beam metal evaporator. Using standard procedures, Mo is evaporated onto the silicon surface to a thickness of 20 nm at a deposition rate of ~0.7 Å/s. The thickness of the deposition is monitored by-way-of a quartz crystal monitor positioned at the same distance from the source as the target substrate. Following deposition of molybdenum, the surface was characterized before converting the film to the metal selenide.

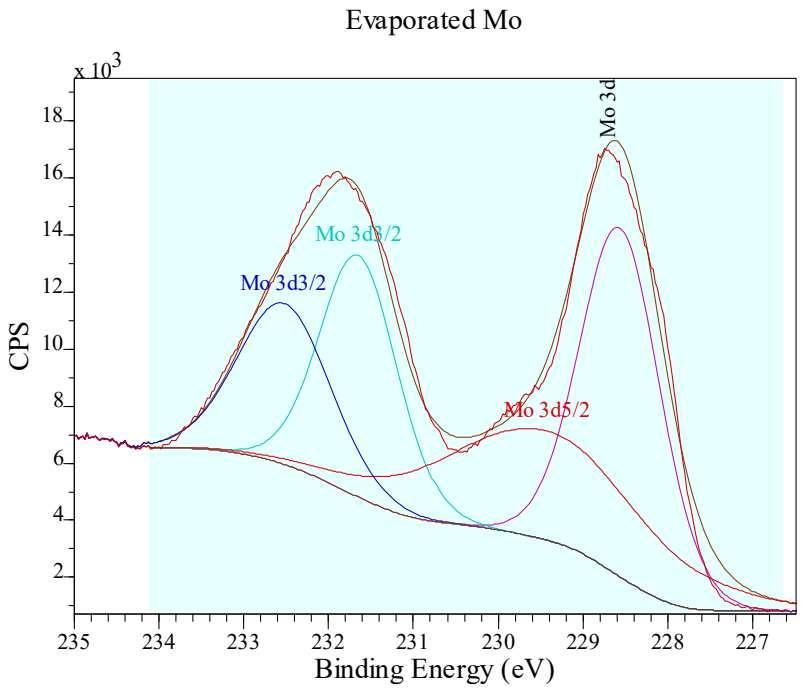


Figure 2.13 XPS spectrum of the Mo 3d region for evaporated molybdenum prior to selenization to $MoSe_2$.

The x-ray photoelectron spectroscopy (XPS) high-resolution spectrum of evaporated molybdenum possessed two strong peaks which were attributable to $MoO_x$, where x = 0-3, after exposure to atmosphere. One Mo $3d^{5/2}$ peak was located at a binding energy of 228.6 eV, corresponding to molybdenum (delta) oxides, $Mo^{\delta+}$, where $0 < \delta < 4$ in oxidation state.[15] The broader Mo $3d^{5/2}$, centered at 229.4 is most likely $MoO_2$ with $Mo^{4+}$ as the oxidation state. No meaningful signature for $MoO_3$ was detectable in the high-resolution XPS spectrum. The Mo $3d^{5/3}$ signal for $Mo^{6+}$ in $MoO_3$ has been reported as being located at a binding energy of 232.5eV. None of the XPS signal from the silicon substrate was observed in the survey spectrum of evaporated Mo with 20 nanometers of thickness, indicating a low number of pinholes in the film

over the area of the X-ray beam. It also indicates that the 20 nm thickness of Mo is higher than the escape depth for photoelectrons from $MoO_x$.

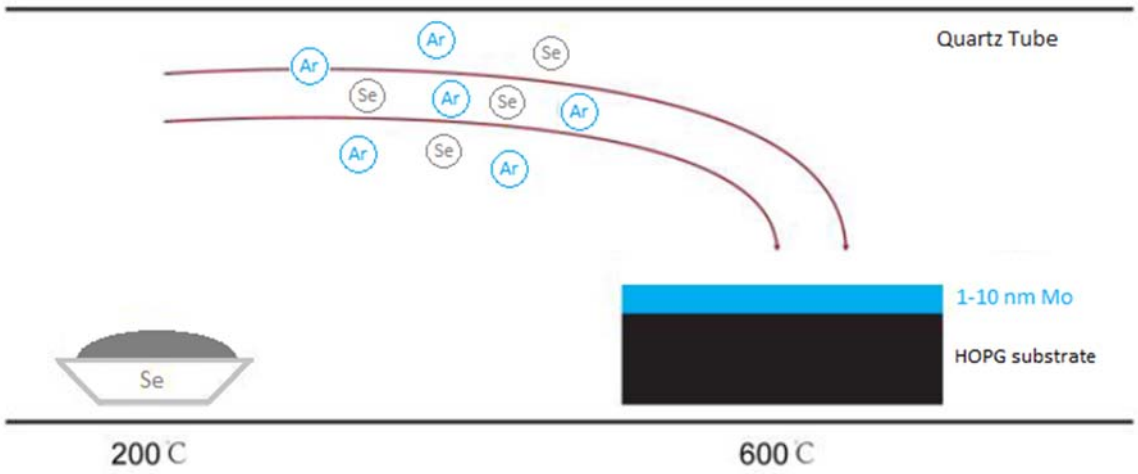


Figure 2.14. The synthesis of polycrystalline thin films of $MoS_2$ and $MoSe_2$.

Next, the silicon sample with 20 nm of evaporated Mo was transferred to a quartz boat in a 25mm diameter quartz tube connected as part of a custom chemical vapor deposition system. This system is connected to a turbo pump as well as a scroll pump. It has mass flow controllers connected to the system enabling the passage of up to 100 sccm each of four different gases: argon, nitrogen, hydrogen, and chlorine.

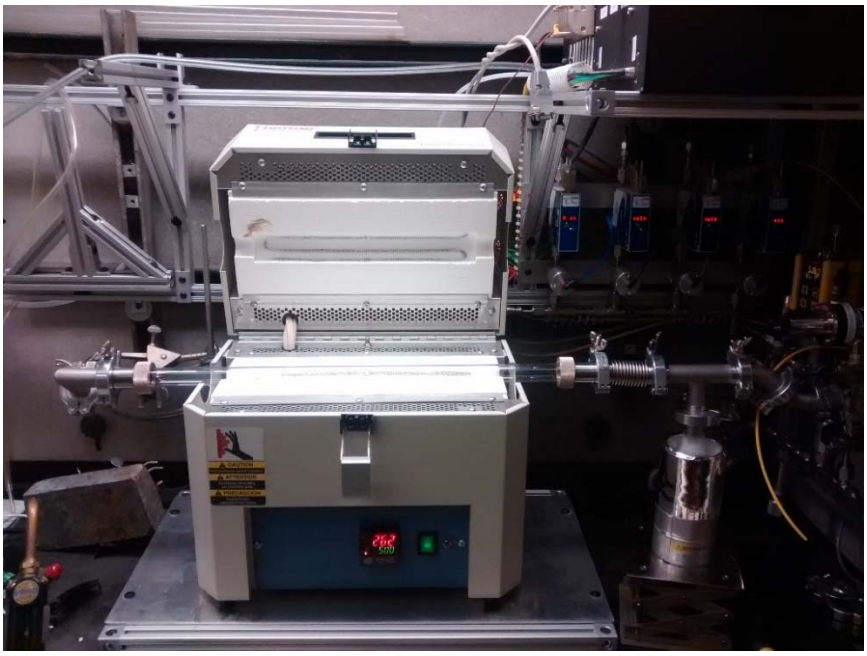

Figure 2.15. Custom chemical vapor deposition (CVD) system for the growth of $MX_2$ polycrystalline thin films.

Figure 2.16. Experimental setup for the synthesis of polycrystalline thin films of $MoS_2$ and $MoSe_2$.

A small furnace (in Figure 2.15) was situated to surround the quartz tube and possessed a single zone for temperature control. The quartz boat containing the Mo coated silicon sample was centered in the furnace. At the edge of the tube furnace, straddling the interface, was a small 3" quartz boat containing 400 mg of selenium beads. To perform the synthesis, the tube was evacuated to < 1 x 10-2 torr. Then, 100 sccm of Argon was flowed through the tube for 10 minutes at which point the temperature of the furnace was set to 550°C and without controlling the temperature ramp rate the desired temperature was reached in 20 minutes. The selenium pellets at the edge of the furnace melted and some became gaseous as evidenced by the deposition of selenium on the walls of the tube downstream on the other end of the heated zone. The furnace was held at reaction temperature of 550°C for 10 minutes, followed by natural cool down, during which Ar gas was kept flowing at a rate of 100 sccm to transport selenium to the substrate.

The polycrystalline thin film was characterized by XPS. Figure 2.17 shows the survey spectrum of as-grown MoSe2 polycrystalline thin film. The survey spectrum is consistent with $MoSe_2$ in general. High-resolution scans give a better idea of the oxidation states of Mo and Se within the film. Figure 2.18 shows the Mo 3d region of the XPS spectrum of polycrystalline $MoSe_2$. The Mo $3d^{5/2}$ peak is centered at a binding energy of 228.9 eV, consistent with a Mo4+ oxidation state for MoSe2. More evidence for the formation of $MoSe_2$ is seen in the high-resolution spectrum corresponding to the Se 3d region. A single oxidation state of selenium is present in the spectrum, with the Se 3d5/2 peak centered at 55.19 eV. The ratio of Se 3d to Mo 3d in the survey spectrum is ~1.70. This is consistent for edge rich $MX_2$ compounds because of the appearance of chalcogenide deficiencies in the material.

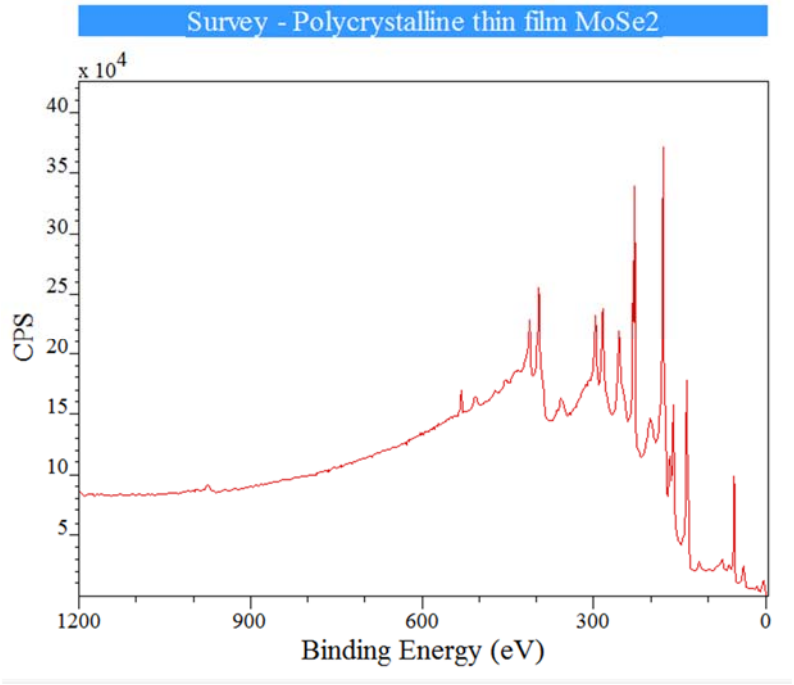


Figure 2.17. XPS survey spectrum of 20 nm polycrystalline thin film of $MoSe_2$.

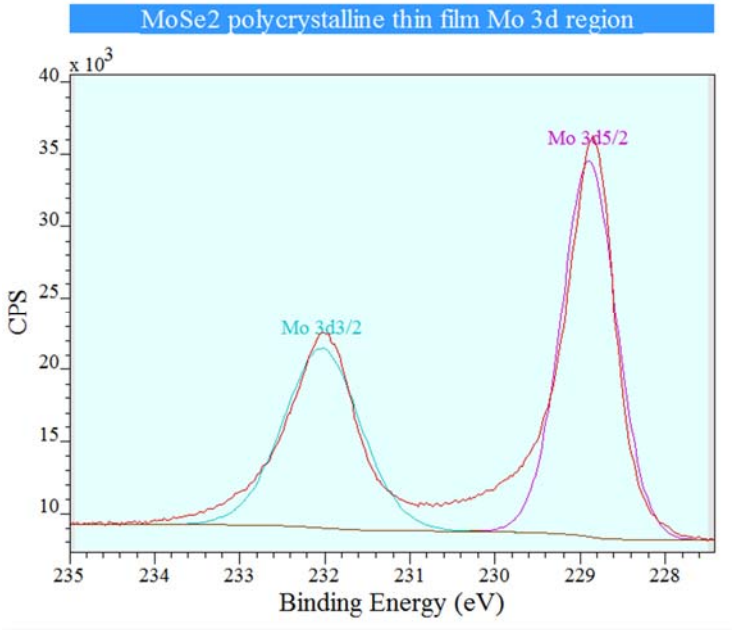


Figure 2.18. XPS high-resolution spectrum of the Mo 3d region of a polycrystalline thin film of $MoSe_2$.

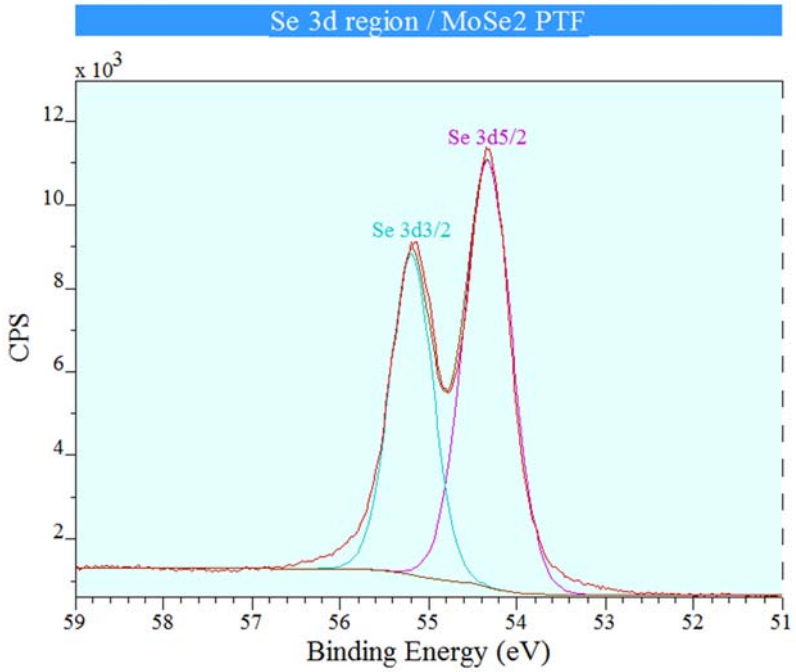


Figure 2.19. XPS high resolution spectrum of $MoSe_2$ polycrystalline thin films. Spectrum is centered in the Se 3d region.

To show this material is polycrystalline in nature with the majority orientation of the layers vertical, we utilized a characterization technique described by Cui et al in their characterization of PTF's of $MoS_2$ and $MoSe_2$. The Raman peak corresponding to the out-of-plane Mo-S phonon mode (A1g) is preferentially excited for edge-terminated film due to the polarization dependence, whereas the in-plane Mo-Se phonon mode (E12g) is preferentially excited for terrace-terminated films. Figure 2.20 shows the A1g and E12g phonon modes for a polycrystalline sample of $MoSe_2$. Because the A1g intensity is greater than that of the E12g intensity, we can conclude that this film is primarily composed of vertically oriented grains of $MoSe_2$. This results in a high number of exposed edge sites on the sample, much higher than

would be found in a single crystal sample of $MoSe_2$. This result is important in understanding the electrochemical measurements regarding the hydrogen evolution reaction catalysis.

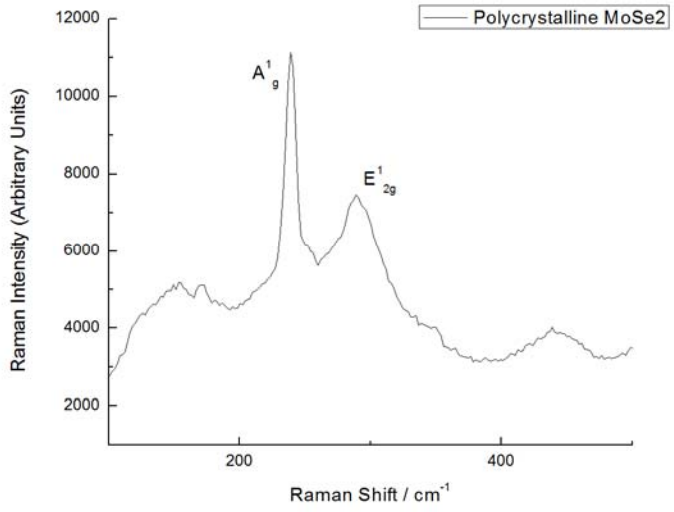


Figure 2.20. Raman spectrum of polycrystalline $MoSe_2$. The vertical alignment of the $MoSe_2$ layers in the film can be seen in the ratio of $A^1_g$ to $E^1_{2g}$ phonon modes. If the ratio of $A^1_g$ to $E^1_{2g}$ is high, the $MoSe_2$ layers in the film are primarily oriented vertically.

### 2.6.3. Synthesis of Amorphous $MoSe_2$

An operando synthesis method was utilized to create amorphous films of $MoSe_2$.1 Thin films of molybdenum diselenide were synthesized using a two-step wet chemical method. In this method, excess sodium selenide was first added to a solution of ammonium heptamolybdate in aqueous sulfuric acid, resulting in the spontaneous formation of a black precipitate containing a mixture of species. After purification and drop-casting onto a glassy carbon electrode, the species active for the HER was formed after application of a reductive potential to the coated electrode. The synthesis is detailed below.

Ammonium heptamolybdate, $(NH_4)_6Mo_7O_{24}\cdot 4H_2O$ [0.40 g, 3.47 x $10^{-4}$ mol, 99.98% (Sigma-Aldrich, St. Louise, MO)], was dissolved in 8 mL of a 0.20 M $H_2SO_4$ solution prepared by diluting 18 M $H_2SO_4$ with $H_2O$. A separate solution was prepared by dissolving 0.10 g (8 x $10^{-4}$ mol) of sodium selenide, $Na_2Se$ [99.8% (Alfa Aesar, Ward Hill, MA)], in 8 mL of $H_2O$. The first solution of Mo was quickly poured into the second solution and a black precipitate was formed upon mixing. This mixture was agitated with a sonicator for 10 minutes. Next, the suspension was transferred to a centrifuge tube and centrifuged for 30 minutes at ~ 4000 rpm. A black precipitate collected at the bottom of the centrifuge tube. The supernatant liquid, which still contained some black color, was discarded. The precipitate was rinsed with 2 10 mL aliquots of 2-propanol. A final 20 mL of 2-propanol was added to the centrifuge tube, which was then subjected to sonication for 30 minutes. This process resulted in suspension of the black solid in the 2-propanol.

To prepare electrodes from the black suspension, highly oriented pyrolytic graphite (HOPG) samples were cut into squares ~ 8mm x 8mm. The HOPG was polished with 400 grit SiC polishing paper on a wet polishing wheel for 10 minutes. The polished HOPG was cleaned by sonication in isopropanol and then acetone for 10 minutes. Next, a 30 μL drop of the mixed composition suspension of Mo and Se was placed onto the polished side of a HOPG substrate. The sample was dried for 18 hours in a vacuum desiccator with an internal pressure of < 100 mTorr.

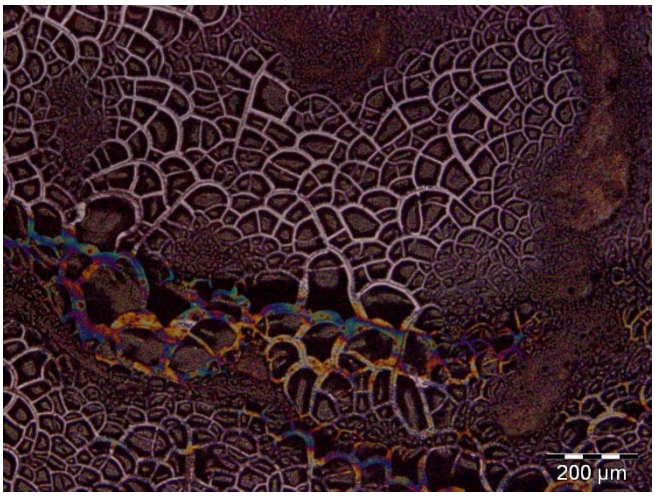


Figure 2.21. Light microscope image of drop casted amorphous mixture of a mixture prepared by mixing ammonium heptamolybdate with sodium selenide. The suspension was dropcast on HOPG and dried under vacuum for 18 hours.

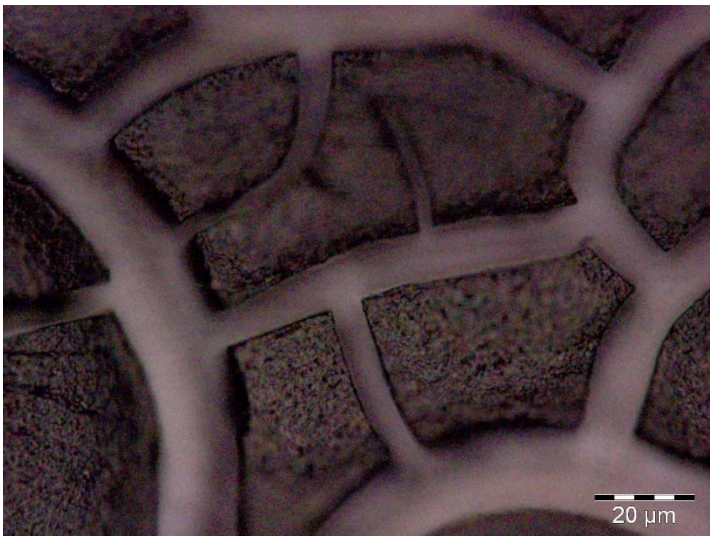


Figure 2.22. High magnification light microscope image of drop casted amorphous mixture of a mixture prepared by mixing ammonium heptamolybdate with sodium selenide. The suspension was dropcast on HOPG and dried under vacuum for 18 hours.

As is clearly visible in Figure 2.21 and Figure 2.22, the drop-casted black suspension of Mo and Se compounds did not result in the formation of a uniform film. The film appears to have cracked upon drying and has formed a number of raised domains with dimensions of approximately 20-50 microns.

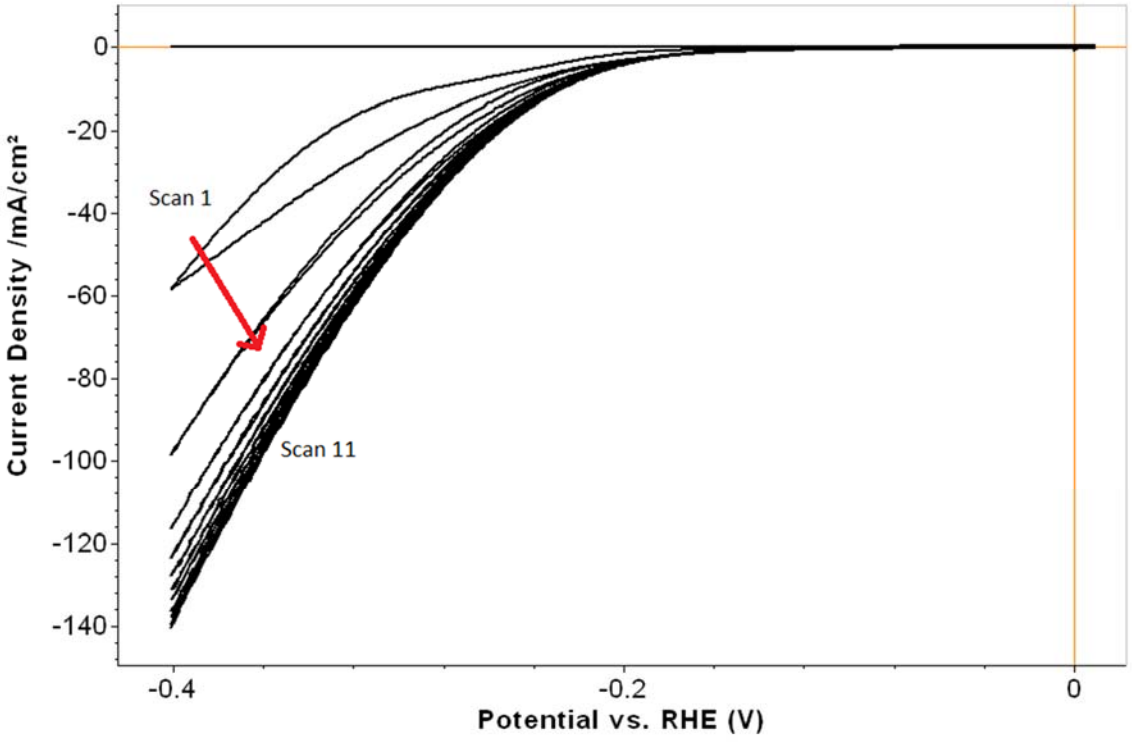


Figure 2.23. Cyclic voltammetry scans in 1 M $H_2SO_4$ of dropcasted $MoSe_2$ precursors. With each scan, the catalytic ability of the film increases and the overpotential for HER decreases. After ~11 scans, the catalysis nearly stops improving with each subsequent scan.

Figure 2.23 shows the method used to convert the dropcasted film of $MoSe_2$ precursor into a catalytic film. The film was cycled in 1.0 M $H_2SO_4$ at a scan rate of 10 mV/s from -0.4 Volts vs. RHE to 0.01 Volts versus RHE. The first scan showed poor catalysis for hydrogen

evolution, requiring nearly 300 mV to drive the hydrogen evolution reaction at 10 $mA/cm^2$. The overpotential increased with each subsequent scan until scan 11, at which time the overpotential for HER was -0.223 V. It was this prepared sample which was used for the pH and morphology studies from earlier in this chapter.

## 2.7. References

1. Saadi, F. H.; Carim, A. I.; Velazquez, J. M.; Baricuatro, J. H.; McCrory, C. C. L.; Soriaga, M. P.; Lewis, N. S., Operando Synthesis of Macroporous Molybdenum Diselenide Films for Electrocatalysis of the Hydrogen-Evolution Reaction. *ACS Catalysis* **2014,** *4* (9), 2866-2873.

2. Sobczynski, A., Molybdenum disulfide as a hydrogen evolution catalyst for water photodecomposition on semiconductors. *Journal of Catalysis* **1991,** *131* (1), 156-166.

3. Hinnemann, B.; Moses, P. G.; Bonde, J.; Jørgensen, K. P.; Nielsen, J. H.; Horch, S.; Chorkendorff, I.; Nørskov, J. K., Biomimetic Hydrogen Evolution: MoS2 Nanoparticles as Catalyst for Hydrogen Evolution. *Journal of the American Chemical Society* **2005,** *127* (15), 5308-5309.

4. Benck, J. D.; Hellstern, T. R.; Kibsgaard, J.; Chakthranont, P.; Jaramillo, T. F., Catalyzing the Hydrogen Evolution Reaction (HER) with Molybdenum Sulfide Nanomaterials. *ACS Catalysis* **2014,** *4* (11), 3957-3971.

5. Hu, S.; Xiang, C.; Haussener, S.; Berger, A. D.; Lewis, N. S., An analysis of the optimal band gaps of light absorbers in integrated tandem photoelectrochemical water-splitting systems. *Energy & Environmental Science* **2013,** *6* (10), 2984-2993.

6. Jaramillo, T. F.; Jørgensen, K. P.; Bonde, J.; Nielsen, J. H.; Horch, S.; Chorkendorff, I., Identification of Active Edge Sites for Electrochemical H2 Evolution from MoS2 Nanocatalysts. *Science* **2007,** *317* (5834), 100-102.

7. Li, Y.; Wang, H.; Xie, L.; Liang, Y.; Hong, G.; Dai, H., MoS2 Nanoparticles Grown on Graphene: An Advanced Catalyst for the Hydrogen Evolution Reaction. *Journal of the American Chemical Society* **2011,** *133* (19), 7296-7299.

8. Carmo, M.; Fritz, D. L.; Mergel, J.; Stolten, D., A comprehensive review on PEM water electrolysis. *International Journal of Hydrogen Energy* **2013,** *38* (12), 4901-4934.

9. Walter, M. G.; Warren, E. L.; McKone, J. R.; Boettcher, S. W.; Mi, Q.; Santori, E. A.; Lewis, N. S., Solar Water Splitting Cells. *Chemical Reviews* **2010,** *110* (11), 6446-6473.

10. McKone, J. R.; Lewis, N. S.; Gray, H. B., Will Solar-Driven Water-Splitting Devices See the Light of Day? *Chemistry of Materials* **2014,** *26* (1), 407-414.

11. Hu, S.; Shaner, M. R.; Beardslee, J. A.; Lichterman, M.; Brunschwig, B. S.; Lewis, N. S., Amorphous TiO2 coatings stabilize Si, GaAs, and GaP photoanodes for efficient water oxidation. *Science* **2014,** *344* (6187), 1005-1009.

12. Lichterman, M. F.; Sun, K.; Hu, S.; Zhou, X.; McDowell, M. T.; Shaner, M. R.; Richter, M. H.; Crumlin, E. J.; Carim, A. I.; Saadi, F. H.; Brunschwig, B. S.; Lewis, N. S., Protection of inorganic semiconductors for sustained, efficient photoelectrochemical water oxidation. *Catalysis Today* **2016,** *262*, 11-23.

13. Sun, K.; Saadi, F. H.; Lichterman, M. F.; Hale, W. G.; Wang, H.-P.; Zhou, X.; Plymale, N. T.; Omelchenko, S. T.; He, J.-H.; Papadantonakis, K. M.; Brunschwig, B. S.; Lewis, N. S., Stable solar-driven oxidation of water by semiconducting photoanodes protected by transparent catalytic nickel oxide films. *Proceedings of the National Academy of Sciences* **2015,** *112* (12), 3612-3617.

14. Morales-Guio, C. G.; Liardet, L.; Mayer, M. T.; Tilley, S. D.; Grätzel, M.; Hu, X., Photoelectrochemical Hydrogen Production in Alkaline Solutions Using Cu2O Coated with Earth-Abundant Hydrogen Evolution Catalysts. *Angewandte Chemie International Edition* **2015,** *54* (2), 664-667.

15. Choi, J. G.; Thompson, L. T., XPS study of as-prepared and reduced molybdenum oxides. *Applied Surface Science* **1996,** *93* (2), 143-149.

**C h a p t e r 3**

# 3. Evidence of Small Molecule Dithiol Binding on Macroscopic Edges of Synthetic Single Crystal Molybdenum Selenide

## 3.1.Abstract

The behavior of $MoSe_2$ single crystals was investigated upon exposure to small molecule dithiol and thiol ligands. Ordinary Raman data shows localization of 1,2-benzenedithiol (1,2-BDT) to macroscopic edges of $MoSe_2$ single crystals. The small molecule dithiol is found to bind as a singly protonated thiolate or dithiolate because of the absence of a strong υ(SH) signal in the Raman spectra. The sulfur-hydrogen stretching signal υ(SH), present at 2531 $cm^{-1}$ in purified samples of 1,2-BDT, is nearly absent and greatly diminished in intensity in the spectrum of macroscopic $MoSe_2$ edges of the functionalized samples. XPS experiments showed the presence of 1,2-BDT following crystal treatment and desorption occurs upon annealing to 300°C. Raman mapping provided a visual method to image edges where ligand localization was present and provided a route to probe for > 1 μm defects within single crystal samples.

## 3.2. Introduction

Photoelectrochemical behavior of semiconductor electrodes used in the generation of solar fuels can be improved through surface control. Surface modification of n-silicon with protective layers such as $TiO_2$ and graphene[1-4] has been shown to decrease corrosion rates for photoanodes when compared to the corresponding unprotected semiconductor electrodes.

Recent work on p-silicon highlights the ability to modify band edge positions that may allow for higher photovoltages and improved performance of silicon photocathodes. Functionalization of $MoS_2$ and $MoSe_2$ has been demonstrated through various routes[5] with edge selective functionalization being observed in single layer samples under ultra-high vacuum conditions. $MoS_2$ functionalized with differing polyethylene glycol ligands (neutral, anionic, and cationic) can be dispersed in aqueous media for 3 weeks while the non-functionalized semiconductor materials remain insoluble. The same functionalization route has a strongly negative effect on hydrogen evolution reaction performance.[6]

An ideal functionalization method of transition metal dichalcogenide materials would allow for the modulation of band edge positions while simultaneously controlling surface recombination rates and catalytic properties. Herein, we report an investigation of selective edge site binding of molybdenum diselenide by thiol ligands.

Detailed experimental procedures are provided in the experimental methods section later in this chapter. Briefly, single crystal $MoSe_2$ was grown by a chemical vapor transport method in an evacuated quartz ampoule in a three-zone tube furnace utilizing selenium tetrachloride as a transport agent. $MoSe_2$ crystals were removed from the ampoule and their compositions were confirmed by X-ray photoelectron spectroscopy (XPS). The crystals were characterized further by Raman spectroscopy, scanning electron microscopy (SEM) and energy dispersive x-ray spectroscopy (EDS). The characterized $MoSe_2$ single crystals were exposed to a solution of 1,2-benzeneditihol (1,2-BDT) in an inert atmosphere glove box. Functionalization was confirmed by XPS and Raman spectroscopy.

### 3.3.Results and Discussion

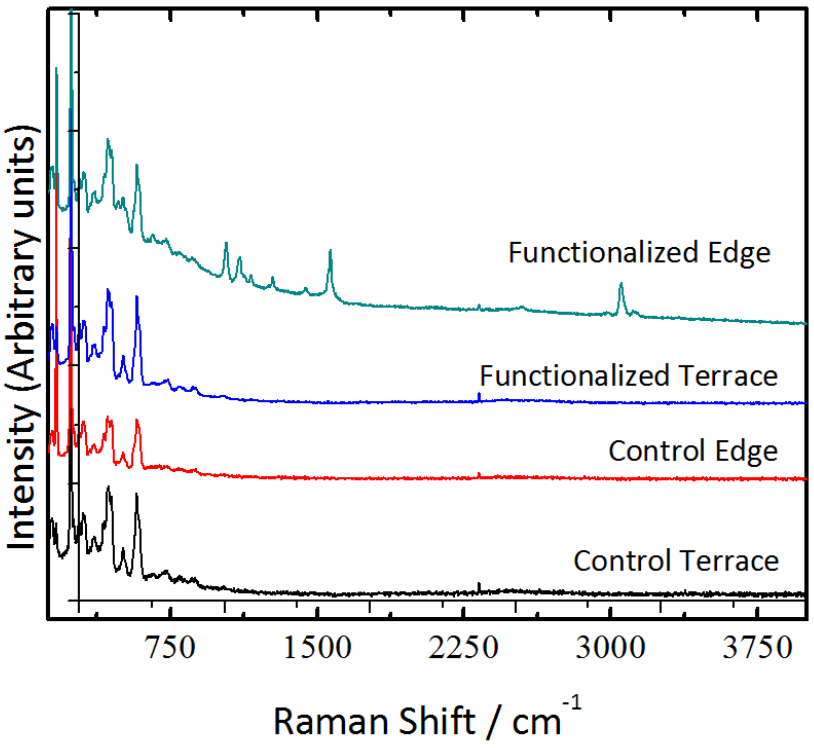


Figure 3.1. Raman intensity as a function of measured Raman shift in $cm^{-1}$ for two regions of a $MoSe_2$ single crystal. The top two traces are for different regions of a crystal exposed to 100 mM 1,2-benzenedithiol in THF. The bottom two traces are for an edge domain and terrace domain on a $MoSe_2$ single crystal which was exposed to THF in the absence of 1,2-benzenedithiol.

Figure 3.1 shows the Raman intensity as a function of Raman shift for $MoSe_2$ single crystals exposed to 100 mM solutions of 1,2-benezedithiol and compared to a control sample. A Raman scan of the $MoSe_2$ crystal which had been exposed to pure THF without 1,2-benzenedithiol provides a spectrum with few features between 750 $cm^{-1}$ and 3750 $cm^{-1}$. However, when the

Raman microscope probes a macroscopic step edge which is visible under optical magnification, the spectrum shows multiple sharp features between 750 $cm^{-1}$ and 3750 $cm^{-1}$.

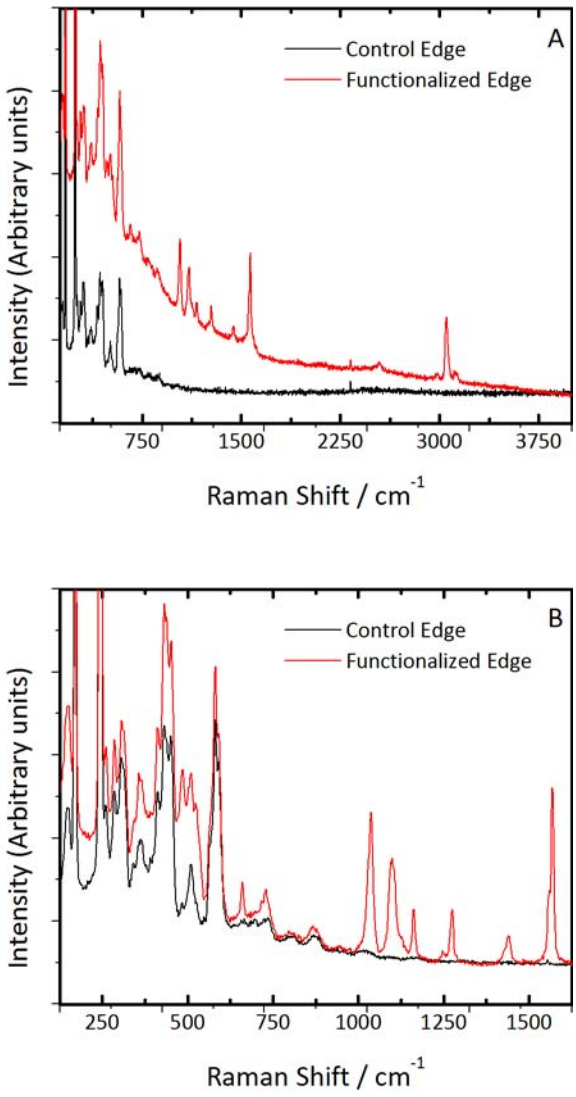


Figure 3.2. Raman intensity as a function of measured Raman shift ($cm^{-1}$) at a macroscopic edge on single crystal $MoSe_2$. The traces show data for the functionalized edge (red) and a non-functionalized edge (black). In (A) one can see the entire spectral region of Raman probing. In (B) one can see in detail the region from 100-1600 $cm^{-1}$

Figure 3.2 highlights distinctions between a functionalized $MoSe_2$ edge and a control edge. The spectral features for the functionalized $MoSe_2$ edge are detailed in Table 1. Comparing the measured Raman resonances of functionalized $MoSe_2$ step edges and 1,2-BDT found in other forms, the form of 1,2-benzenedithiol ligand present at the step edges most closely resembles that of a singly protonated or completely unprotonated molecule. Cho et al[7] demonstrated the ability to determine the nature of the adsorbate in the case of 1,2-BDT on silver particles. Evidence of 1,2-BDT existing as the deprotonated dianion 1,2-benzenedithiolate was seen in the absence of the ν(SH) sulfur-hydrogen stretching mode. The ordinary Raman spectrum of pure 1,2-BDT shows a strong and broad signal at 2531 $cm^{-1}$ indicating the presence of the sulfur hydrogen motif in the molecule( Figure 3.3). However, when 1,2-BDT is placed in 6M sodium hydroxide to deprotonate the thiols, the strong spectral feature near 2539 $cm^{-1}$ is no longer present. The loss of ν(SH) upon adsorption of 1,2-BDT to silver films supported the claim of 1,2-BDT binding as the deprotonated dianion 1,2-benzenedithiolate. In the case of 1,2-BDT binding to $MoSe_2$ edge sites, a similar argument can be made. Upon adsorption to macroscopic edge sites of $MoSe_2$, the strong ν(SH) stretch is no longer present in the Raman spectrum. This suggests that 1,2-BDT is binding selectively to $MoSe_2$ edge sites as 1,2-benzenedithiolate.

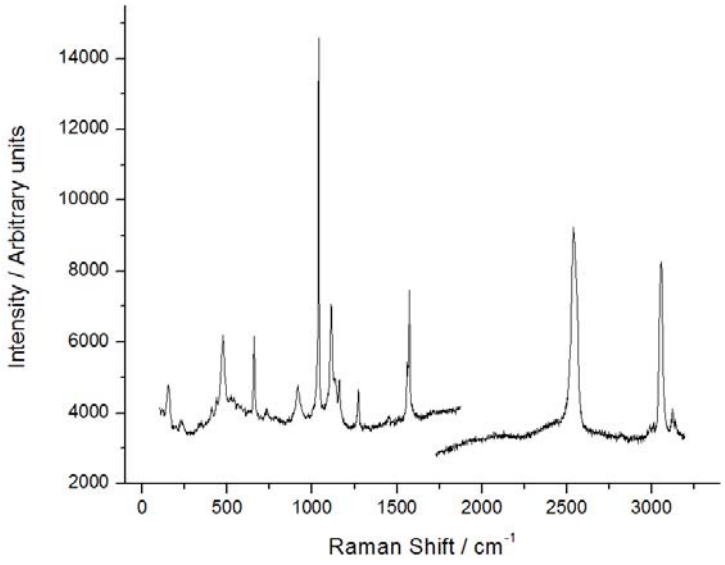


Figure 3.3. Raman spectrum of 1,2-benzenedithiol taken as two separate spectra between 100 cm-1 and 1800 cm-1 and 1500 cm-1 and 3200 cm-1. Note the large ν(S-H) stretching frequency present at 2531 cm-1.

**Table 1. Raman resonances at step edges of $MoSe_2$ are compared to previous studies with 1,2-BDT**

| *Signal* | *$MoSe_2$ 1,2-BDT*[a] | *1,2-BDT*[b] | *1,2-BDT*[c] | *$Ag_2$(1,2-BDT)*[d] |
|---|---|---|---|---|
| 1 | 1038 | 1038 | 1029 | 1034 |
| 2 | 1100 | 1113 | 1095 | 1087 |
| 3 | 1165 | 1159 | 1157 | 1160 |
| 4 | 1275 | 1273 | 1246 | 1261 |
| 5 | 1442 | 1452 | 1432 | 1433 |
| 6 | 1568 | 1572 | 1556 | 1563 |
| 7 | - | 2531 | - | - |
| 8 | 3054 | 3054 | 3045 | 3043 |

[a]Functionalized $MoSe_2$.
[b]For full spectrum see supporting information
[c]1,2-BDT in 6 M NaOH
[d]Cho et al. *Vibrational Spectroscopy,* 10(**1996**) 261-270.

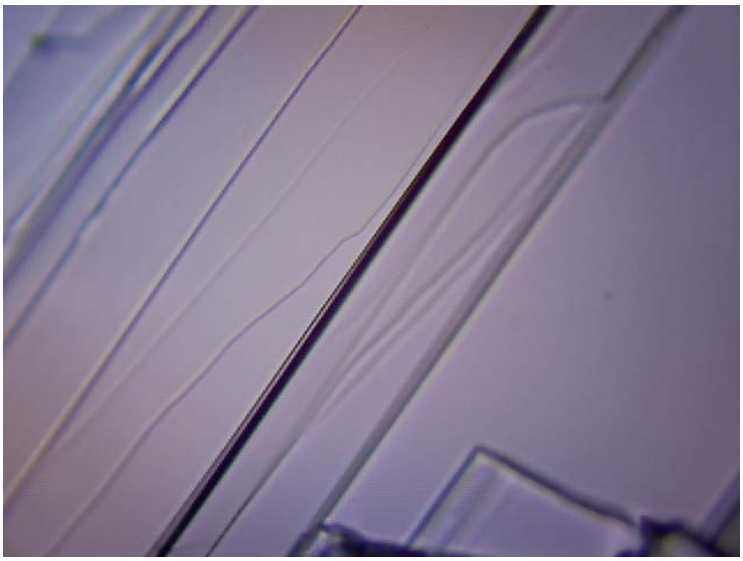

Figure 3.4. Raman sampling location for spectra from Figure 3.1. This location corresponds to the location for data acquired for control edge spectra. Spectra were acquired from center ~20 pixels of each image at 20x magnification.

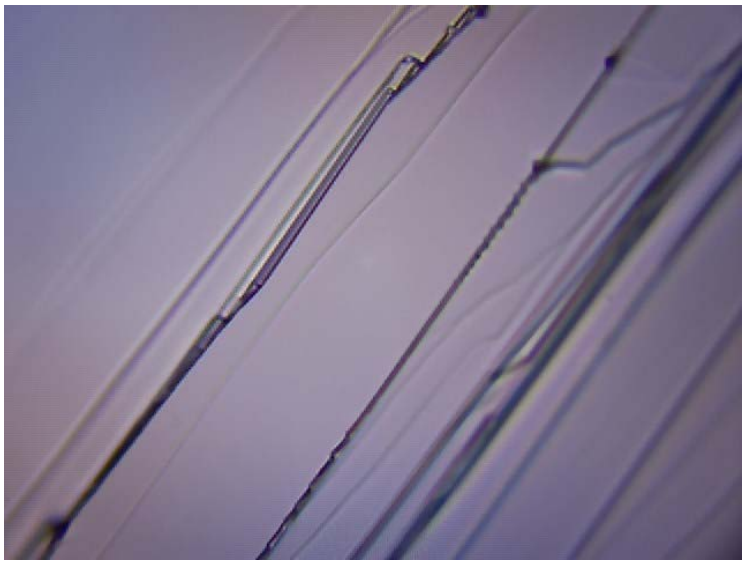

Figure 3.5. Raman sampling location for spectra from Figure 3.1. This location corresponds to the location for data acquired for the control terrace spectra. Spectra were acquired from center ~20 pixels of each image at 20x magnification.

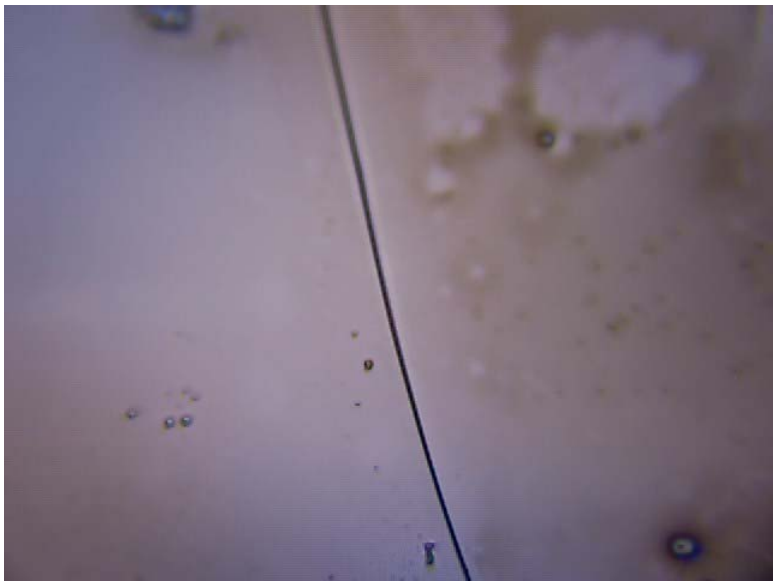

Figure 3.6. . Raman sampling location for spectra from Figure 3.1. This location corresponds to the location for data acquired for the functionalized edge spectra. Spectra were acquired from center ~20 pixels of each image at 20x magnification.

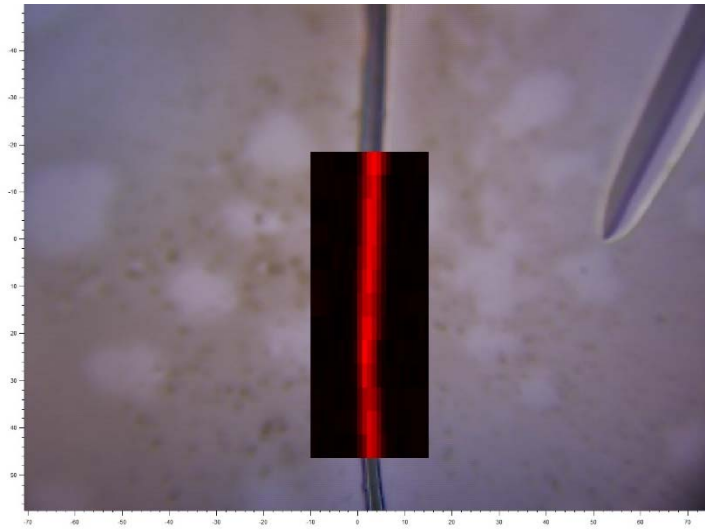

Figure 3.7. Raman mapping data of functionalized $MoSe_2$ edge. This data was collected by measuring Raman intensity at 1039 $cm^{-1}$ while rastering in 1 μm steps in the horizontal direction and 5 μm steps in the vertical direction. 960 spectra were collected in total. Red indicates areas of high Raman intensity while black indicates areas of low Raman intensity.

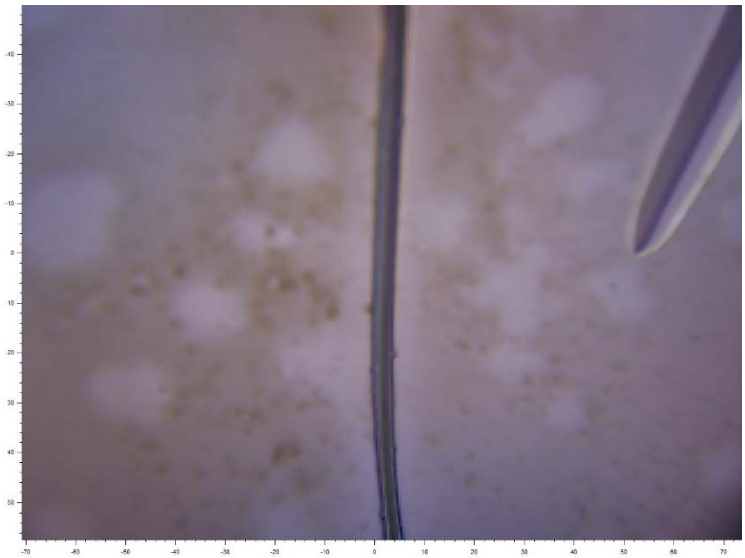

Figure 3.8. The area sampled in Figure 3.7 without the Raman mapping data overlay.

The selection of $MoSe_2$ as substrate and aromatic thiols as binding ligands has allowed for the characterization of the binding behavior of 1,2-BDT by X-ray photoelectron spectroscopy. If samples of TMDCs with sulfur as the chalcogen were chosen instead of selenium, the sulfur atoms inherent in the $MS_2$ material would interfere with measuring the presence of 1,2-BDT. Figure 3 shows the results of an annealing experiment on $MoSe_2$ single crystals which had been exposed to 1,2-BDT and subsequently annealed within an ultra-high vacuum chamber. Following our standard 1,2-BDT treatment procedure, $MoSe_2$ single crystal samples were transferred to an ultra-high vacuum chamber that functioned as part of a Kratos Axis Ultra. XPS measurements were collected prior to each annealing step and then following the final anneal at 300ºC. Figure 3 shows the XPS data collected on a 1,2-BDT treated $MoSe_2$ sample after annealing to 100ºC, 200ºC, and 300ºC. Following heating to 100ºC in UHV, the intensity of the S 2p signal is stabilized and reduced from that of the initial measurement (see SI) taken immediately upon transferring the sample into the instrument. The four fitted peaks

present in Figure 3a are the Se $3p^{3/2}$ centered at 160.65 eV, Se $3p^{1/2}$ at 166.3 eV, S $2p^{3/2}$ at 163.6 eV, and S $2p^{1/2}$ at 164.7 eV. The spectrum show relative intensities for each relevant sulfur and selenium peak remains essentially unchanged following a subsequent heating to 200ºC. Peak positions in Figure 3b are Se $3p^{3/2}$ is at 160.7 eV, Se $3p^{1/2}$ at 166.3 eV, S $2p^{3/2}$ at 163.6 eV, and S $2p^{1/2}$ at 164.7 eV. Following the final annealing step to 300ºC, the S 2p signal is no longer present, and what remains is a Se $3p^{3/2}$ signal at 160.9 eV and Se $3p^{1/2}$ signal at 166.7. Interesting to note is the slight shift of both Se 3p signals to slightly higher binding energy, by approximately 0.2 eV, after the loss of 1,2-benzenedithiol.

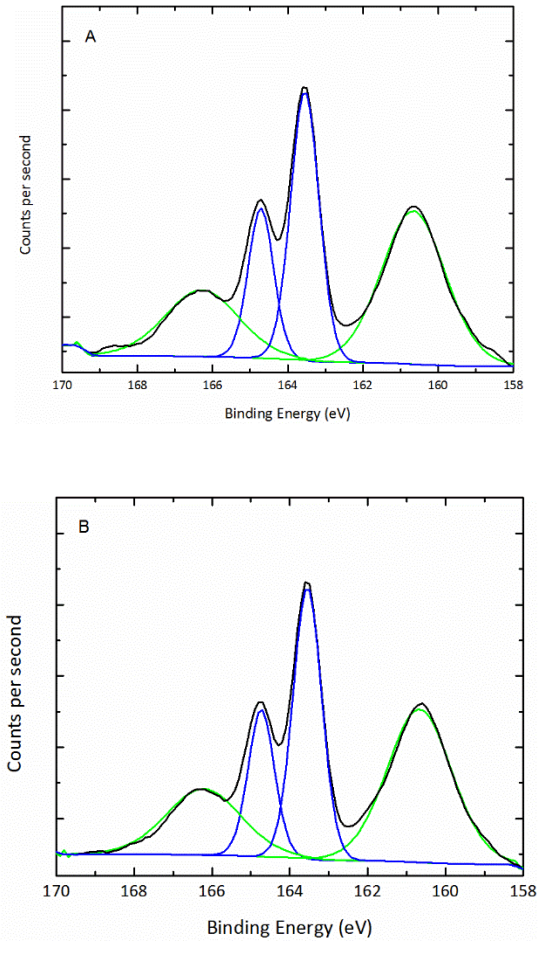

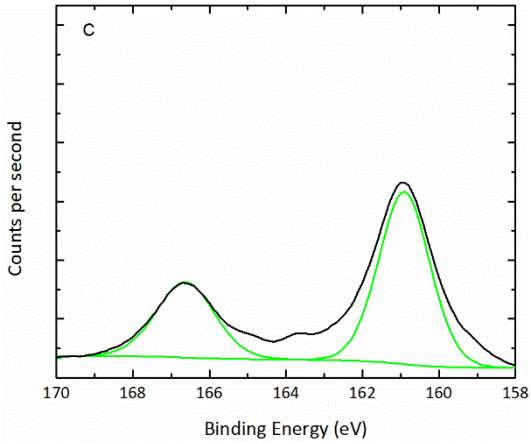


Figure 3.9. XPS spectra of $MoSe_2$ exposed to 1,2-BDT and annealed to (A) 100°C, (B) 200°C, and (C) 300°C. The blue trace is fitted as a sulfur 2p peak and the light green trace is the selenium 3d signal.

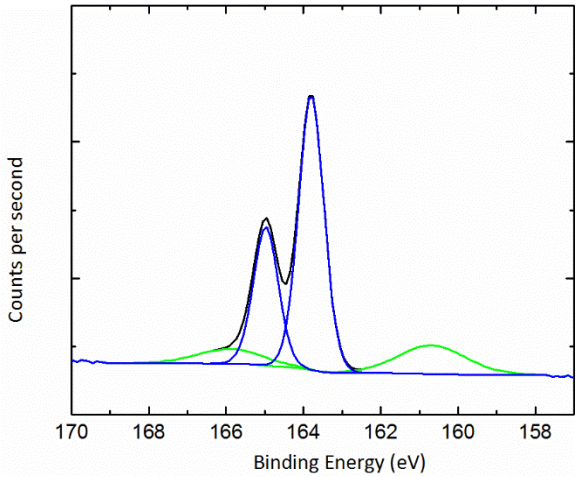


Figure 3.10. Displays the S 2p region of a $MoSe_2$ crystal treated with 1,2-BDT and immediately after transfer into the XPS chamber. The blue trace (S 2p) has an intensity much higher than would be expected from an adsorbed monolayer and is present on the surface with an intensity of approximately 10:1 the intensity of the Se 3p signal.

## 3.4. Exploring the binding of additional small molecules to $MX_2$'s

In addition to exploring benzenedithiol binding to $MoSe_2$, we explored a collection of additional small molecule ligands in search of an explanation of the observed selective binding phenomenon. In this section I'll describe raman mapping experiments with $WSe_2$ exposed to dithiols like ethane-1,2-dithiol, propane-1,3-dithiol, monothiols 4-fluorobenzenethiol and 4-trifluoromethylbenzenethiol, and pyrocatechol. The structures of explored ligands are shown in Figure 3.11.

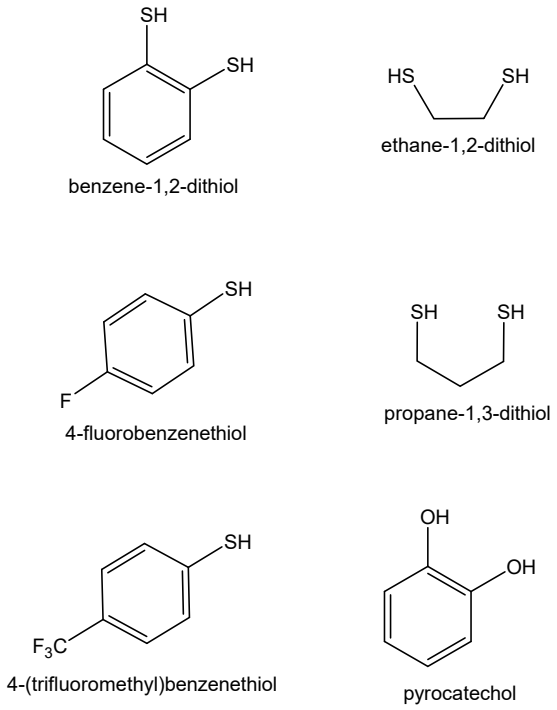


Figure 3.11. Small molecules exposed to $WSe_2$ and probed by Raman spectroscopy.

First, 1,2-dihydroxybenzene (1,2-DHB), the alcohol analogous to 1,2-benzenedithiol was explored. A freshly exfoliated single crystal of $WSe_2$ was immersed in a 100 mMolar solution

of 1,2-DHB in THF for 10 minutes. Next, the crystal was washed with THF and ultrapure water. The samples were immediately taken to the Raman microscope and studied with ordinary Raman and mapping techniques.

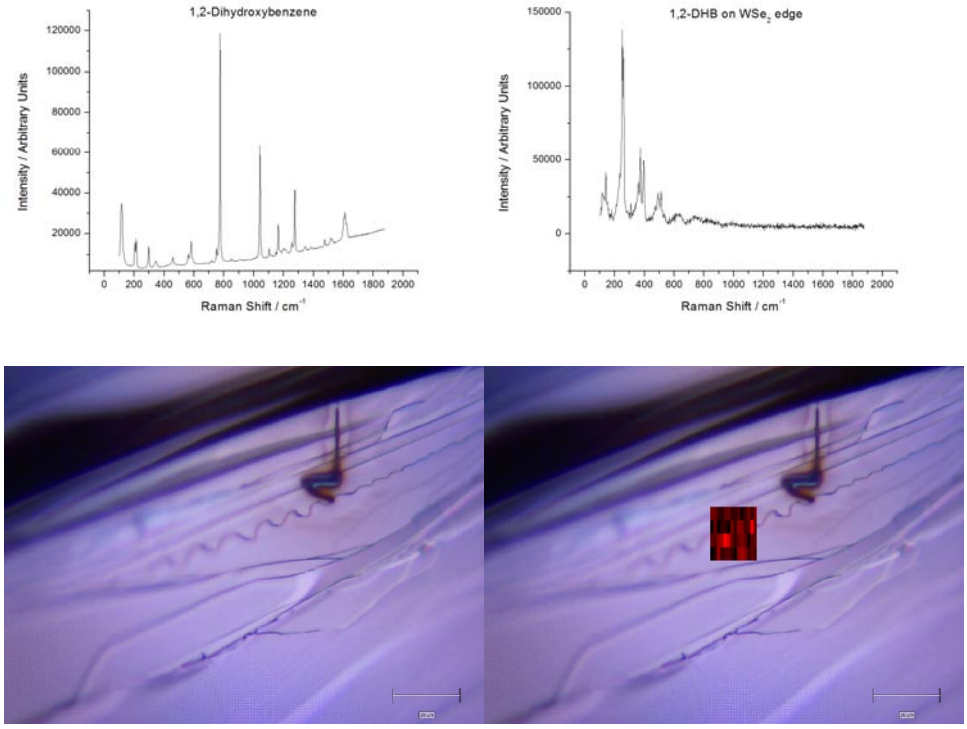


Figure 3.12. Raman spectrum of 1,2-dihydroxybenzene (top left), Raman point scan of a $WSe_2$ macroscopic edge following treatment with 1,2-DHB (top right). Mapping area without data overlay (bottom left). Raman mapping area with data overlay (bottom right).

The Raman spectrum of 1,2-DHB was used to select an appropriate Raman shift to perform mapping experiments. A strong resonance at 774 $cm^{-1}$ was chosen as the resonance to explore using Raman mapping. The laser was rastered across the surface of the $WSe_2$ crystal and a Raman spectrum was collected at each laser spot. Unlike the mapping data for 1,2-BDT, there was no apparent localization of 1,2-DHB on the macroscopic edge sites of $WSe_2$. This is seen also by point scans of macroscopic edges as can be seen in Figure 3.12 (top right). None of the

resonances attributable to 1,2-DHB can be found in the spectrum taken at a macroscopic edge site. Many locations were sampled for this experiment. By Raman spectroscopy, none of the samples locations showed any indication of selective localization of 1,2-DHB to the macroscopic edge sites of $WSe_2$.

Next, we explored mono-thiol ligands to probe whether selective edge-site binding is present in select ligands. $WSe_2$ samples exposed to 100 mMolar 4-fluorobenzenethiol (4-FBT) showed no evidence of selective binding to macroscopic edge sites. Spectra were collected on multiple terrace sites and edge sites, and there was no detectable presence of 4-FBT on either terrace or edge sites. Figure 3.13 shows the Raman spectra collected at a terrace site (left) and macroscopic edge site (right) on $WSe_2$ exposed to 4-FBT.

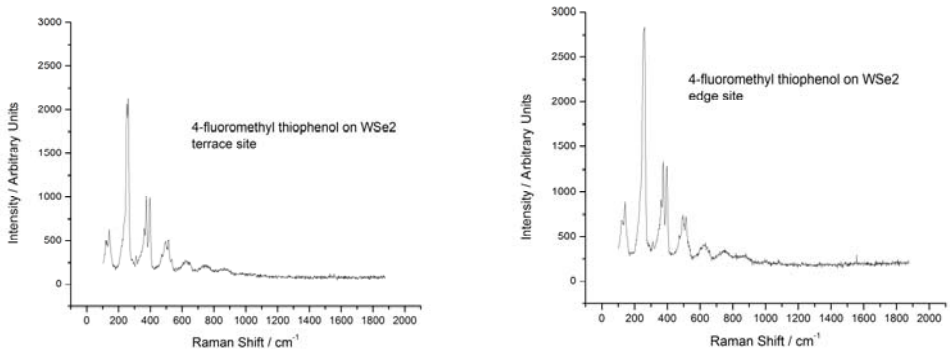


Figure 3.13. Raman spectrum of $WSe_2$ single crystal exposed to 4-FBT. Raman spectrum acquired of a terrace site (left) and a macroscopic edge site (right).

The results of the Raman data collected for a variety of small molecule ligands exposed to $WSe_2$ is shown in Table 1. Among them, only 1,2-benzenedithiol was found to bind selectively to macroscopic edge sites of $WSe_2$.

| Ligand | Macroscopic ddge-site binding by Raman to $WSe_2$ |
|---|---|
| 1,2-benzenedithiol | Yes |
| 1,2-dihydroxybenzene | No |
| 4-fluorothiophenol | No |
| 4-(trifluoromethyl)thiophenol | No |
| Ethane-1,2-dithiol | No |
| Propane-1,3-dithiol | No |
| Trifluorotoluene | No |

Table 1. Summary of Raman data exploring ligand binding to macroscopic edges of $WSe_2$.

## 3.5.Conclusions

In conclusion, 1,2-BDT binds selectively to macroscopic edge-sites of $MoSe_2$. This binding is not uniform over the entire surface of $MoSe_2$ single crystals as localized Raman data pinpoints the localization at macroscopic step edges and 1,2-BDT was not detectable by Raman spectroscopy on terrace sites. The bound ligand takes the form of a mono-protonated thiolate or doubly-deprotonated benzenedithiolate during binding as evidenced by the absence of a strong ν(SH) signal in the Raman spectra. Complete desorption occurs following anneal to 300$^{o}$C in an ultra-high vacuum environment. $WSe_2$ was used to explore the binding of additional small

molecules to edge-sites of $MX_2$ crystals. Again, 1,2-benzenedithiol was found to bind selectively to macroscopic edge sites based on raman point scan and mapping data. However, for a range of additional small molecules, none provided evidence suggesting selective binding to edge sites. Additional work exploring adsorbates and their effects on carrier recombination rates and catalysis may allow elucidation of the generality of this functionalization method and its usefulness for transition metal dichalcogenide protection.

## 3.6. Materials and Methods

Materials:

Quartz tubing was obtained from GM associates. Water was obtained from a Barnstead Nanopure system and had a resistivity ≥ 18.0 MΩ-cm. Molybdenum powder (99.99%, Sigma-Aldrich) and selenium pellets (99.999%, Sigma-Aldrich) were used as received. 1,2-benzenedithiol (97%, Alfa Aesar) was vacuum sublimated prior to use. Selenium tetrachloride (99%, Sigma-Aldrich) was used as received and replaced 2 months after opening. Tetrahydrofuran (anhydrous, Aldrich) was stored in an inert atmosphere glovebox and used as received. All other chemicals were used as received unless otherwise noted.

Crystal Synthesis:

Single crystal samples of $MoSe_2$ were grown by a chemical vapor transport technique.[8-11] Quartz ampules were prepared from various diameter quartz tubing. Tubes were sealed at one end with a hydrogen/oxygen torch and then were soaked in a standard base bath (300 g potassium hydroxide, 4 L isopropyl alcohol, 1 L water) for 12 hours. The ampules were then washed with ultrapure water and acetone 5 times.

Polycrystalline $MoSe_2$ was prepared by first loading a 25 mm inner diameter quartz ampule with a stoichiometric mixture of Mo and Se using 2.000 grams of molybdenum powder and 3.291 grams of selenium pellets. The ampoule was evacuated to $< 1.0 \times 10^{-3}$ torr and sealed with a natural gas/oxygen flame. The sealed ampule was then heated to 900ºC for 24 hours in a single-zone Lindberg heavy-duty tube furnace.

A 1.000 gram sample of polycrystalline $MoSe_2$ powder was placed in a quartz ampoule along with $SeCl_4$ and evacuated to $< 1.0 * 10^{-5}$ torr. An effort was made to restrict the reagents to one end of the ampule. The sealed ampule was placed in a two zone Carbolite tube furnace and heated for 24 hours at 1025 ºC in the growth zone and 975 ºC in the charge zone to clean the growth zone to prevent unwanted nucleation sites. The temperature gradient was then reversed producing a temperature of 975 ºC in the growth zone and 1025 ºC in the charge zone with a gradient of ~2 ºC $cm^{-1}$. After 7 days, several smooth, hexagonal shaped platelets of crystalline $MoSe_2$ as large as 10 mm on a side were obtained. Several growths of crystalline $MoSe_2$ were attempted using the above procedure. Each growth yielded crystalline material, but only a few growths produced a large quantity of crystals that were of the appropriate size for study. Crystals were that were not used immediately were stored in an inert atmosphere glove box.

Functionalization procedure:

In a typical procedure, a single crystal sample of $MoSe_2$ was transferred to an inert atmosphere glove box and exfoliated with a strip of adhesive tape to reveal a fresh crystal surface. The sample is immersed in a 100 mmolar solution (10 mL) of 1,2-benzenedithiol in THF for 10 minutes. The sample is removed from the solution, rinsed with THF, and removed from the

glovebox. Next, the $MoSe_2$ sample is washed thrice with ultrapure water, dried with a stream of $N_2$, and immediately transported to the XPS instrument and pumped into the ultra-high vacuum environment.

Instrumentation:

X-ray photoelectron spectroscopic (XPS) data were collected at ~5 × 10−9 Torr using a Kratos AXIS Ultra DLD with a magnetic immersion lens that consisted of a spherical mirror and concentric hemispherical analyzers with a delay-line detector (DLD). An Al Kα (1.486 KeV) monochromatic source was used for X-ray excitation. Ejected electrons were collected at a 90° angle from the horizontal. The CASA XPS software package v 2.3.16 was used to analyze the collected data. Raman spectra were collected with a Renishaw Raman microscope at λ=532 nm through an objective with numerical aperture=0.75. The laser power was ~ 3 mW. Scanning electron microscope (SEM) images were obtained using a FEI Nova NanoSEM 450 at an accelerating voltage of 10.00 kV with a working distance of 5 mm and an in-lens secondary electron detector.

## 3.7.References

1. Hu, S.; Shaner, M. R.; Beardslee, J. A.; Lichterman, M.; Brunschwig, B. S.; Lewis, N. S., Amorphous TiO2 coatings stabilize Si, GaAs, and GaP photoanodes for efficient water oxidation. *Science* **2014,** *344* (6187), 1005-1009.

2. Lichterman, M. F.; Sun, K.; Hu, S.; Zhou, X.; McDowell, M. T.; Shaner, M. R.; Richter, M. H.; Crumlin, E. J.; Carim, A. I.; Saadi, F. H.; Brunschwig, B. S.; Lewis, N. S., Protection of inorganic semiconductors for sustained, efficient photoelectrochemical water oxidation. *Catalysis Today* **2016,** *262*, 11-23.

3. Nielander, A. C.; Bierman, M. J.; Petrone, N.; Strandwitz, N. C.; Ardo, S.; Yang, F.; Hone, J.; Lewis, N. S., Photoelectrochemical Behavior of n-Type Si(111) Electrodes Coated With a Single Layer of Graphene. *Journal of the American Chemical Society* **2013,** *135* (46), 17246-17249.

4. Nielander, A. C.; Thompson, A. C.; Roske, C. W.; Maslyn, J. A.; Hao, Y.; Plymale, N. T.; Hone, J.; Lewis, N. S., Lightly Fluorinated Graphene as a Protective Layer for n-Type Si(111) Photoanodes in Aqueous Electrolytes. *Nano Letters* **2016,** *16* (7), 4082-4086.

5. Presolski, S.; Pumera, M., Covalent functionalization of MoS2. *Materials Today* **2016,** *19* (3), 140-145.

6. Chou, S. S.; De, M.; Kim, J.; Byun, S.; Dykstra, C.; Yu, J.; Huang, J.; Dravid, V. P., Ligand Conjugation of Chemically Exfoliated MoS2. *Journal of the American Chemical Society* **2013,** *135* (12), 4584-4587.

7. Cho, S. H.; Lee, Y. J.; Kim, M. S.; Kim, K., Infrared and Raman spectroscopic study of 1,2-benzenedithiol adsorbed on silver. *Vibrational Spectroscopy* **1996,** *10* (2), 261-270.

8. Kline, G.; Kam, K.; Canfield, D.; Parkinson, B. A., Efficient and stable photoelectrochemical cells constructed with WSe2 and MoSe2 photoanodes. *Solar Energy Materials* **1981,** *4* (3), 301-308.

9. McKone, J. R.; Pieterick, A. P.; Gray, H. B.; Lewis, N. S., Hydrogen Evolution from Pt/Ru-Coated p-Type WSe2 Photocathodes. *Journal of the American Chemical Society* **2013,** *135* (1), 223-231.

10. J. Baglio, E. K., N. DeCola, C. Struck, J. Marzik, K. Dwight, A. Wold, Growth and Characterization of n-$WS_2$ and Niobium-Doped p-$WS_2$ Single Crystals. *Journal of Solid State Chemistry* **1983,** *49*, 166-179.

11. C. Koval, J. O., Preparation and Electrochemical Characterization of $WSe_2$ Electrodes having a wide Range of Doping Densities. *J. Electroanal. Chem.* **1987,** *234*, 133-143.

**C h a p t e r 4**

# 4. Exploring the Growth of Atomic Layer Deposited Metal Oxides on Transition Metal Dichalcogenide Semiconductors

## 4.1.Abstract

Explored was the growth of titanium dioxide ($TiO_2$) nanoparticles on exfoliated and otherwise prepared samples of transition metal dichalcogenides semiconductors. Atomic layer deposited $TiO_2$ does not form a conformal film on $MoSe_2$, $WSe_2$, or $MoS_2$ single crystals. Instead, nanoparticles of $TiO_2$ nucleate and form on the surface. These nanoparticles are loosely adhered to the surface and can be removed with a high-pressure air stream, or brushing the surface with a kimwipe. ALD-$TiO_2$ nanoparticles form. Electrochemical cycling of potential between -0.1 V and 1.5 V under one-sun illumination results in the loss of nanoparticles from the surface and corrosion of the $MX_2$ single crystal.

## 4.2.Introduction

Transition metal dichalcogenide semiconductors ($MX_2$) are a class of materials with a wealth of useful properties for use in solar energy conversion devices. Depending on the composition of the transition metal (M = Mo, W) or the chalcogen (X = S, Se, Te) the band gap $E_g$ for $MX_2$ materials can vary from approximately 1.0 eV to 2.1 eV, enabling the efficient absorption of light in either a single-junction or tandem device. $MX_2$ semiconductors are also quite chemically stable and are resistant to corrosion. These materials have been known for years

to be efficient light absorbers for use in photoelectrochemical cells. $WSe_2$ was studied in detail throughout the 1980s and was found to exhibit stability as well as >17% photoelectrochemical energy-conversion efficiencies while in contact with aqueous polyhalide redox systems.[1-5] However, the ability to stabilize $MX_2$ photoanodes in aqueous solution without the addition of high concentrations of halide has never been realized because of high rates of carrier recombination and corrosion which occurs when edge-site are not passivated.

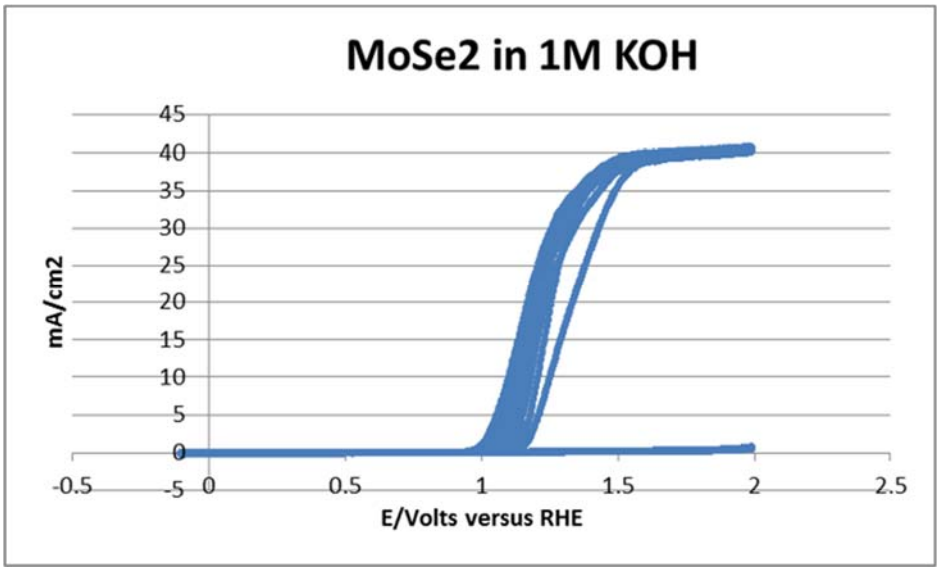


Figure 4.1. Cyclic voltammogram of n-$MoSe_2$ under dark and one sun illumination in 1 M KOH. The lower curve is the dark current and the upper curves are current under 1 sun illumination. This looks like a fantastic photoanode, however no oxygen evolution bubbles are visible and the result to the electrode is significant etching and surface pitting.

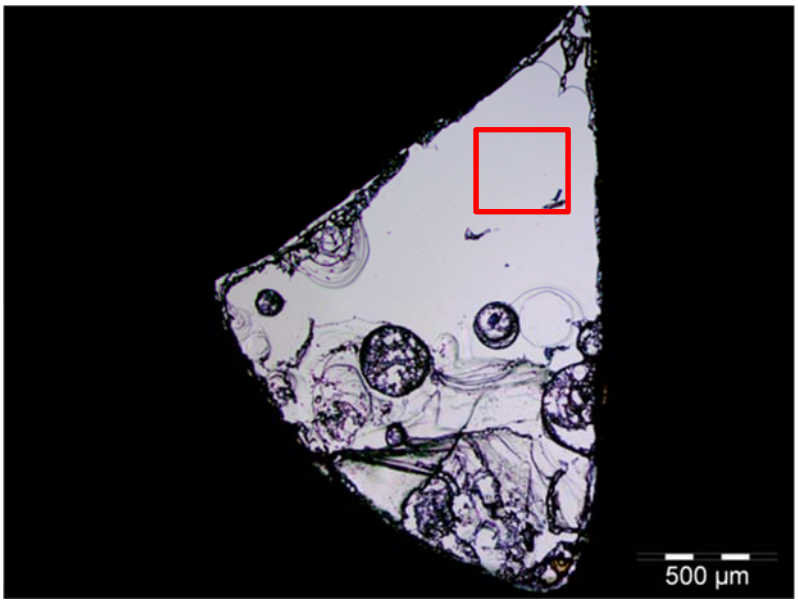


Figure 4.2. Microscope image of the n-$MoSe_2$ electrode in Figure 4.1 after cyclic voltammetry under 1 sun illumination. Take note of the high level of pitting and corrosion on the electrode surface.

Figure 4.1 shows a Cyclic voltammogram of n-$MoSe_2$ under dark and one sun illumination in 1 M KOH. The lower curve is the dark current and the upper curves are current under 1 sun illumination. Under this experimental setup, one observes a high amount of photocurrent and a great fill factor, suggesting this is an excellent photoanode. However, oxygen evolution does not occur, as no bubbles are observed on the surface of the electrode under operation. Additionally, following the cyclic voltammetry experiment, there is a significant amount of visible pitting and corrosion on the surface of the electrode. This is contrasted with the electrode prior to cyclic voltammetry in which the entire electrode was smooth roughly uniform under the microscope, looking like the region contained within the red box of Figure 4.2. Without additional modification, n-$MoSe_2$ single crystals are unsuitable for use as oxygen evolving photanodes in a solar fuels device.

## 4.3. Atomic layer deposition as a protection method for small band-gap semiconductors

A method has recently been developed to protect silicon photoanodes with a thick layer, 3-150 nm, of titanium oxide ($TiO_2$) deposited by atomic layer deposition (ALD).[6] This protection method has proven to be rather general, providing the ability to protect not only silicon but other materials susceptible to corrosion under anodic conditions such as GaAs, GaP, CdTe and InP.[7] The band gaps of several successfully protected photoanode materials is seen in **Error! Reference source not found.**. Traditionally, metal oxide photoanodes were capable of oxidizing water to $O_2$ in alkaline and acidic media, but were unable to bring about the transformation efficiently because of their large band gaps and highly positive valence-band-edge position. The photons from a large portion of the solar spectrum thermalize and do not contribute to solar energy conversion. Protecting smaller band gap semiconductors with $TiO_2$ expands the photoanode toolkit to include lower band gap materials and subsequently, higher energy conversion efficiencies. Since the transition metal dichalcogenides span a wide range of available band gaps, 1.0-2.1 eV, being able to protect this class of semiconductors would greatly increase the number of accessible absorbers with ideal band gaps.[8]

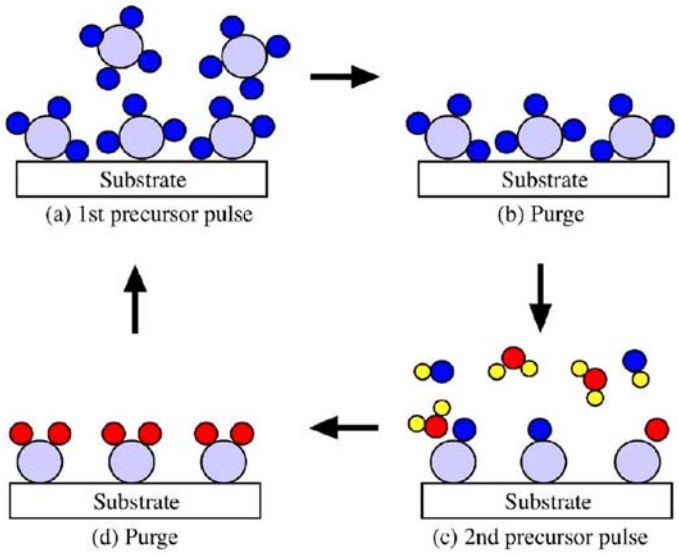


Figure 4.3. The atomic layer deposition (ALD) process.

Figure 4.3 shows the steps involved in the process of atomic layer deposition. The first step is exposing the substrate surface to precursor pulse, causing the substrate to react in a self-limiting fashion to the substrate and depositing one single-layer of precursor. In this cartoon, the precursor is a tetra functional transition metal precursor such as tetrakisdimethylamido titanium $Ti(NH_2)_4$, also known as TDMAT. The excess precursor is then purged by way of a vacuum pump in the second step of the process. In the third step, a second precursor pulse is used to bond with reactive sites from the previous precursor which is adhered to the substrate. In this case, water is used to react with the $Ti(NH_2)_x$ species on the surface to form titanium hydroxides. In the final step, the excess precursor and other volatiles are removed under vacuum. This completes one cycle of atomic layer deposition and leaves a surface, which is primed for additional cycles of the deposition. A beneficial feature of this technique is the self-limiting nature of the process. Water and TMEDA are extremely reactive towards one another and if

they were both introduced to the reaction chamber at the same time, would react rapidly, generating mostly ammonia and titanium dioxide. However, because each precursor is introduced to the chamber only after the previous precursor has been evacuated from the reaction chamber, reactivity only occur at the surface of the substrate. This property allows for the generation of conformal metal oxide coatings to a variety of surfaces.

### 4.4. ALD on transition metal dichalcogenides surfaces

We wanted to explore whether ALD could be used to grow conformal thin films of metal oxides on single crystals of transition metal dichalcogenides semiconductors. The goal of the work was to determine if these metal oxide films could serve to protect $MX_2$'s from corrosion when used as photoanodes. Like in the previous chapters of this thesis, single crystals were grown by chemical vapor transport. Sample surfaces were prepared by exfoliation of the top layers of the crystal by use of adhesive tape. The newly exposed, pristine surfaces were immediately loaded into an ALD instrument and pumped down to 100 mTorr. $TiO_2$ was deposited by atomic-layer deposition (ALD) at 150 °C using tetrakis(dimethylamido)titanium (TDMAT) as the Ti source heated to 75 °C and $H_2O$ as the O source. Cycles were performed with pulse and purge times of 0.1 s and 15 s for the TDMAT, respectively and 0.015 s and 15 s for the $H_2O$ respectively, with the $H_2O$ pulse beginning each new cycle. The results of the deposition are shown below.

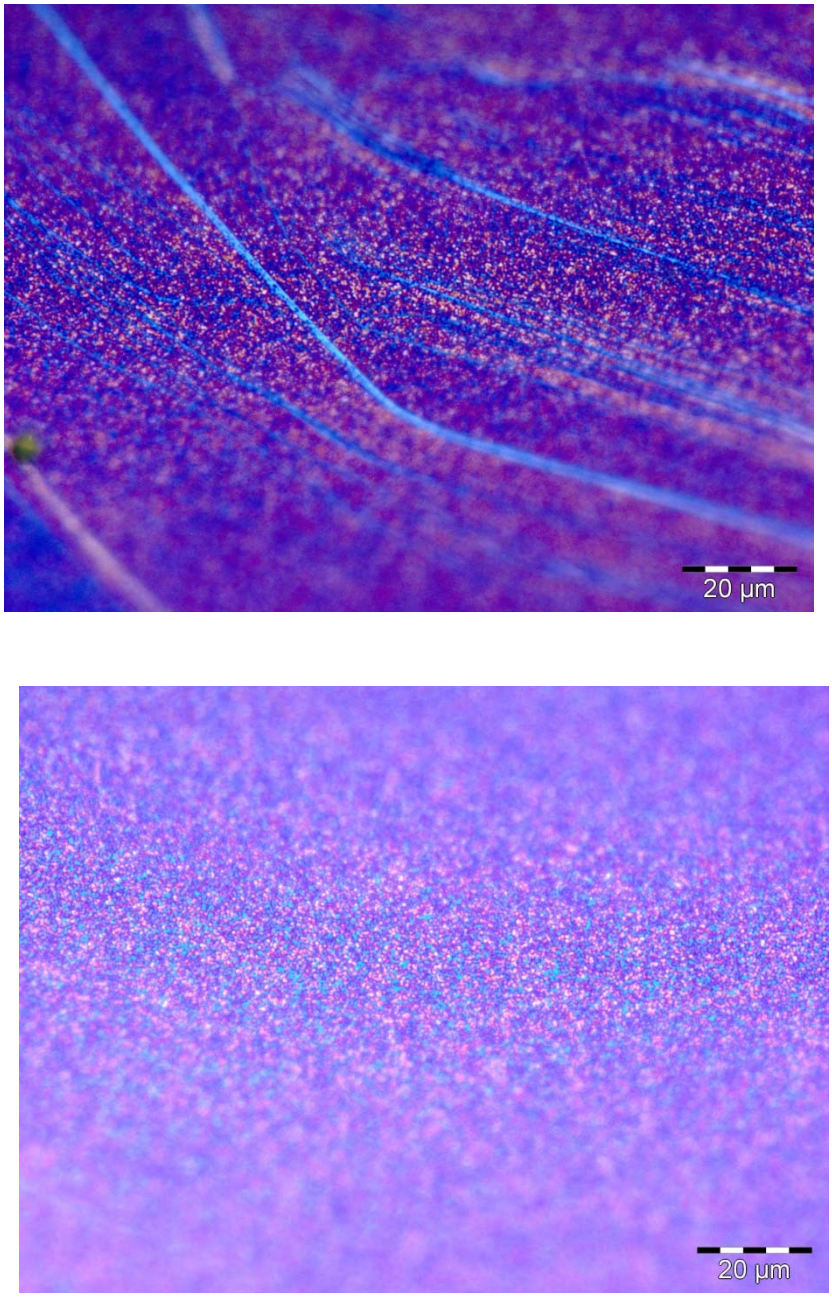


Figure 4.4. Light microscope image of 1000 ALD cycles alternating $H_2O$, TDMAT on n-$MoSe_2$.

Figure 4.4 shows the light microscope images of an n-$MoSe_2$ single crystal following 1000 cycles of ALD-$TiO_2$. These are real-color images without polarization filters. Little information can be gleaned from these images. High resolution SEM provides information that is more relevant. Figure 4.5 and Figure 4.6 show SEM images of various regions of the n-$MoSe_2$ substrate following 1000 cycles of ALD-$TiO_2$. In Figure 4.5, one can observe wavy regions of varying brightness, indicating varying electron conductivity. All of the regions possess a grainy appearance. Under higher magnification in Figure 4.6, two regions show the cause of the grainy appearance in lower magnification image. Nanoparticles are present on the substrate surface, with some of the nanoparticles apparently in contact with adjacent particles while others are present without contact with adjacent particles. The right image in Figure 4.6 shows a small section of the substrate in which a triangular tiling pattern forms with the nanoparticles on the sample surface. Triangular tiling is one of the three regular tilings of the plane. Dark triangular sections composed of many $TiO_2$ nanoparticles contrast with those sections containing few or no nanoparticles. A statistical analysis was completed of the nanoparticles visible in SEM images from the samples seen in Figure 4.6. Nanoparticles that were not in contact with adjacent particles were included in the statistical analysis. Twenty-one particles were included and showed a size distribution of $217 \pm 16$ nm diameter for the particles. The particles, which are connected to adjacent particles, appear to be roughly the same size, but this cannot be known with certainty based on the SEM images alone.

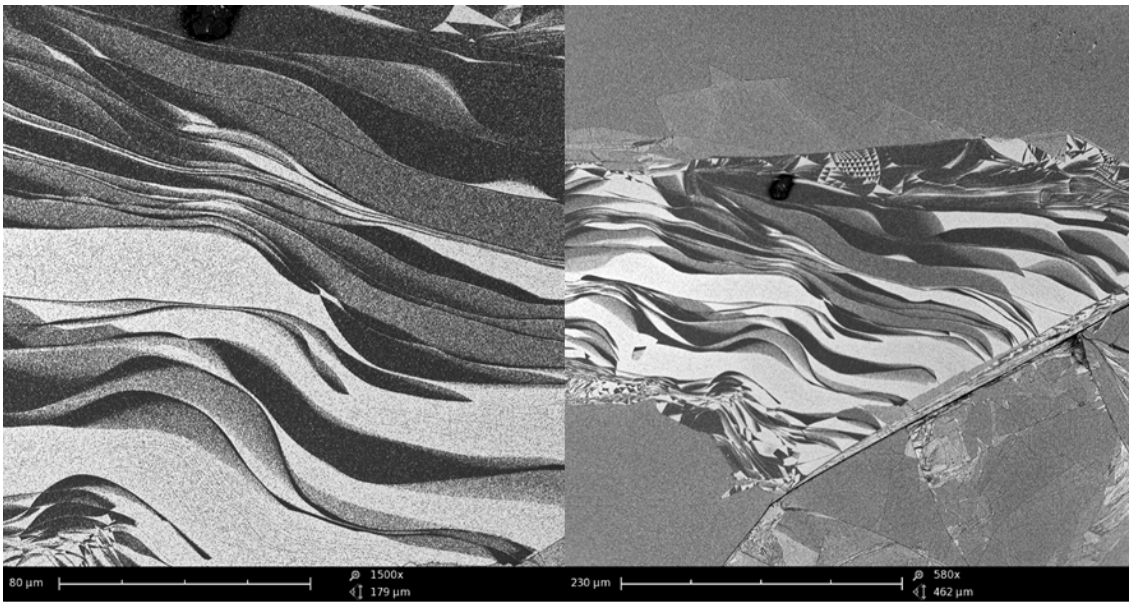


Figure 4.5. SEM images of a highly patterned region of n-$MoSe_2$ after 1000 cycles of ALD-$TiO_2$. This type of patterning was found only a small portion of the sample. The majority of the sample was roughly uniform in apprearance both under light-microscope and under SEM imaging.

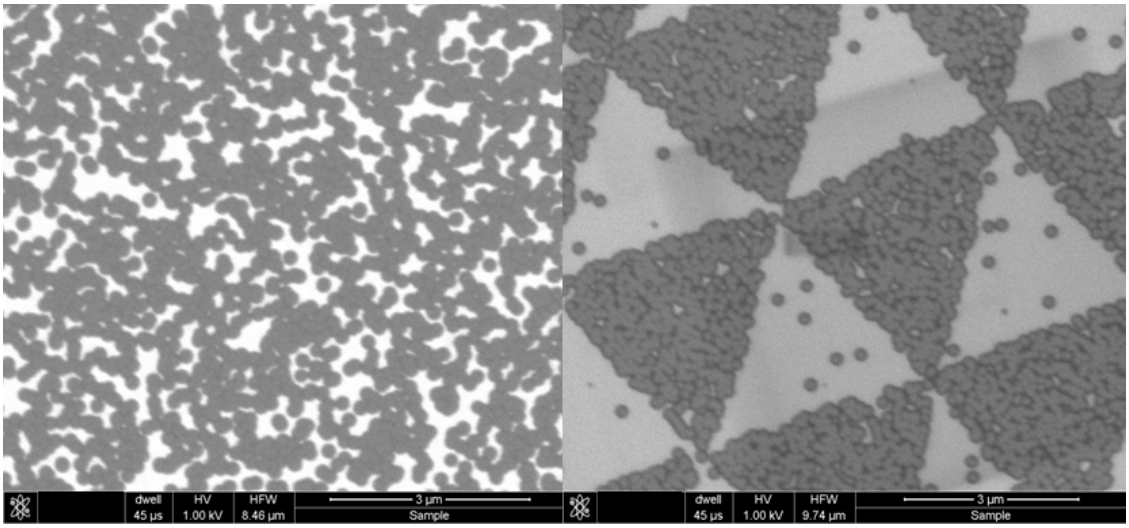


Figure 4.6. High resolution SEM showing two different regions of n-$MoSe_2$ after 1000 cycles of ALD-$TiO_2$.

To characterize these nanoparticle-coated substrates further, XPS was used to determine surface composition. Figure 4.7 shows the XPS spectrum of the Mo 3d (left) and Ti 2p (right) regions on a sample of n-$MoSe_2$ following 1000 cycles of ALD-$TiO_2$. There is a strong signal for both titanium and molybdenum in the sample. XPS is a surface sensitive technique. If we generated a conformal coating of $TiO_2$ on $MoSe_2$ thicker than the escape depth of photoelectrons through $TiO_2$, we would expect not to see the molybdenum 3d signal in the XPS spectrum. For ALD-$TiO_2$ grown by using our experimental procedure, each cycle yields approximately 0.4 nm of thickness to the coating. For a typical growth on Si or GaAs, 1000 cycles would then yield a coating with approximately 400 nm of thickness. Four hundred nm is far higher than the escape depth for photoelectrons for most materials (5-30 nm). Since there is a signal for the Mo 3d peak in the XPS spectrum, we can conclude that our film is not a conformal coating of $TiO_2$ on $MoSe_2$.

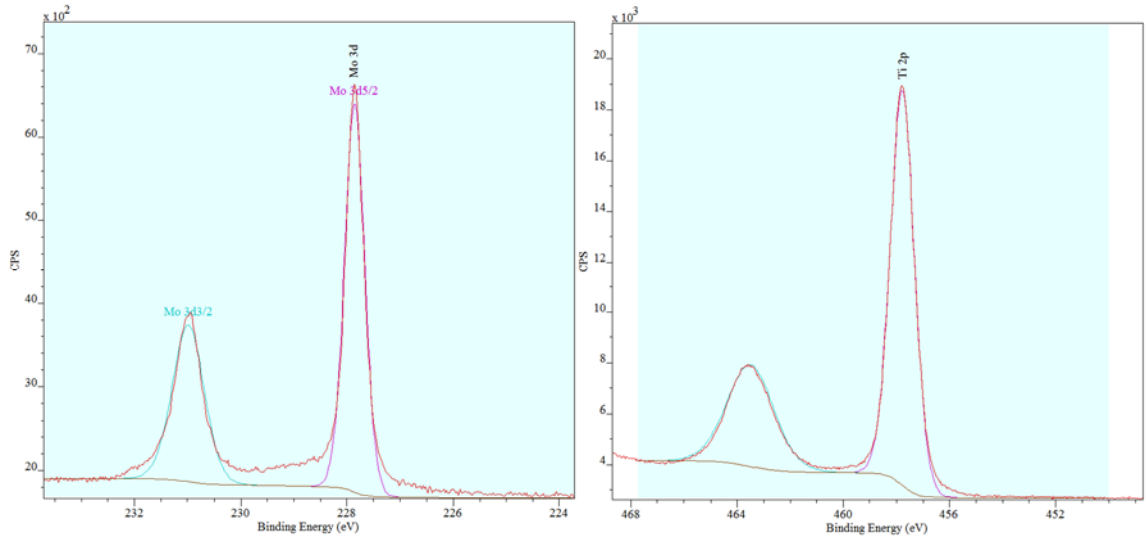


Figure 4.7. XPS spectrum of the Mo 3d (left) and Ti 2p (right) regions following 1000 cycles of ALD-$TiO2_2$ on n-$MoSe_2$.

To show further the $TiO_2$ coating isn't conformal on $MoSe_2$, an additional sample was prepared. This time, the $MoSe_2$ sample was exposed to 1700 cycles of ALD-$TiO_2$. The ratio of the Ti 2p region to the Mo 3d region in the XPS was compared for samples containing 1000 ALD cycles as well as 1700 ALD cycles. The XPS data is summarized in Figure 4.8. The ratio of area under the peak Mo 3d divided by the area under the Ti 2p peak does decrease when the number of ALD cycles increased from 1000 to 1700. However, a conformal ALD film with 1700 cycles could be expected to be ~680 nm in thickness and one would expect the Mo signal to approach zero. This would naturally place the Mo/Ti ratio near zero as well. This is not what we observe. Instead, when the SEM data is considered, it appears we have an assortment of nanoparticles formed on the surface of $MoSe_2$, nucleating in what appears to be random fashion in some surface locations and nucleating in a more ordered fashion in other surface locations. The nature of what is causing the localization is explored in the following section.

| ***Sample*** | ***Element*** | ***Region*** | ***Peak Area*** | ***Ratio Mo/Ti*** | ***ALD cycles*** |
|---|---|---|---|---|---|
| 1 | Mo | 238-224 eV | 6779 | 0.35 | 1000 |
| 1 | Ti | 468-455 eV | 19164 | | 1000 |
| 2 | Mo | 238-224 eV | 4652 | 0.22 | 1700 |
| 2 | Ti | 468-455 eV | 21662 | | 1700 |

Figure 4.8. XPS data summary for two $MoSe_2$ exposed to different numbers of ALD-$TiO_2$ cycles. The ratio of Mo/Ti is the total area of the Mo 3d peak divided by the total area of the Ti 2p peak.

## 4.5. Electrochemical behavior of ALD-$TiO_2$ on $MX_2$ single crystals

We prepared electrodes from $MoSe_2$ single crystal samples coated with 960 cycles of ALD-$TiO_2$. These electrodes possessed a yellow surface appearance, and consisted of nanoparticles coating the crystal surface. Figure 4.9 shows the $MoSe_2$ after ALD. The film appears relatively uniform by optical microscopy. However, the film is fragile and the coating is damaged by brushing a kimwipe against the surface as seen in the right panel. The scratches are regions where the nanoparticles have been moved, exposing the bare $MoSe_2$ surface.

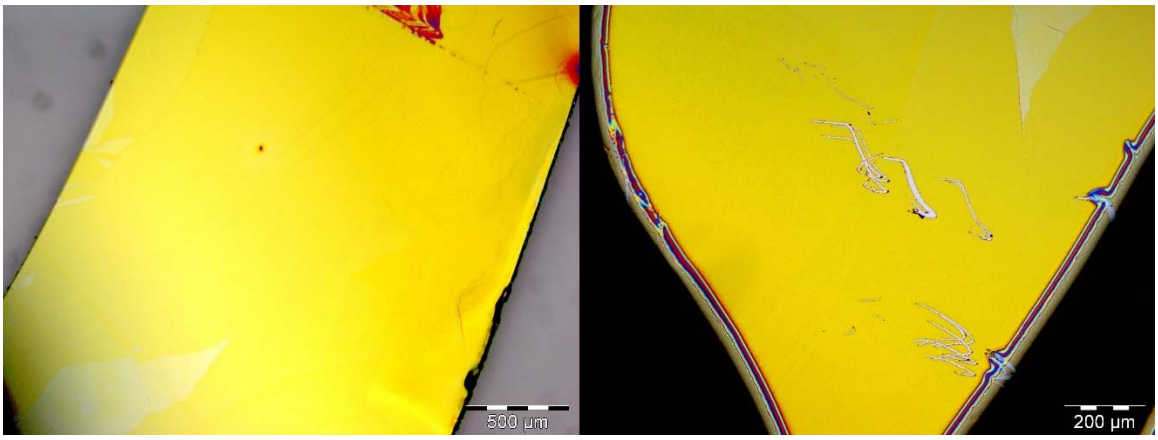


Figure 4.9 $MoSe_2$ single crystal following 960 cycles of ALD-$TiO_2$. The films are fragile and the surface coating can be displaced by brushing against the surface with a kimwipe.

The electrodes were cycled using cyclic voltammetry in 1.0 M KOH under dark and one sun illumination conditions. The first scan was completed in the dark and is labeled as dark in Figure 4.10. Current density at 1.5 V vs. RHE is less than 500 $\mu A/cm^2$. For the next two scans, labeled Light 1 and Light 2 respectively, the electrode was illuminated with 100 $mW/cm^2$ or 1 Sun illumination. The first light scan reached a current density of 2.57 $mA/cm^2$ and the

second light scan reached a higher current density of 3.37 mA/cm$^2$. Following these single CV sweeps, we viewed the electrode under an optical microscope.

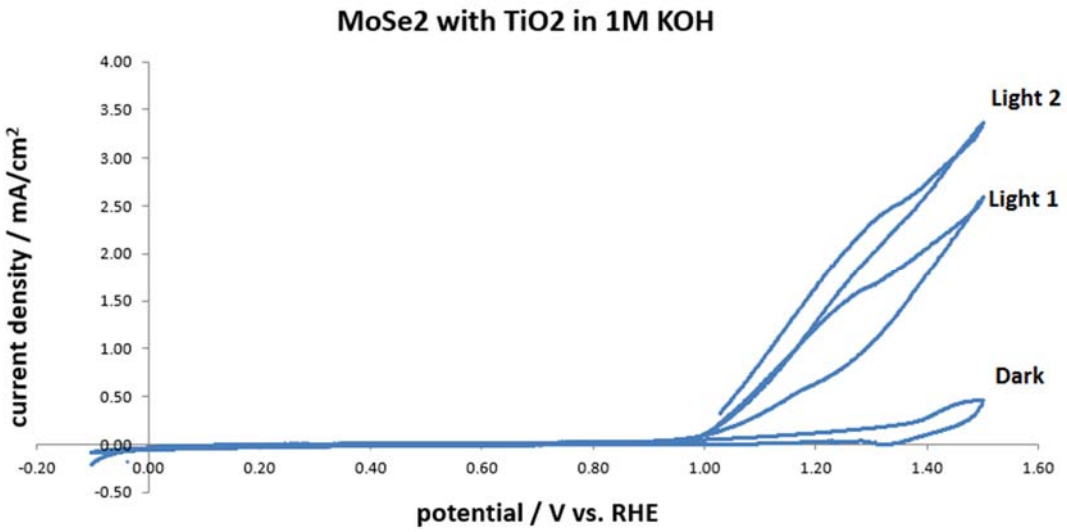


Figure 4.10 Cyclic voltammetry of $MoSe_2$ with 960 cycles of ALD-$TiO_2$. The dark scan was completed in low-light conditions. On the second scan, labeled light 1, the electrode was illuminated with 1 Sun. The final scan, labeled light 2 was also illuminated with one sun illumination. Current density increased between the two light scans.

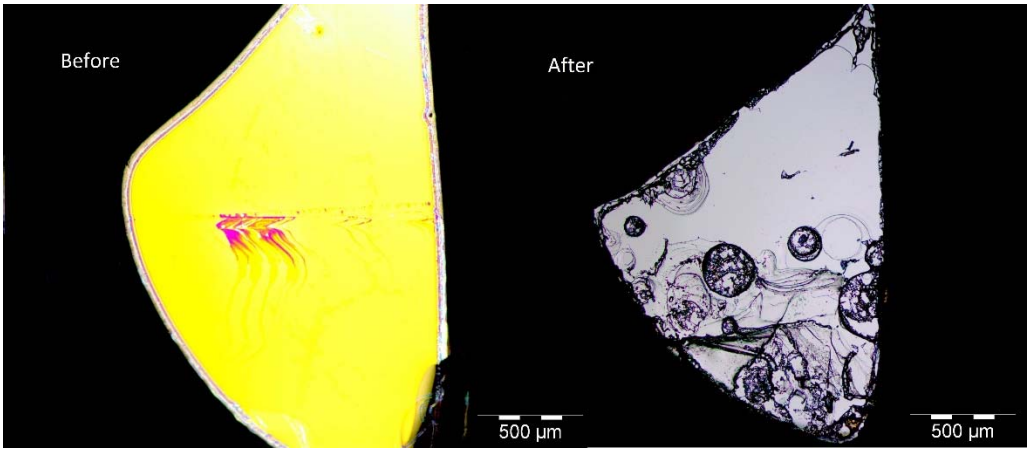


Figure 4.11 $MoSe_2$ electrode coated with ALD-$TiO_2$ before and after cycling for one hour in 1.0 M KOH. The electrode area was redefined with epoxy prior to cycling.

Observed under the optical microscope was a surface lacking the yellow appearance of the electrode prior to electrochemical experiments. Instead, there was pitting and corrosion of the surface. The $TiO_2$ nanoparticles, previously located on the surface are absent by XPS as there is no observable signal in the Ti 2p region of the spectrum.

## 4.6. Conclusions

Attempts to grow conformal thin films of $TiO_2$ on n-$MoSe_2$ by ALD did not yield the desired films. Instead of growing conformal films, nanoparticles of $TiO_2$ were formed on the surface. These nanoparticles adhered loosely to the terrace sites of single crystal $MoSe_2$ and were easily brushed away from the surface leaving a bare $MoSe_2$ surface. Under photoanodic conditions in alkaline media, $MoSe_2$ electrodes coated with ALD-$TiO_2$ rapidly corroded and the $TiO_2$ nanoparticles were lost from the surface. Thus, ALD grown $MoSe_2$ failed to protect the photoanodes from corrosion did not enable the use of $MoSe_2$ as an oxygen evolving photoanode in alkaline solution. Regions of single crystals with small terraces showed varying nanoparticle growth characteristics, in some cases with nanoparticles forming a triangular tile pattern. Investigations into the cause of these pattern formations and their relationship to defect density and terrace quality are ongoing.

## 4.7.References

1. Kline, G.; Kam, K.; Canfield, D.; Parkinson, B. A., Efficient and stable photoelectrochemical cells constructed with WSe2 and MoSe2 photoanodes. *Solar Energy Materials* **1981,** *4* (3), 301-308.

2. Schneemeyer, L. F.; Wrighton, M. S.; Stacy, A.; Sienko, M. J., N-TYPE MOLYBDENUM-DISELENIDE-BASED LIQUID-JUNCTION SOLAR-CELLS - A NON-AQUEOUS ELECTROLYTE SYSTEM EMPLOYING THE CHLORINE - CHLORIDE COUPLE. *Applied Physics Letters* **1980,** *36* (8), 701-703.

3. Parkinson, B. A.; Furtak, T. E.; Canfield, D.; Kam, K. K.; Kline, G., EVALUATION AND REDUCTION OF EFFICIENCY LOSSES AT TUNGSTEN DISELENIDE PHOTOANODES. *Faraday Discussions* **1980,** *70*, 233-+.

4. Prasad, G.; Srivastava, O. N., The high-efficiency (17.1%) WSe 2 photo-electrochemical solar cell. *Journal of Physics D: Applied Physics* **1988,** *21* (6), 1028.

5. Schneemeyer, L. F.; Wrighton, M. S., NORMAL-TYPE MOLYBDENUM DISELENIDE-BASED PHOTOELECTROCHEMICAL CELLS - EVIDENCE FOR FERMI LEVEL PINNING AND COMPARISON OF THE EFFICIENCY FOR CONVERSION OF LIGHT TO ELECTRICITY WITH VARIOUS SOLVENT-HALOGEN-HALIDE COMBINATIONS. *Journal of the American Chemical Society* **1980,** *102* (23), 6964-6971.

6. Hu, S.; Shaner, M. R.; Beardslee, J. A.; Lichterman, M.; Brunschwig, B. S.; Lewis, N. S., Amorphous TiO2 coatings stabilize Si, GaAs, and GaP photoanodes for efficient water oxidation. *Science* **2014,** *344* (6187), 1005-1009.

7. Lichterman, M. F.; Sun, K.; Hu, S.; Zhou, X.; McDowell, M. T.; Shaner, M. R.; Richter, M. H.; Crumlin, E. J.; Carim, A. I.; Saadi, F. H.; Brunschwig, B. S.; Lewis, N. S., Protection of inorganic semiconductors for sustained, efficient photoelectrochemical water oxidation. *Catalysis Today* **2016,** *262*, 11-23.

8. Hu, S.; Xiang, C.; Haussener, S.; Berger, A. D.; Lewis, N. S., An analysis of the optimal band gaps of light absorbers in integrated tandem photoelectrochemical water-splitting systems. *Energy & Environmental Science* **2013,** *6* (10), 2984-2993.

# A p p e n d i x A

## A. Synthesis and Polymerization Reactivity of Mono and Binuclear Titanium Constrained Half-Sandwich Olefin Polymerization Catalysts

This appendix serves as a route to document my work completed while serving as a graduate research assistant in the Agapie group from November 2010 to March 2013. Although this work is far-removed from the work in the Lewis group regarding transition metal dichalcogenides semiconductors and the scope of this thesis, I believe this is the most appropriate manner in which to document my prior synthetic work.

### A.1 Introduction

In terms of sheer volume, industrial polymers are among the most important man-made materials on earth; tens of millions of tons of various polymer materials are produced yearly.[1] Free-radical polymerization methods are currently employed in the synthesis of polyvinyl chlorides, polyacrylates, and others.[2] However, these methods do not allow for fine control over polymer features such as tacticity, polymer branching, insertion of polar monomers (appendix A), or molecular weight. Thus, there is much effort aimed at developing catalysts with enhanced olefin polymerization abilities.

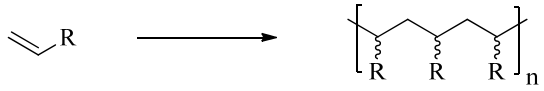


R = H, Alkyl, Halogen, OMe, $CO_2Me$, etc.

Figure A.1. Polymerization of non-polar and polar olefins.

The understanding of olefin polymerization catalysts has progressed significantly since the discoveries by Ziegler and Natta that heterogeneous combinations of $TiCl_4$ and $AlR_3$ (R = alkyl, aryl, hydride) are capable of generating high density polyethylene (HDPE) and isotactic polypropylene (iPP), though these catalysts are still used on an industrial scale.[3] One of the greatest advances in organometallic polymer chemistry was the development of well-defined, single-site organotransition metal olefin polymerization catalysts, such as the group 4 metallocenes (**A**, Figure A.2) and related systems including the half-sandwich amide type catalysts (**B**). These discoveries allowed for a deeper understanding of the factors controlling activity and selectivity of the catalyst.

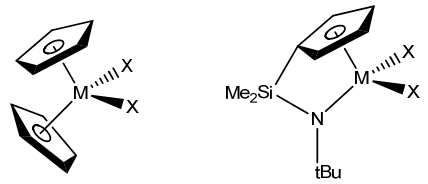


Figure A.2. Group 4 metallocenes (A) and constrained-geometry catalysts (B).

It is generally agreed that coordinatively unsaturated cationic alkyl complexes $[L_nMR]^+$ are the catalytically active species involved in polymerizations in these systems (Figure A.3). Several different routes to the catalytically active species $[L_nMR]^+$ are shown from the corresponding catalyst precursors (Figure A.3).

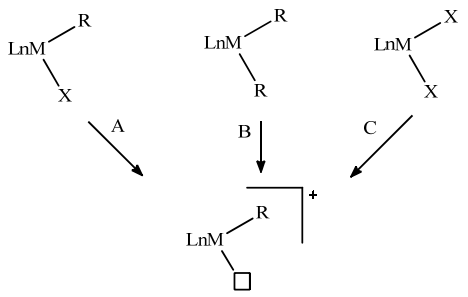


Figure A.3. Three different routes to a catalytically active species $[L_nMR]^+$ where the open coordination site on the metal is indicated by an open box.

Route A often involves silver of sodium abstraction of an anionic ligand, substituting it for a weakly coordinating anion such as $^-[B(3,5\text{-}(CF_3)_2C_6H_3)_4]$, $^-BF_4$, or $^-OTf$. Route B involves the abstraction of an alkyl anion from the metal center. Common reagents include $[Ph_3C][B(C_6F_5)_4]$, $[PhNHMe_2][B(C_6F_5)_4]$, and $[H(OEt_2)_2][B(3,5\text{-}(CF_3)_2C_6H_3)_4]$. Route C is a combination of alkylation followed by alkyl group abstraction. This can be done using either an alkylating reagent followed by an alkyl-abstracting agent or by a single reagent that accomplishes both. Partially hydrolyzed trimethylaluminum (methylaluminoxane or MAO) is a widely used reagent that can accomplish both of these processes. A review of activators and cocatalysts for metal catalyzed olefin polymerizations covers common reagents and proposed mechanisms in detail.[4]

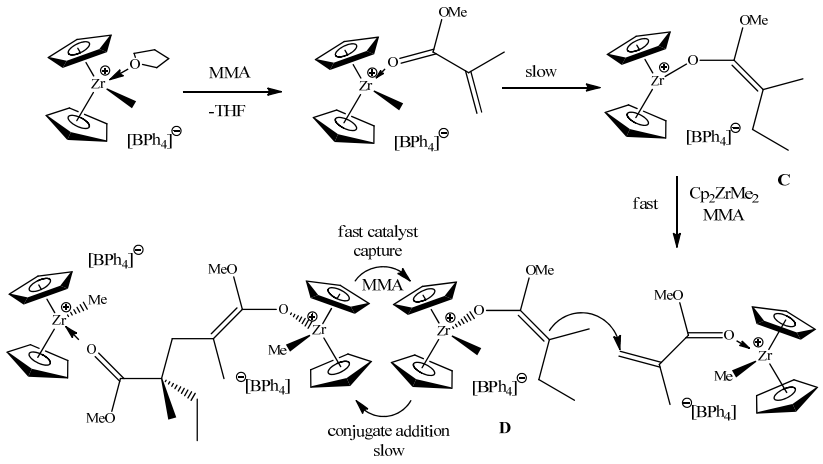


Figure A.4 Slow initiation and subsequent propagation in the bimetallic polymerization of MMA by $[Cp_2ZrMe(THF)]^+[BF_4]^-$ and $[Cp_2ZrMe_2]$.

Many researchers have suggested a bimetallic requirement for polar monomer polymerizations by early metal catalysts.[2, 5-6] Collins reported an early metal system using $[Cp_2ZrMe(THF)]^+[BF_4]^-$ as catalyst and $[Cp_2ZrMe_2]$ as initiator that is capable of polymerizing methyl methacrylate (MMA) to generate a syndio-rich high molecular weight polymer.[2] Kinetic studies indicated a zero order dependence on MMA and additional mechanistic work suggests a slow initiation (with respect to propagation) at low temperature. The rate limiting step involves the reaction of cationic complex with MMA to generate enolate species **C** (Figure A.4). This species then reacts with $[Cp_2ZrMe_2]$ to generate neutral enolate species **D** and a cationic zirconocene methyl complex. Next, a slow Michael addition followed by fast catalyst recapture by methyl methacrylate allows for propagation to occur (Figure A.4). This example highlights cooperative reactivity between two catalyst centers in the polymerization of polar monomers.

In recent years, a variety of bio-inspired multinuclear polymerization catalysts have been developed.[3] Many enzymes utilize two or more metal centers held in close proximity by the

proteins' ligand environment, catalyzing difficult chemical transformations at very high turnover numbers and frequencies. Cooperative multimetallic substrate activation and conversion has been established in a number of metalloenzyme-catalyzed[7] processes and many synthetic models of active metalloenzymes have been studied.[8-9] If two metal centers are required for the polymerization of polar monomers, a bridged binuclear catalyst eliminates the diffusive step.

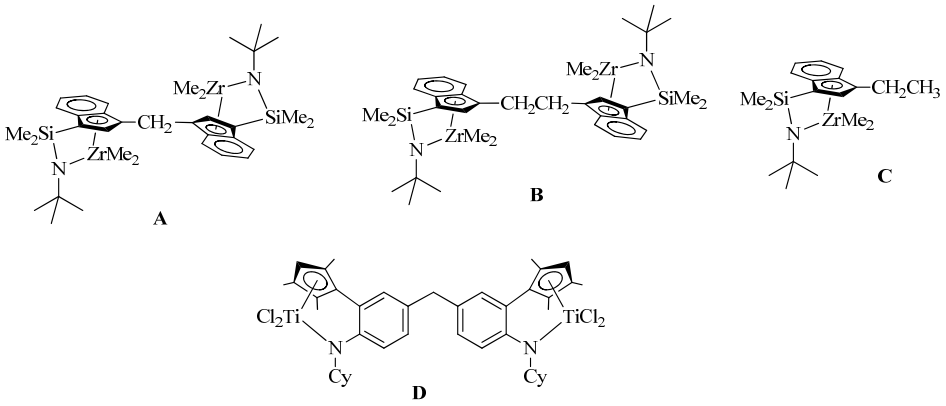


Figure A.5 Structures of selected binuclear and mononuclear polymerization catalysts.

Multinucleating ligands have been used to orient metal centers close to one another. Typically, ligand moieties that have been shown to support olefin polymerization catalysts are connected via a linker. A variety of linkers, from flexible alkyl chains, to unsaturated olefins, to rigid ring systems, have been utilized to support multiple metal centers (Figure A.5). Many of these bimetallic systems generate unique polymers with respect to the related monometallic catalysts. Under identical ethylene polymerization conditions, zirconium catalysts **A** and **B** show ~70x and ~130x increases, respectively, in product polymer molecular weight versus the monometallic analogue **C** when activated with MAO. In addition, when activated with the bis-borate activator

**$B_2$** (Figure A.6), both complexes **A** and **B** produce polyethylene with substantial ethyl branching as characteristic microstructure features. *Ab initio* calculations done on activated **A** and 1-octene suggest that the close proximity of the two zirconium sites in these bimetallic catalysts promotes an approximately 3 kcal/mol more favorable agostic interaction versus that with no agnostic interaction. The resulting increases in propagation/termination rate ratios lead to increased polymer molecular weight.[5]

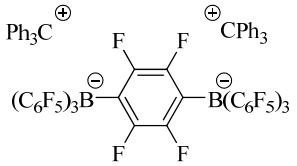


Bis-Borate
**$B_2$**

Figure A.6 Bis-Borate activator $B_2$.

When a doubly bridged ligand (**E)** instead of a single bridged ligand **(F)** was used to connect two metals centers (Figure A.7), higher activity was observed in the polymerization of styrene. In addition, a polymer with higher tacticity and molecular weight was generated. It was proposed that the second bridge prevents rotation around the polymethylene bridge and allows for stereospecific monomer enchainment.[6]

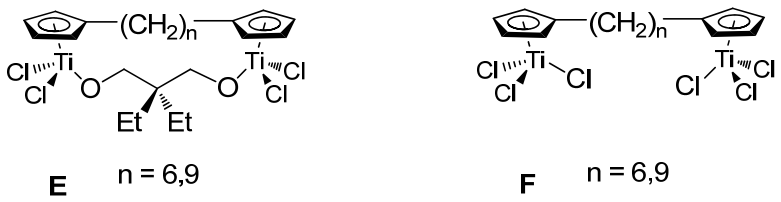


Figure A.7 Dinuclear polymerization catalysts derived from both singly and doubly linked ligands.

Previous work from the Agapie group[10] provides evidence for an interesting bimetallic effect in nickel complexes during the polymerization of ethylene in the presence of various amines. A ligand framework was designed based on a terphenyl backbone with restricted rotation around the aryl-aryl bonds in order to allow for the study of the effect of the metal-metal distance and orientation on generated polymer microstructure. It was shown that there is negligible conversion between the syn and anti atropisomers at the temperature of the polymerizations.[11] This allowed for the isolation of both the syn and anti atropisomers (Figure A.8). The inhibiting effect of polar additives is up to 250 times lower for the syn isomer than the anti-isomer. Unfortunately, the complexes did not incorporate polar monomers and did not show an increase in polymerization over their monometallic counterparts.

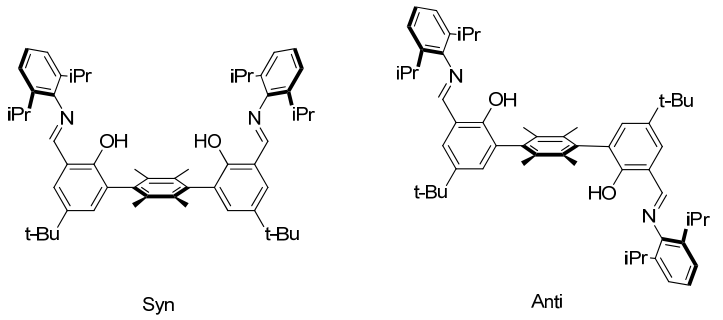


Figure A.8 The syn and anti atropisomers of a binucleating terphenyl diimine ligand.

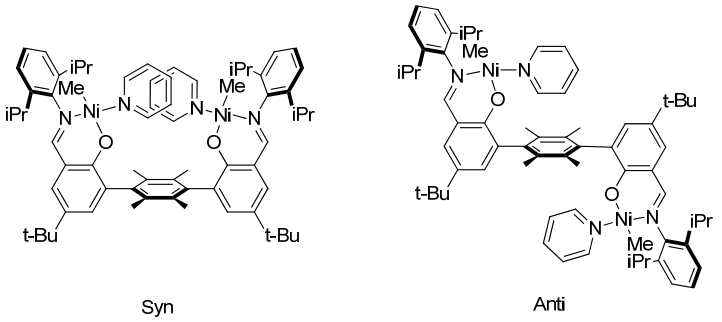


Figure A.9. The syn and anti atropisomers of a diimine dinickel complex.

*Strategy*

Several bimetallic complexes were targeted to explore the bimetallic effects during polymerization with an early metal catalyst (Figure A.10). Substitutions in both the *para* and *meta* positions on the central arene should afford complexes with different metal/metal distances. This may have a significant effect on polymerization reactivity.[10] Targeted are both titanium and zirconium complexes of each ligand. The shown ligand environment was chosen because of recent publications that showed a very high polymerization reactivity of the monotitanium

species **4** (Figure A.11) for the copolymerization of ethylene and 1-hexene[12-17] along with a straightforward synthetic path.

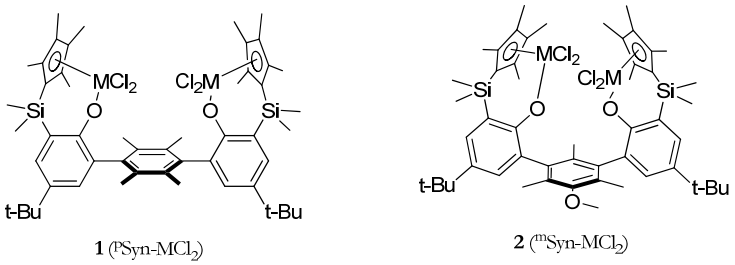


Figure A.10. Two envisioned polymerization precatalysts (M = Ti, Zr).

The final step in the synthesis of a mono-titanium catalyst precursor analogous to **1** and **2** is shown in Figure A.11. Two phenol-protecting groups are reported in the primary literature in the formation of the desired mono-$TiCl_2$ catalyst precursor **4**. Metalating the methoxy-protected phenol (R = Me) with $TiCl_4$ requires high temperature and results in a very low yield (2%) of the desired complex.[13] Using an allyl protecting group resulted in much higher yields (50%) under milder conditions.[12] In order to reduce the number of protection and deprotection steps required if an allyl protecting group were used, it was hypothesized that metalations could be completed with methoxy-methyl ether (MOM) protecting group. It was posited that $TiCl_4$ would also cleave the MOM group and allow for the formation of the desired complex.

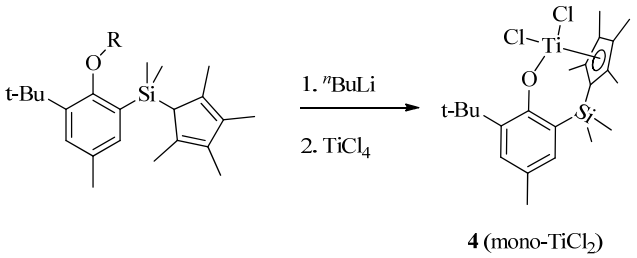


Figure A.11. Reported formation of catalysts precursor 4. (R = Me, $CH_2CH{=}CH_2$)

*Synthesis of a Mononucleating half-sandwich complex*

A model ligand was synthesized to test the hypothesis (Figure A.12). Methoxy methyl ether protection of commercially available 2,4-di-tert-butylphenol with MOMCl followed by directed o-lithiation and subsequent quenching with dichlorodimethylsilane gives complex **3c** in good yield. The $^{1}$H NMR spectrum clearly shows the introduction of an upfield singlet at 0.77 ppm consistent with the generation of a single species containing silicon-Me functional groups. Species **3c** was subjected to a previously generated lithium tetramethylcyclopentadienyl reagent (**LiCp$^{4Me}$**) in tetrahydrofuran. Deprotonation of the tethered Cp$^{4Me}$ functionality is required before metalation with $TiCl_4(THF)_2$. Species **3b** was stirred in diethyl ether in the presence of $^{n}$BuLi. Over time a white precipitate is formed. This material was triturated with pentane to give a brilliant white powder. It is useful in the assignment of species **3a** to notice that the *ipso*-$^{1}$H on the tetramethylcyclopentadienyl group is no longer present in the NMR spectrum.

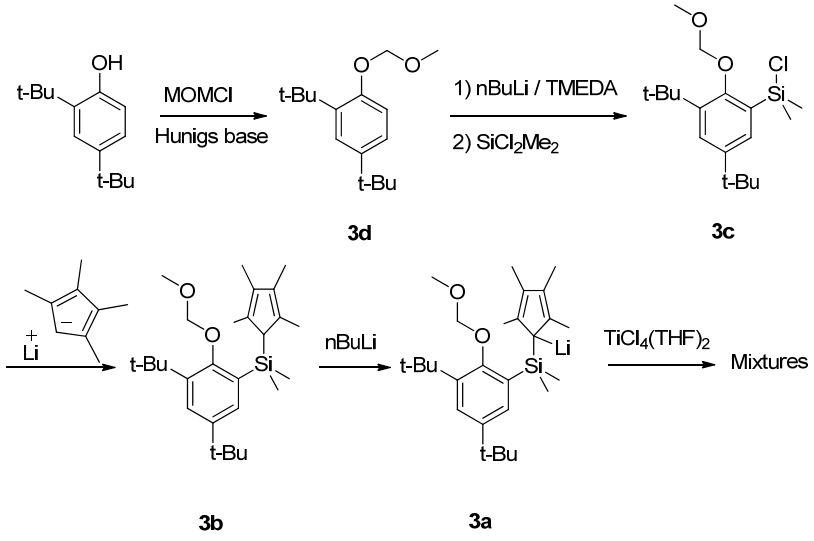


Figure A.12. An explored synthetic route to catalyst precursor 3 using a MOM protecting group.

Metallations were attempted by stirring **3a** with both $TiCl_4$ and $TiCl_4(THF)_2$ at ambient and low temperatures. These reactions failed to cleanly generate the desired complex **3,** instead giving a mixture of products. In all cases, the disappearance of the upfield silicon-methyl singlet and the two singlets from the tetramethylcyclopentadienyl group were absent in the $^1H$ NMR spectra, suggesting that the silicon aryl bond was cleaved under these metalation conditions.

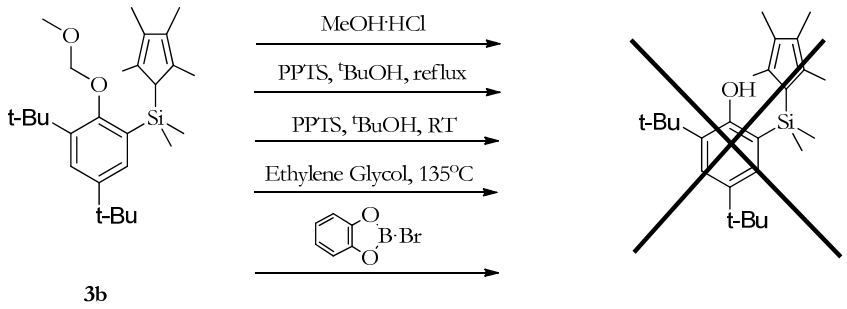


**3b**

Figure A.13. Various conditions used to attempt the removal of the MOM protecting group.

Alternatively, because of the observed instability of the silicon bridge to the metalation conditions we attempted direct deprotection of the MOM group of **3b** before metalation. Compound **3b** was subjected to the reaction conditions shown in Figure A.13, which all resulted in the cleavage of either the silicon-$Cp^{4Me}$ bond or the Si-aryl bond. It was concluded that a MOM-protecting group would not be useful as a protecting group after the installation of the silicon functionality.

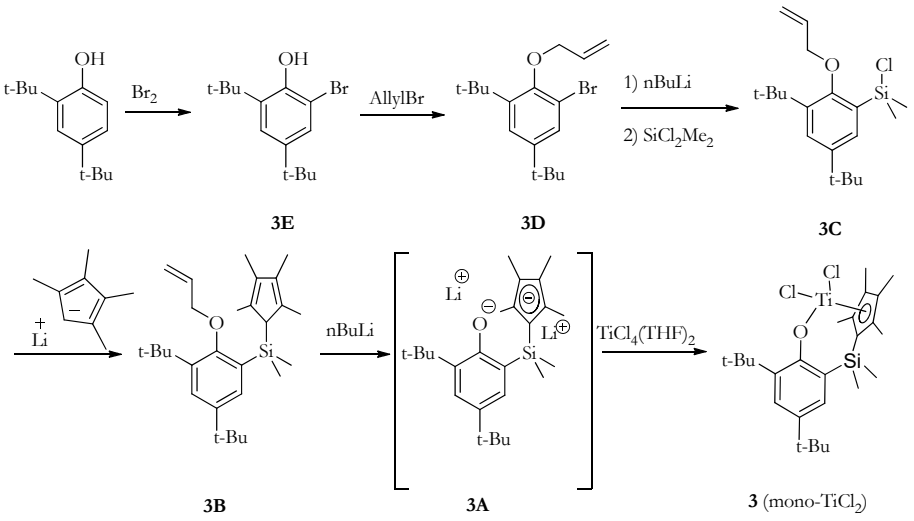


Figure A.14. The synthetic route to catalyst precursor 3 using an allyl-protecting group.

The synthesis of catalyst precursor **3** was accomplished using a synthetic route (Figure A.14) reminiscent of a route reported by Hanaoka *et al.*[12, 14] Ortho-bromination and allyl protection affords compound **3D**. The silylated compound **3C** was synthesized by a lithium-halogen exchange followed by quenching with dichlorodimethylsilane. The fully protonated ligand **3B** was stirred with $^{n}$BuLi in diethyl ether. The deprotected, deprotonated material, **3A**, was carried forward without further purification. This material was taken up in toluene and added slowly to a yellow suspension of $TiCl_4(THF)_2$ in toluene. An immediate color change to dark red-orange was observed. This material was heated in a Schlenk tube for 12 hours at 90°C gradually becoming a yellow-red color. Workup and recrystallization from a cold mixture of pentane/toluene affords yellow needle-like crystals and provided much cleaner material (Figure A.15).

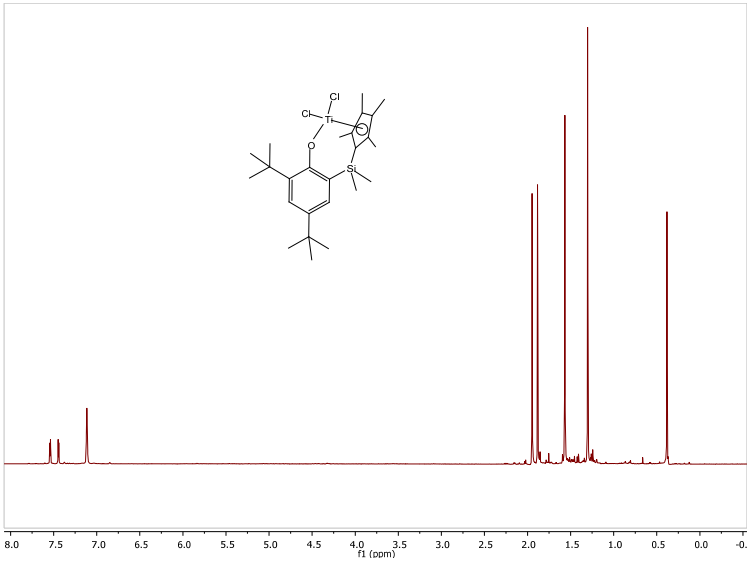


Figure A.15. A $^{1}H$ NMR spectrum of catalyst precursor 3 taken in $C_6D_6$.

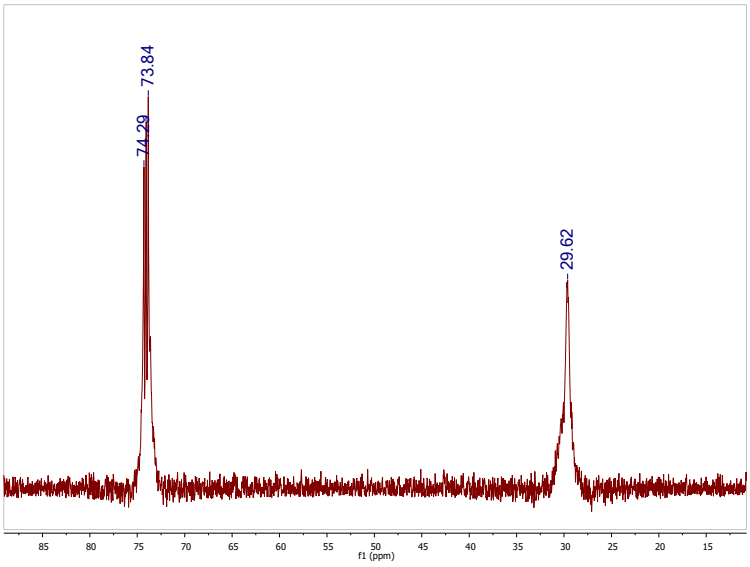


Figure A.16. 13C NMR spectrum of the polymer generated by compound 3 after activation by TIBA/TB under 100 psig of ethylene pressure. The residual solvent (1,1,2,2-tetrachloroethane) signal is visible centered at 74.04 ppm.

The ethylene polymerization activity of catalyst precursor **3** also was studied. Complex **3** was activated with a large excess of triisobutylaluminum (TIBA) and triphenylcarbenium

tetrakis-pentafluorophenyl borate ($Ph_3C^+B^-(C_6F_5)_4$) (abbreviated TB), under 100 psig of ethylene in 10 mL of toluene. Stirring in the reaction vessel stopped after running for approximately 20 seconds likely because a gel-like material had formed in the vessel arresting the motion of the stirbar. The polymerization was stopped at this point by venting the ethylene gas and pouring the reaction mixture into acidified methanol. A white solid was collected on a fine porosity frit and dried under vacuum for 12 hours at ambient temperature to give 279 mg of material. This yield corresponds approximately to which corresponded to a turnover frequency of 29 $kg{\cdot}mmol^{-1}{\cdot}hr^{-1}$. When several milligrams of the material was suspended in deuterated 1,1,2,2-tetrachloroethane and heated to 130°C, the mixture homogenized allowing for $^{13}$C-NMR characterization (Figure A.16). The spectrum shows only one relatively broad carbon resonance at 29.62 ppm, consistent with generation of high molecular weight polyethylene with essentially no branching. This is promising because it's consistent with what is expected for literature compound **4**.

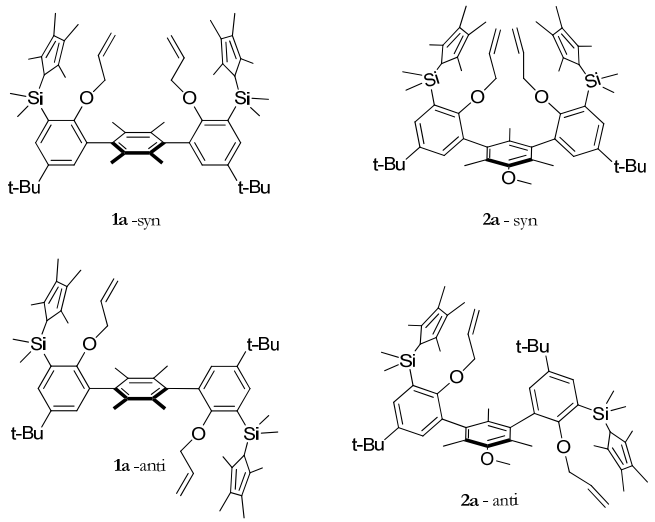


Figure A.17. The *syn* and *anti* atropisomers of terphenyl binucleating ligands with meta and para substitution on the central aryl ring.

*Synthesis of binucleating ligands*

Four binucleating ligands containing a rigid terphenyl backbone were also synthesized (figure 18). *Para* and *meta* substitution on the central aryl ring should allow access to metal complexes with varying metal-metal distances. Starting from previously prepared material,[10-11] a Negishi coupling affords a mixture of both the *syn* and *anti* atropisomers for the para and meta substituted analogues (figure 19). For the meta-terphenyl **2f**, a MOM-protecting group was used because an orthogonal protecting group to the methyl ether on the central arene is required. For the para-terphenyl **1f** a methyl-protected phenol was used because coupling times are much shorter than those for a MOM protecting group. The atropisomers are separated by column chromatography as compounds **1e** and **2e**. It was possible to confirm the assignments of each isomer for the *para* system by comparing them to isolated products prepared in our laboratory.[11] For the *meta* terphenyl, the hypothesis is currently that the Negishi coupling generates more of the anti-isomer than the syn isomer.

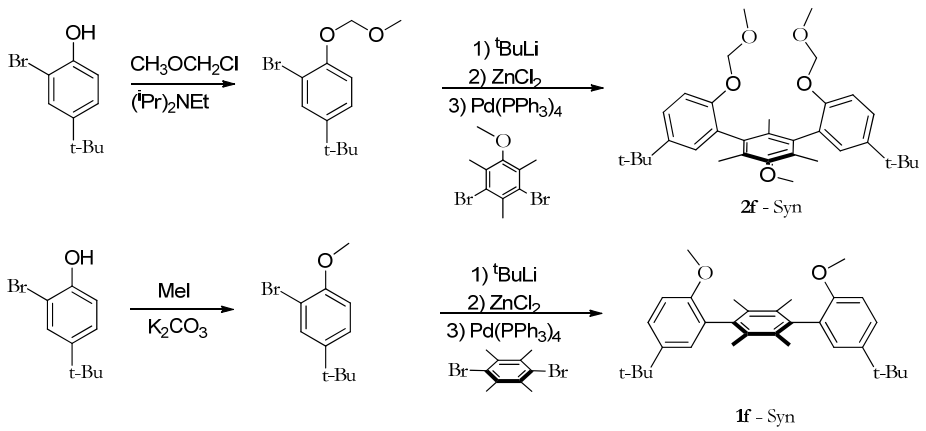


Figure A.18. The synthesis of 1f and 2f by way of a Negishi coupling. In addition to the syn- atropisomer that is shown, the anti-atropisomer is also generated for the meta and para terphenyls.

The *para*-syn complex **1-syn** was prepared (Figure 20). Deprotection of **1f** with excess boron tribromide cleanly affords the free phenol **1e**. Next, selective ortho-bromination of **1e** with two equivalents of bromine at -78°C followed by allyl protection gives **1c**. A lithium halogen exchange followed by quenching with dichlorodimethylsilane yields **1b**. Reaction with lithium tetramethylcyclopentadienyl yielded the desired ligand **1a** in good yield. The anti atropisomer was also prepared using the same procedure.

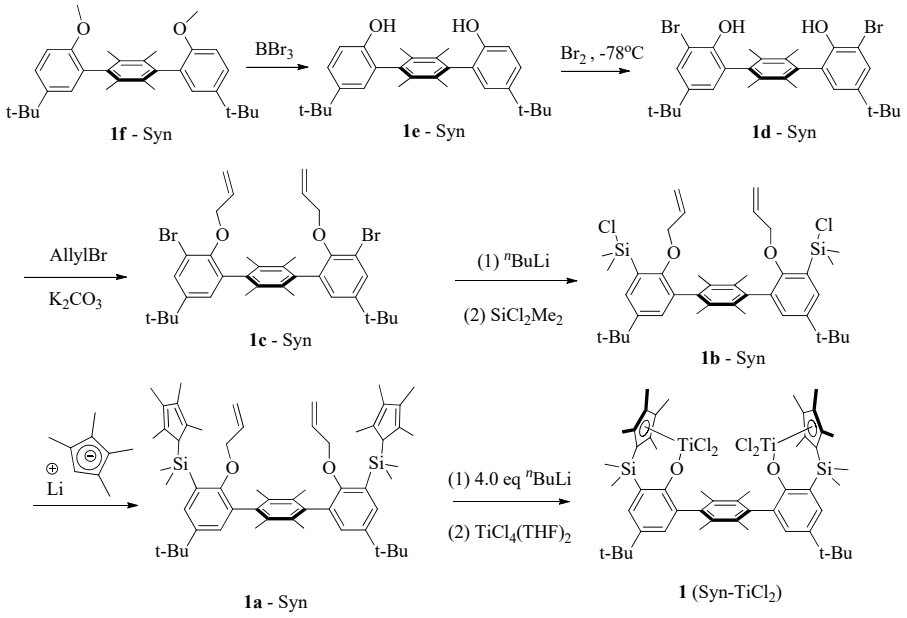


Figure A.19. Synthetic route to catalyst precursor 1 for the syn atropisomer with the para terphenyl backbone.

*Metalation of 1a-syn and 1a-anti*

Metalation proceeds as described above. **1a** is stirred with 4.0 equivalents of $^{n}$BuLi in diethyl ether. This material is then taken up in a mixture of 3:1 toluene:THF and added to a solution of $TiCl_4(THF)_2$ in toluene at -35 °C. The color changes immediately to a red-orange. Upon heating to 95 °C for one hour, the color of the mixture lightens to yellow-orange. Crystals of the product of the reaction were obtained by vapor diffusion of pentane out of a single drop

of hexamethyldisiloxane (HMDSO). The $^1$H NMR of the crystals no longer shows the spectroscopic features expected for the allyl protecting groups. In addition, the chemical shifts for the two singlets corresponding to the tetramethylcyclopentadienyl functional group (1.98 and 1.95 ppm) in the $^1$H NMR spectrum are found in the expected region for metalated half-sandwich complexes. There are only seven peaks in the $^1$H NMR suggesting that both ligand pockets were metalated giving a symmetric complex. The anti-ligand **1a-anti** could be similarly metalated using the same procedure. The *anti*-complex **1a-anti** was purified by precipitation from cold pentane. The $^1$H NMR spectrum of this species is similar to that for **1a-syn** showing only seven distinct resonances indicated the formation of a symmetric complex. The chemical shifts of the seven resonances differed slightly from those of **1a-syn** as expected.

*Polymerization reactivity of 1-syn and 1-anti*

Polymerizations were attempted with **1a-syn** activated with 400 equivalents of triisobutylaluminum and three equivalents of $Ph_3C^+B^-(C_6F_5)_4$ (per Ti) in toluene under 100 psi of ethylene. The polymer generated had a relatively broad $^{13}$C NMR signal at 29.54 ppm again consistent with high-molecular weight polyethylene with negligible branching. Another polymerization was run under those same conditions but with the addition of 5000 equivalents of 1-hexene. Upon workup the polymer generated in these conditions also shows only a single $^{13}$C resonance at 29.5 ppm consistent with an unbranched high molecular weight polyethylene. An attempted homopolymerization of 1-hexene in toluene yields no oligomers or polymer. Together these data suggest that **1-syn** does copolymerize 1-hexene and ethylene under the conditions tested. This reactivity is significantly different than that for mono-titanium complexes **3** and **4,** which generate a copolymer of 1-hexene and ethylene with incorporation of greater

than 20% 1-hexene.[12] It is possible that the steric environment in the ligand pocket of **1** disfavor the insertion of 1-hexene into the polymer chain.

*Attempted metalations of 2a-syn and 2a-anti*

Ligands **2a-syn** and **2a-anti** were successfully synthesized. A Negishi coupling afforded both atropisomers of the MOM protected terphenyl **2f**. The phenol was readily deprotected using a mixture of aqueous hydrochloric acid and methanol. The atropisomers were separated using silica gel column chromatography. The atropisomers were assigned using the assumption that the Negishi coupling generates a larger amount of the *anti* atropisomer than the *syn* isomer. The full ligands **2a-syn** and **2a-anti** are obtained from **2f-syn** and **2f-anti** using the same synthetic procedure shown in figure 20. Metalations were attempted with both atropisomers of ligand **2a** under the conditions used to metalate **1a**. The $^{1}$H NMR spectra for the resulting material has a veritable forest of peaks consistent with metalation conditions that do not generate a single desired species. A mixture of many different species is likely generated. One possible explanation for this observation is that strong lewis acids such as $BBr_3$ are often used to deprotect methoxy-protected phenols; it is possible that the $TiCl_4(THF)_2$ used to metalate **2** instead could also remove the methoxy group, forming some undesired titanium complexes.

*Conclusions and future directions*

Bimetallic polymerization catalysts **1-syn and 1-anti** were successfully synthesized. Preliminary polymerization reactivity was studied for the syn atropisomer and it was found to differ from the monometallic version found in the primary literature in that it does not incorporate 1-hexene

to generate a copolymer in one set of conditions. Further study is required for these systems.

Polymerization reactivity for **1-anti** will be studied as a control for the syn complex. This will serve as a better control for the hypothesis that the steric environment in the syn complex prevents the incorporation of 1-hexene.

In addition to polymerizations that occur by a coordination-insertion mechanism, activity for other polymerizations will be explored. The coordination-addition polymerization of methyl methacrylate will be studied for titanium and zirconium complexes (*vide supra*). It has been recently shown that a number of group four metal complexes are active for the ring opening polymerization of lactides.[18-19] This reactivity will be explored in titanium and zirconium complexes formed using the ligands reported here.

It would be beneficial to study the mode of activation in these complexes. No data has been collected yet to suggest whether one or two of the titanium centers on a single molecule are activated during polymerization. Generating the dialkyl complexes (Figure A.20) followed by stoichiometric activation may provide insight into this question. Polymerization experiments will be conducted using both ½ of an equivalent and 1 equivalent of activator per binuclear complex. Measuring the activity will suggest whether both or only one of the titanium centers are activated. If it is determined that only one of the titanium centers is activated, other activators will be tested.

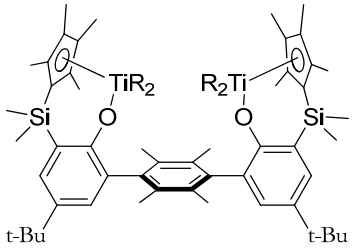


**1** (Syn-$TiR_2$)

Figure A.20. Titanium alkyl complex for stoichiometric initiation experiments

To explore the bimetallic effect during polymerization using sterically encumbered binucleating ligands on early metals (Ti, Zr) which are typically more active and more easily poisoned, complex **3-s** (Figure A.21) was synthesized from previously prepared terphenyl ligand **2-s-allyl**. The ligand environment around titanium was chosen because of reports in the literature by several research groups of the proficiency of phenoxy-cp complexes of titanium for the copolymerization of ethylene and 1-hexene.[2-7] Metalation of **2-s-allyl** was accomplished by first a one-step deprotection/deprotonation using $^{n}$BuLi followed by reaction with $TiCl_4(THF)_2$ and subsequent heating in a mixture of toluene and THF.

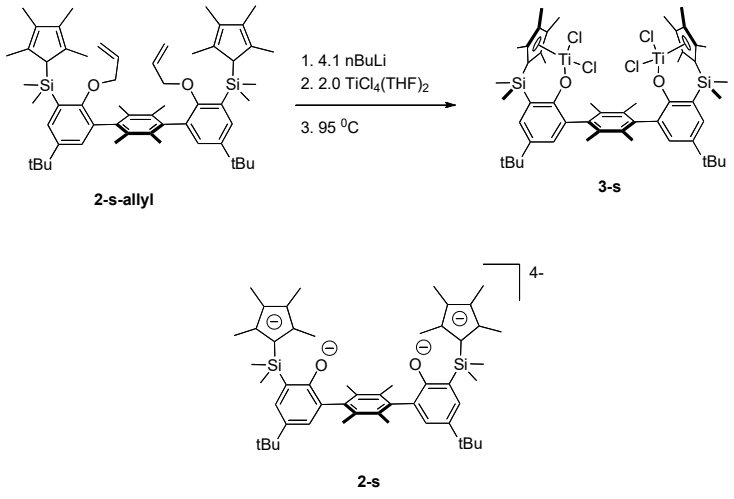


**2-s-allyl** **3-s** **2-s**

Figure A.21: Synthesis of 3-s from ligand precursor 2-s-allyl. Also shown is tetra-anionic deprotected and deprotonated ligand 2-s.

The desired complex was found to be quite soluble in even highly nonpolar solvents such as pentane and hexamethyldisiloxane (HMDSO). Isolation of the desired product from the crude mixture was accomplished by vapor diffusion of pentane out of a solution of the crude material in pentane/HMDSO to give yellow crystals in low yield (5.6%). The $^{1}$H NMR data of the collected crystals supports the assignment of **3-s** as a bimetallic titanium complex, which in solution at ambient temperature would be expected to have $C_{2v}$ symmetry equilibrating all four Ar-$CH_3$ groups in the central arene. Several crops of crystals collected from the crude reaction mixtures of the metalation reaction failed to diffract x-rays with the exception being a material **4-s**. This material, as seen in Figure A.22, is a bimetallic complex of titanium with an oxo ligand bridging the two titanium ions. One terminal chloride ligand is present for each of the titanium ions.

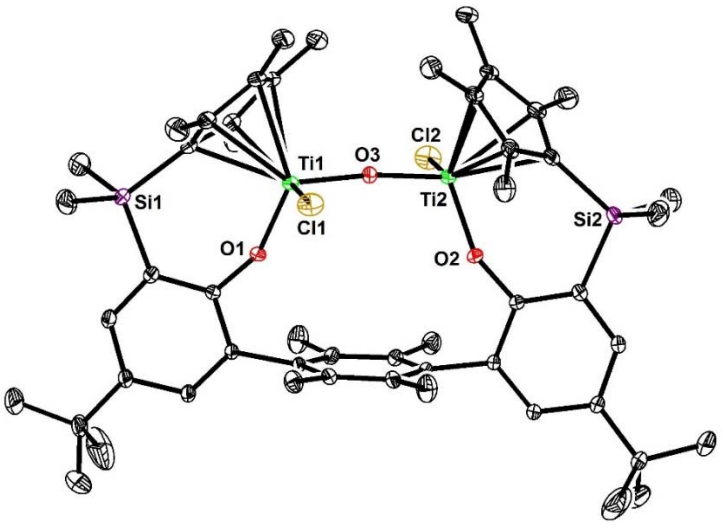


Figure A.22. A solid-state structure of di-titanium complex 4-s with a bridging oxo.

The material providing the structure of **4-s** was likely formed during metalation by reaction with trace amounts of water evolving two equivalents of HCl. **4-s** is not the bulk material because the $^1$H NMR of the crystals is not consistent with the symmetry present in **4-s**. While **3-s** is expected to possess a mirror plane of symmetry, which passes through both distal arenas and both titanium ions, **4-s** lacks this mirror plane of symmetry, having only $C_2$ symmetry. This would cause the $^1$H NMR spectrum to possess significantly more resonances. In particular, one would expect different resonances for each of the two Si-$CH_3$ groups, which isn't observed. Perhaps this contaminant **4-s** co-crystallizes with **3-s** and is present in very small amounts. **4-s** is likely more crystalline, explaining how while several crystals of **3-s** were mounted, they failed to diffract and instead when a crystal of **4-s** was selected, it diffracted to give a useable data set. The solid-state structure of **4-s** provided evidence that binucleating ligand **2-s** could support two $Ti^{IV}$ ions. Attempts to obtain a solid-state structure of **3-s** are ongoing.

Similar to the monometallic phenoxy-tetramethylcyclopentadienyl complexes in the literature (ref), bimetallic complex **3-s** is a highly active polymerization catalyst upon activation (figure 4). Upon activation of **3-s** with 400 equivalents of $Al^iBu_3$ and 6 equivalents of $[Ph_3C]^+[B(C_6F_5)_4]^-$, the active species is capable of polymerizing ethylene with an activity up to 1.95 $kg \cdot mmol^{-1} \cdot hr^{-1}$, approximately an order of magnitude lower than that of a monometallic phenoxy-tetramethylcyclopentadienyl complex of titanium which under similar activation conditions, polymerizes ethylene with an activity of up to 42.9 $kg \cdot mmol^{-1} \cdot hr^{-1}$. **3-s** is also a potent catalyst for the generation of copolymers of ethylene and 1-hexene. Under identical activation conditions but with the addition of various equivalents of 1-hexene, a polymer material is generated which has different solubility properties from the polymer generated in the absence

of 1-hexene additives. The polymer can be characterized by $^{1}H$ and $^{13}C$ NMR spectroscopy, and by using the processing method of De Pooter et al.[8] it was determined that in the presence of 80 000 equivalents of 1-hexene, a copolymer that is 15 mol % 1-hexene is generated. This % incorporation is slightly lower than 23.7 mol % incorporation found for the monometallic titanium complex **5**. A large excess of $Al^{i}Bu_3$ as an alkylating agent is not necessary in order to successfully activate **3-s** as it was activated with 50 equivalents of $Al^{i}Bu_3$ Activation of **3-s** with methylaluminoxane (MAO) was not as effective as with the route involving the reagent pair $Al^{i}Bu_3$/TB. The activity in ethylene polymerization in the absence of an inhibiting additive such as 1-hexene is an order of magnitude or greater worse than with $Al^{i}Bu_3$/TB.

| Catalyst[a] | Activator | Activator / eq. | Additive | Add. / equiv. | Time / min | Polymer / g | Activity / kg/(mmol·hr) |
|---|---|---|---|---|---|---|---|
| **3-s** | $Al^{i}Bu_3$ / TB[b] | 800 / 6 | 1-hexene | 4800 | 20 | 0.084 | 2.52 |
| **3-s** | $Al^{i}Bu_3$ / TB | 800 / 6 | 1-hexene | 8000 | 120 | 0.39 | 1.95 |
| **3-s** | $Al^{i}Bu_3$ / TB | 800 / 6 | 1-hexene | 80000 | 120 | 0.029 | 0.145 |
| **3-s** | MAO[c] | 100 | - | - | 60 | 0.000 | 0 |
| **3-s** | MAO | 1000 | - | - | 60 | 0.006 | 0.06 |
| **3-s** | MAO | 2000 | - | - | 20 | 0.006 | 0.18 |
| **3-s** | $Al^{i}Bu_3$ / TB | 800 / 6 | - | - | 20 | 0.052 | 1.56 |
| **3-s** | $Al^{i}Bu_3$ / TB | 800 / 6 | - | - | 20 | 0.098 | 2.94 |
| **3-s** | $Al^{i}Bu_3$ / AB[d] | 800 / 6 | - | - | 20 | 0.054 | 1.62 |
| **3-s** | $Al^{i}Bu_3$ / AB | 800 / 6 | $Pr_3N$ | 2000 | 60 | 0.000 | 0 |
| **3-s** | $Al^{i}Bu_3$ / TB | 800 / 6 | $Et_2O$ | 3200 | 20 | 0 | 0 |

Table 2. Polymerization data for 3-s. [a]0.1 μmol in toluene with a total volume of 10 mL and 100 psig of ethylene. [b]TB = $[Ph_3C]^+[B(C_6F_5)_4]^-$. [c]One equivalent of MAO was considered to be a single $OAlCH_3$ fragment. [d]AB = $[H(NMe_2(C_6H_5)]^+[B(C_6F_5)]^-$.

Because of the sensitivity to early metal polymerization catalysts to Lewis basic molecules, **3-s** is readily poisoned by even weakly Lewis basic materials such as diethyl ether. Addition of 1600 equivalents of diethyl ether per titanium to the polymerization apparatus using the same activation procedure as for the polymerization of ethylene without any other additives results in the generation of no polymer. It is unclear whether the active cationic titanium species

is poisoned by the ether or whether activation of **3-s** fails to occur because of a reaction between diethyl ether and $Al^{i}Bu_3$ or $[Ph_3C]^+[B(C_6F_5)_4]^-$. Ethylene polymerization does not occur for the monometallic titanium complex **5** in the presence of 1600 equivalents of diethyl ether. Experiments to explore the effect of bulkier ethers such as diisopropyl ether or methyltertbutyl ether on polymerization activity are currently a work in progress.

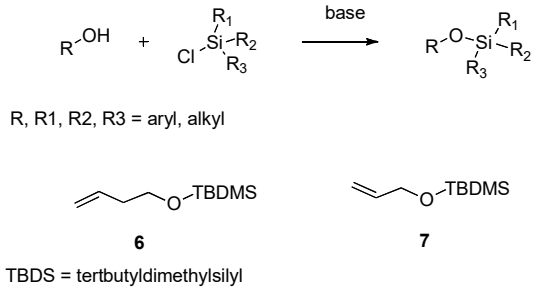


Figure A.23: The synthesis of bulky silyl ethers as potential monomers. The synthesis of 6 and 7 have been completed and their ability reactivity has been explored with 3-s and 5.

Silyl-protection of alcohols may allow access to monomers exhibiting properties that would allow incorporation of the monomer into a polymer with ethylene using the bimetallic catalyst **3-s** but not with a monometallic version such as **5** because of the ease of varying the steric bulk on the silyl ether. Using the general procedure shown in figure 5, two such monomers were prepared. One of them, **6**, possesses a terminal olefin two carbons distal from the silyl ether. The second, **7**, is also a terminal olefin with instead one carbon atom separating the olefin and the silyl ether. Some polymerizations of ethylene in the presence of varying equivalents of **6** and **7** were attempted. The polymer yield for each of these runs is very low, with some resulting in only small flecks of polymer visible in the reaction vessel after quenching the reaction mixture with acidified methanol, indicating that the silyl ether is highly inhibiting in these polymerization

runs. These results suggest a slight difference in reactivity between the mononuclear complex **5** and the binuclear complex **3-s**. With the addition of 1000 equivalents of **6** per titanium center to the polymerization setup with precatalyst **5** results in the generation of no polymer material. No white flecks of polymer were visible in the reaction vessel after quenching the mixture with acidified methanol. However, with the binuclear complex **3-s**, upon quenching the reaction, a small amount of white material was visible floating in the solution. This material was collected by filtration, dried under vacuum, and weighed. Approximately 1 mg of material was collected. These two experiments are not enough data to draw meaningful conclusions from although there was an observable difference in reactivity between **5** and **3-s** in the presence of silyl ether **6** so futher study is required. This same pattern was seen with the addition of 500 equivalents of silyl ether **7** with the monometallic catalyst **5** generating no polymer and with bimetallic catalyst **3-s** generating a small amount of polymer**.**

| entry | Catalyst | Activator | Activator / eq. | Additive | Add. / equiv. | Time / min | Polymer / g | Activity / kg/(mmol·hr) |
|---|---|---|---|---|---|---|---|---|
| 1 | **3-s** | $Al^iBu_3$ / AB | 800 / 6 | 6 | 2000 | 60 | 0.001 | 0.01 |
| 2 | **3-s** | $Al^iBu_3$ / AB | 800 / 6 | 6 | 1000 | 60 | 0.001 | 0.01 |
| 3 | **3-s** | $Al^iBu_3$ / AB | 800 / 6 | 6 | 200 | 120 | 0.003 | 0.015 |
| 4 | **3-s** | $Al^iBu_3$ / AB | 800 / 6 | 7 | 1000 | 60 | 0.001 | 0.01 |
| 5 | **5** | $Al^iBu_3$ / AB | 400 / 3 | 6 | 1000 | 60 | 0.000 | 0 |
| 6 | **5** | $Al^iBu_3$ / AB | 400 / 3 | 6 | 500 | 60 | 0.001 | 0.01 |
| 7 | **5** | $Al^iBu_3$ / AB | 400 / 3 | 6 | 100 | 120 | 0.004 | 0.02 |
| 8 | **5** | $Al^iBu_3$ / AB | 400 / 3 | 7 | 500 | 60 | 0.000 | 0 |

Table 3. Polymerization data for 5 and 3-s in the presence of silyl ethers 6 and 7.

The nature of the active catalytic species during polymerizations is very difficult to elucidate. It is particularly difficult when there exists the presence of a large amount of an aluminum compound in solution, like is the case with activation by MAO or when using $Al^iBu_3$ as the in-situ alkylating agent. It was desired to make discreet titanium alkyl complexes supported

by ligand **2-s** and attempt stoichiometric activation of those species by $[Ph_3C]^+[B(C_6F_5)_4]^-$, $[H(NMe_2(C_6H_5)]^+[B(C_6F_5)]^-$, or $B(C_6F_5)_3$. Alkylations were run on **3-s** to generate the corresponding titanium alkyl complexes (Figure A.24).

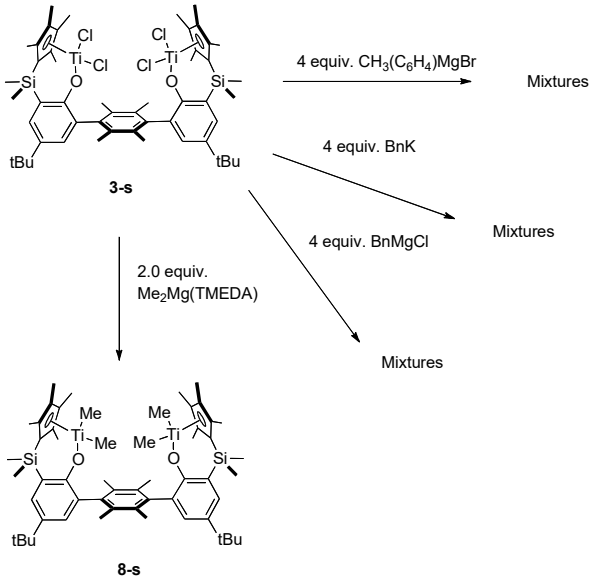


Figure A.24: Alkylations of 3-s with a variety of alkyl nucleophiles. The only reagent to provide a clean alkylated product was $Me_2Mg$(TMEDA).

There was a reaction of **3-s** with four equivalents of benzyl potassium in toluene over approximately one hour but the product was not a single species by $^1$H NMR. Much like the reaction with benzyl potassium, reactions with several different types of Grignard reagents such as paramethylphenylmagnesium bromide and benzylmagnesium chloride did not yield cleanly alkylated species. However, upon addition of two equivalents of $Me_2Mg$(TMEDA) (TMEDA = N,N,N',N'-tetramethylethylenediamine) the product after 1 hour by $^1$H NMR shows a very clean product (figure 8) which we assigned as the dialkyl complexes of titanium **3-s**. The spectrum of starting material **3-s** possesses a single strong resonance of integration of 12 relative to the resonance for the aryl tertbutyl groups (1.27 ppm) at 0.48 ppm, which corresponds to the

protons of the -$SiMe_2$ group. Upon reaction with $Me_2Mg$(TMEDA), an additional resonance of equal integration to the signal for –SiMe protons appears in the region between 0.4 and 0.6 ppm, which is the expected region for a titanium methyl group (-0.1 - 0.9 ppm).[9] The presence of only one resonance suggests that **8-s** is fluxional in $C_6D_6$ at room temperature so as to equilibrate all four of the Ti-Me groups on the NMR timescale thus giving the molecule $C_{2v}$ symmetry. However, although this material could be synthesized, further reactivity studies with it proved unfruitful. **8-s** was not stable over an hour at room temperature in solution as $^1$H NMR spectra taken after one hour in $C_6D_6$ showed significant change to become a multitude of species.

*Synthesis of a binucleating terphenyl phenoxy-indenyl ligand*

Complex **3-s** has an activity over an order of magnitude lower than that of the monometallic complex **5**. This difference in reactivity may be a result of the increased steric bulk at the binding sites of titanium by putting two titanium centers on **2-s**. One potential way to dial back on the steric bulk at titanium is to synthesize a different ligand with a slightly different substitution pattern on the cyclopentadiene group. Treatment of **9-s** with a slight excess of Li($C_9H_7$) in diethyl ether results in the formation of lithium chloride and a new organic compound.

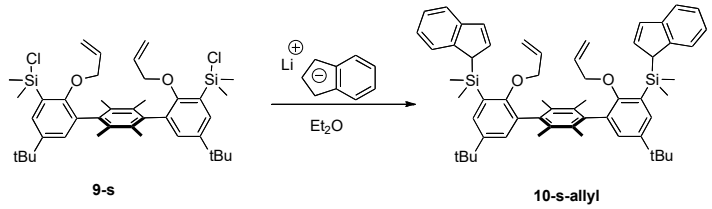


**9-s** **10-s-allyl**

Figure A.25: Synthesis of 10-s-allyl.

The $^1$H NMR of the crude reaction mixture possesses the resonances between 4 and 6 ppm typical of aryl-allyl ether functional groups like those seen the $^1$H NMR spectrum of **2-s-allyl**. The $^1$H NMR shows how the singlet found at 0.9 ppm for **9-s** indicative of the $SiCH_3$ protons splits into two singlets of equal integration. This is consistent with the formation of **10-s-allyl** because of the loss of equivalence between the methyl groups on a single silicon atom. The aromatic region possesses overlapping resonances making it difficult to assign all of the proton resonances in that region. This material was submitted to the reaction conditions used to form **3-s**. **10-s-allyl** was subjected to four equivalents of $^n$BuLi in diethyl ether followed by addition to $TiCl_4(THF)_2$ in a mixture of THF/Toluene. The crude material had a $^1$H NMR in $C_6D_6$ that was very broad and didn't possess any of the sharp signals one would expect to see with the formation of the desired product.

Another strategy for decreasing the steric bulk around the titanium active sites is to change the substitution on the central arene of our terphenyl framework. The idea is illustrated in figure 11. For the 1,4 substituted central arene the coordination sites of titanium, which are shown by boxes, point towards each other more than they do in the meta case. For the 1,3 substituted central arene, two of the coordination sites are pointed more directly at one another but the other two coordination sites point off into space. It is unclear how this change in orientation will affect polymerization behavior. To explore this idea, meta substituted ligand **16** (Figure A.27) was synthesized using a strategy identical to that used for the synthesis of 1,4 substituted ligand **2-s-allyl**. Upon reaction of **16** with four equivalents of $^n$BuLi followed by addition of $TiCl_4(THF)_2$ and subsequent heating, a mixture is formed that has a $^1$H NMR suggestive of the formation of a significant amount of desired dititanium complex **17**. The most

important feature in the spectrum suggesting complex formation is the presence of four sharp singlets of equal integration between 1.9 and 2.1 ppm. This would be consistent with a loss of symmetry in the cyclopentadienyl methyl groups upon complexation of the group to titanium. However, this material was not found to be very crystalline and crystals of **17-s** were not isolable. In addition, the material seems to be unstable in the solid state over a number of days at -35 $^{o}$C as seen by a change in the $^{1}$H NMR spectrum upon sitting for that time.

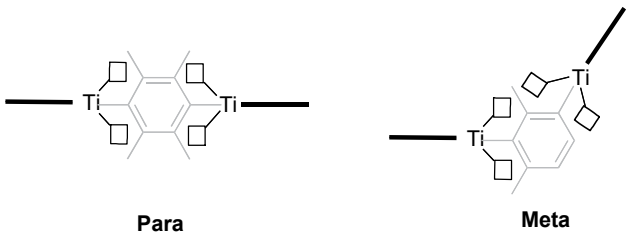


Figure A.26: An illustration of the change in orientation of the binding sites of titanium with both 1,4 and 1,3 substitution on the central arene.

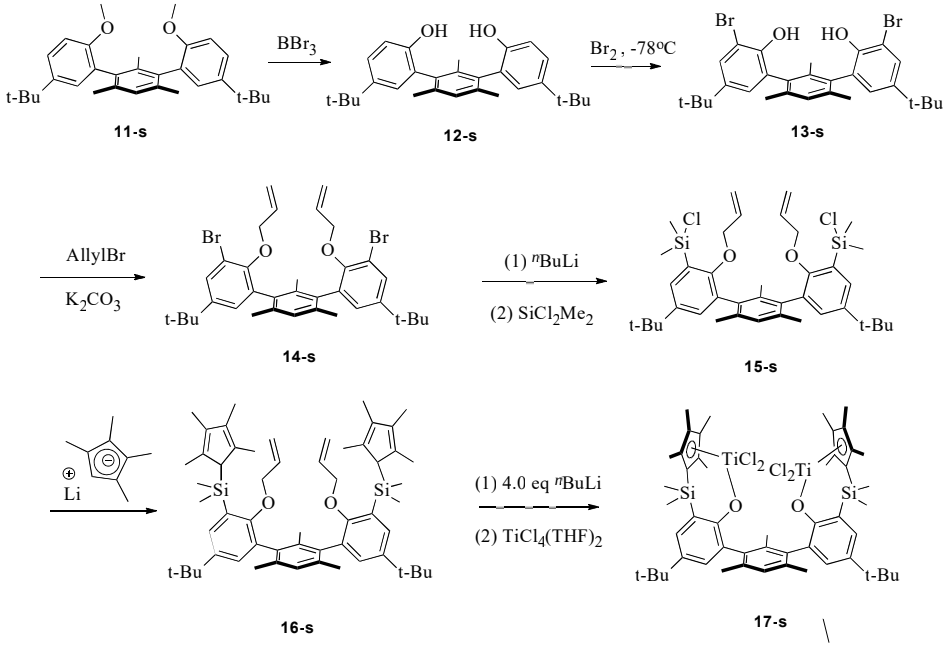


Figure A.27: Synthetic scheme for the formation of 17-s.

*Conclusions and future direction*

The preliminary polymerization results of **3-s** in the presence of silyl ethers suggests that a bimetallic effect may be present with the studied early metal system in a manner analogous to the previously reported system with nickel and bulky amines. The concentration of silyl ethers needs to be lowered because at the current number of equivalents, not enough polymer is being generated so as to allow for characterization of the polymers. Additionally, the high concentration of triisobutylaluminum used as an alkylating agent makes analyzing any inhibition effect difficult because of the possibility that much of the silyl ether in solution simply complexes the triisobutylaluminum, sequestering it away and keeping it from interacting with the active titanium species. The amount of triisobutylaluminum used as an alkylating agent needs to be minimized.

Complex **17-s** needs to be isolated because the comparison between **3-s** and **17-s** could offer information on the importance of orientation of the two metal centers to polymerization behavior. Perhaps, opening up the coordination sites in **17-s** could result in a higher overall activity in ethylene polymerization. Additionally, perhaps changing the steric profile of the titanium centers in **17-s** from **3-s** could drastically change the ease by which inhibiting compounds such as ethers and amines bind titanium and cause **17-s** to be much more readily inhibited by such molecules than **3-s**.

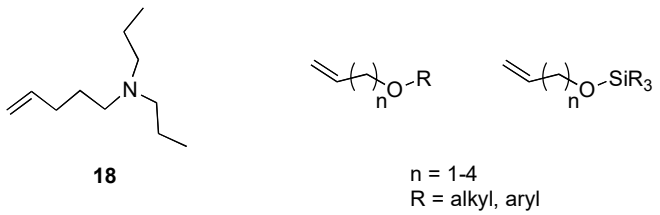


Figure A.28: Potential monomers to be incorporated using the "bimetallic effect."

If it is found that, with either bulky ethers or amines, polymers of ethylene or copolymers of ethylene/1-hexene can be formed in the presence of various Lewis bases, the ability of **3-s** to incorporate monomers with distal polar groups (Figure A.28) will be studied. Very recent results from our group show that for monomers with bulky pendant amines, a version of our terphenyl bis-phenoxy imine complex of nickel can generate a copolymer of ethylene and the bulky amine monomer **18** (Figure A.28).

*Synthesis of bisphenoxycyclopentadienyl compounds (para – figure 14)*

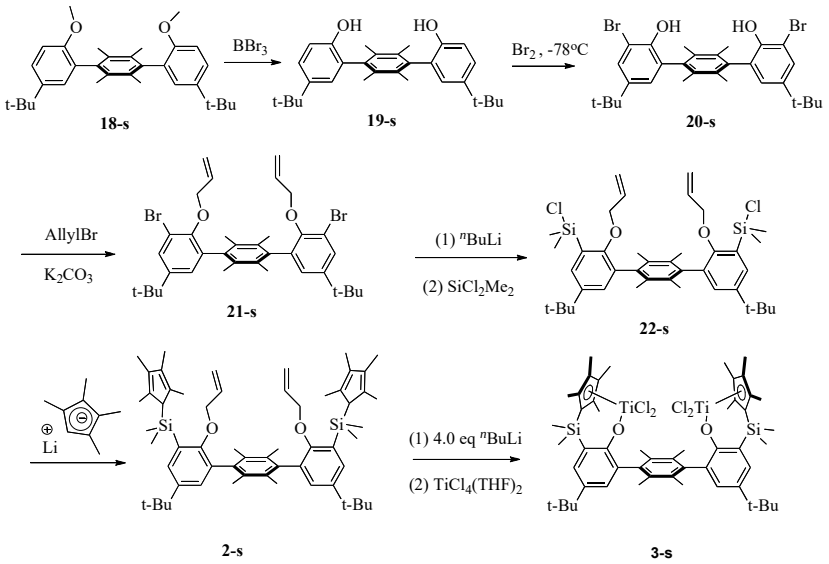


Figure A.29: synthetic scheme for 3-s.

## A.2. Experimental

**18-s** and **18-a**. Synthesis of the biphenyl compounds **18** was accomplished via the Negishi coupling of 1,4-dibromo-2,3,5,6-tetramethybenzene with two equivalents of 2-bromo-4-*tert*-atropisomers of the terphenyl compound were coprecipitated from methanol as a colorless solid (15.4 g, 71% yield). $^{1}$H NMR (300 MHz, $CDCl_3$): δ 7.36 (2dd, 2H, Ar*H*), 7.19 (2d, 2H, Ar*H*), 6.95 (2d, 2H, Ar*H*), 3.78 (2s, 6H, OC$H_3$), 1.99 (2s, 12H, ArC$H_3$), 1.34 (2s, 18H, C(C$H_3$)$_3$) ppm. $^{13}$C NMR (75 MHz, $CDCl_3$): δ 154.70 (Ar), 143.25 (Ar), 137.83 (Ar), 137.57 (Ar), 132.22 (Ar), 132.10 (Ar), 130.75 (Ar), 129.31 (Ar), 128.97 (Ar), 124.29 (Ar), 124.21 (Ar), 110.19 (Ar), 110.09 (Ar), 55.81 (O*C*H$_3$), 55.59 (O*C*H$_3$), 34.29 (Ar*C*(CH$_3$)$_3$), 31.75 (ArC(*C*H$_3$)$_3$), 18.07 (Ar*C*H$_3$), 18.00 (Ar*C*H$_3$) ppm. HRMS (EI+) Calcd. for $C_{32}H_{42}O_2$: 458.3185. Found: 458.3184.

**19-a** and **19-s**. A mixture of **18-a** and **18-s** (10.897g, 23.76 mmol, 1 equiv.) was dissolved in 100 mL of dichloromethane and cooled to 0 °C. Neat boron tribromide (9 mL, 95.03 mmol, 4 equiv.) was added to the solution. The reaction mixture was allowed to warm to ambient temperature and stirred for one hour. The mixture was quenched with saturated sodium bicarbonate solution. The organic fraction was collected, contacted with $MgSO_4$, filtered through celite, and concentrated *in vacuo*. The syn and anti isomers were isolated by column chromatography. 4:1 DCM:hexanes. **19-anti** (6.5 g) $^{1}$H-NMR (300 MHz, $CDCl_3$): δ ppm 7.31 (dd, 2H, J = 8.4, 2.4 Hz, Ar-**H**) 7.05 (d, 2H, J = 2.4 Hz, ArH) 6.94 (d, 2H, J = 8.5 Hz, ArH) 4.52(s, 2H, ArOH) 1.99 (s, 12H, Ar-$CH_3$) 1.32 (s, 18H, C($CH_3$)$_3$) **19-syn** (1.73 g) $^{1}$H-NMR (300 MHz, $CDCl_3$): δ ppm 7.50 (d, 2H, J = 2.3 Hz, ArH) 7.02 (d, 2H, J = 2.3 Hz, ArH) 5.26 (br, 2H, ArOH) 1.98 (s, 12H, Ar$CH_3$) 1.30 (s, 18H, C($CH_3$)$_3$)

**20-s**. 3,3"-dibromo-5,5"-di-*tert*-butyl-2',3',5',6'-tetramethyl-[1,1':4',1"-terphenyl]-2,2"-diol **19-s** (1.728 g, 4.01 mmol, 1 equiv.) was dissolved in 100 mL of dichloromethane and cooled to -78 °C. Bromine (403 μL, 7.82 mmol, 1.95 equiv.) was added by syringe. The mixture was stirred at reduced temperature for one hour and then allowed to reach ambient temperature. The mixture was stirred for 8 hours at ambient temperature. A saturated solution of sodium bicarbonate was added. The organic phase was collected, contacted with $MgSO_4$, filtered through celite, and concentrated *in vacuo*. The compound was purified by flash column chromatography 5:1:1/2 hexane:Ethyl Acetate:DCM as a white solid (2.20 g, 94% yield) $^{1}$H-NMR (300 MHz, $CDCl_3$): δ ppm 7.52 (d, 2H, J = 2.3 Hz, ArH) 7.05 (d, 2H, J = 2.3 Hz, ArH) 5.27 (s, 2H, ArOH) 2.00 (s, 12H, Ar$CH_3$) 1.32 (s, 18H, C($CH_3$)$_3$)

**21-s**. 2,2"-bis(allyloxy)-3,3"-dibromo-5,5"-di-*tert*-butyl-2',3',5',6'-tetramethyl-1,1':4',1"-terphenyl. **20-s** (2.450 g, 4.16 mmol, 1 equiv.) was dissolved in 200 mL of acetone. Allyl bromide (3.6 mL, 41.6 mmol, 10 equiv) was added by syringe. This mixture was added using an addition funnel to a stirred solution of sodium hydroxide (1.7 g, 41.6 mmol, 10 equiv.) in 5 mL of water. After addition was complete, the mixture was rapidly stirred for 24 hours at which time volatiles were removed *in vacuo*. The mixture was extracted with dichloromethane, contacted with $MgSO_4$, filtered through celite, and concentrated *in vacuo*. The compound was purified by flash column chromatography 5:1:1/2 hexane:Ethyl Acetate:DCM as a white solid. (2.557 g, 92 % yield) $^{1}$H NMR (300 MHz, $C_6D_6$): δ ppm. 7.72 (d, 2H, J = 2.4 Hz, ArH) 7.10 (d, 2H, J = 2.4 Hz, ArH)

5.80 (ddt, 2H, J = 17.1, 10.5, 5.4 Hz, $OCH_2CH=CH_2$) 5.21(dd, 2H, J = 17.1, 1.7 Hz, $OCH_2CH=CH_2$) 4.96 (dd, 2H, J = 17.1, 1.7 Hz, $OCH_2CH=CH_2$) 4.22 (dt, 4H, J = 5.3, 1.5 Hz, $OCH_2CH=CH_2$) 2.04 (s, 12H, $ArCH_3$) 1.11 (s, 18H, $C(CH_3)_3$)

**22-s**. **21-s** (2.557 g, 3.82 mmol, 1 equiv) was dissolved in a 3:1 mixture of toluene:THF (20 mL) in a Schlenk tube The Schlenk tube was cooled to -78 °C. After the temperature had equilibrated, $^n$BuLi (3.37 mL, 8.41 mmol, 2.2 equiv) was added via syringe. The reaction was stirred for 1 h at -78 °C beore it was quickly transferred via cannula to a second Schlenk tube containing dichlorodimethylsilane (9.3 mL, 76.4 mmol, 20 equiv) in toluene (10 mL) at -78°C. The reaction mixture was allowed to slowly reach ambient temperature at which point volatiles were removed under vacuum. The residue was taken up in pentane, filtered through celite, and concentrated *in vacuo*. The product was collected as a white powder by precipitation from pentane. First precipitate (872 mg, 33 % yield). Additional precipitates can be collected. $^1$H-NMR (300 MHz, $C_6D_6$ ): δ 8.13 (d, 2H, J = 2.6 Hz, Ar*H*) 7.34 (d, 2H, J = 2.6 Hz, Ar*H*) 5.61 (ddt, 2H, J = 17.2, 10.4, 5.1 Hz, $OCH_2C\mathit{H}=CH_2$) 5.11 (dd, 2H, J = 17.2, 1.7 Hz, $OCH_2CH=C\mathit{H}_2$) 4.88 (dd, 2H, J = 10.5, 1.6 Hz, $OCH_2CH=C\mathit{H}_2$) 4.14-4.07 (m, 4H, $OC\mathit{H}_2CH=CH_2$) 2.12 (s, 12H, $ArC\mathit{H}_3$) 1.30 (s, 18H, $C(C\mathit{H}_3)_3$) 0.79 (s, 12H, $Si\text{-}C\mathit{H}_3$) ppm.

**2-s**. **22-s** (0.861 g, 1.24 mmol, 1 equiv) was dissolved in THF (5 mL) and added to a suspension of lithium tetramethylcyclopentadienyl (0.333 g, 2.60 mmol, 2.1 equiv) in THF (10 mL). The reaction mixture was stirred for 12 h before filtering through celite, concentrating, taking up in pentane and filtering again through celite. The product (0.950 g, 89 % yield) was carried on without further purification. $^1$H NMR (300 MHz, $C_6D_6$) δ 7.62 (d, *J* = 2.6 Hz, 2H), 7.29 (d, *J* = 2.6 Hz, 2H), 5.91 – 5.57 (m, 2H), 5.28 (dd, *J* = 17.2, 1.8 Hz, 2H), 4.97 (dd, *J* = 10.6, 1.7 Hz, 2H), 4.22 (d, *J* = 4.9 Hz, 4H), 3.72 (s, 1H), 2.21 (s, 12H), 1.97 (s, 12H), 1.91 (s, 12H), 1.29 (s, 18H), 0.42 (s, 12H)

**3-s.** Metalation of **2-s** was accomplished by taking **2-s** (0.200 g, 0.23 mmol, 1 equiv.) up in 10 mL of diethyl ether and cooling to -35 °C at which time, nBuLi (380 μL, 0.95 mmol, 4.1 equiv.) was added by syringe. The mixture was allowed to warm to ambient temperature and stirred for 3 hours. Volatiles were removed *in vacuo*. The remaining material was dissolved in 20 mL of THF. This solution was added cold (-35 °C) to a solution of $TiCl_4(THF)_2$ (0.154 g, 0.46 mmol, 2.0 equiv.) in 20 mL of THF at -35 °C. The mixture was allowed to reach ambient temperature and then was heated in a 95 °C oil bath for 4 hours. Volatiles were removed *in vacuo*. The material was taken up in 20 mL of pentane and filtered through celite to remove lithium salts. The material was isolated by crystallization from pentane/hexamethyldisiloxane (15 mg, 6.4 % yield) $^1$H NMR (300 MHz, $C_6D_6$ ): δ ppm. 7.63 (d, 2H, J = 2.5 Hz, ArH) 7.37 (d, 2H, J = 2.4 Hz, ArH) 2.28 (s, 12H, $ArCH_3$) 1.98 (s, 12H, $Cp^*Me$) 1.95 (s, 12H, $Cp^*Me$) 1.31 (s, 18H, $C(CH_3)_3$) 0.53 (s, 12H, $Si\text{-}CH_3$)

**8-s.** The titanium dichloride complex **3-s** (8.4 mg, 0.008 mmol) was dissolved in 5 mL diethyl ether and cooled to -35 °C. A second solution of dimethylmagnesium(tetramethylethylenediamine) (2.72 mg, 0.016 mmol) was prepared by dissolving the material in 5 mL of diethyl ether and cooling to -35 °C . The solution containing the titanium complex was added to the second solution and warmed to room temperature. The mixture was stirred for one hour before removing volatiles *in vacuo*. The material was taken up

in pentane and filtered through Celite to remove magnesium salts. The product was isolated as colorless oil. (8 mg, 90%) $^1$H NMR (300 MHz, $C_6D_6$) δ 7.64 (s, 2H, ArH) 7.44 (s, 2H, ArH) 2.34 (s, 12H, $ArCH_3$) 1.88 (s, 12H, $Cp^*Me$) 1.74 (s, 12H, $Cp^*Me$) 1.37 (s, 18H, $C(CH_3)_3$) 0.59 (s, 12H, $TiCH_3$) 0.51 (s, 12H, $SiCH_3$)

*Synthesis of bisphenoxycyclopentadienyl compounds (meta – Scheme 4)*

**11-a** and **11-s**. Synthesis of the biphenyl compounds **12** was accomplished via the Negishi coupling of 1,3-dibromomesitylene (5.488 g, 19.74 mmol, 0.48 equiv.) with 2-bromo-4-*tert*-butylmethoxybenzene (10.000 g, 41.13 mmol, 1 equiv.) using conditions analogous to the synthesis of compounds **1**. Anti and syn isomers generated in the coupling reaction were not separated and instead were carried on together. (5.571 g, 63 % yield) $^1$H NMR (300 MHz, $CDCl_3$): δ ppm. 7.34 (dd, 2H, J = 8.6, 2.6 Hz, ArH) 7.17 (d, 2H, J = 2.5 Hz, ArH) 7.11 (s, 1H, ArH) 6.92 (d, 2H, J = 8.5 Hz, ArH) 2.73 (s, 6H, $OCH_3$-anti) 2.84 (s, 6H, $OCH_3$-syn) 2.06 (s, 6H, $ArCH_3$) 1.71 (s, 3H, $ArCH_3$) 1.330 (s, 18 H, $C(CH_3)_3$ – anti) 1.326 (s, 18 H, $C(CH_3)_3$ – anti)

**12-a**. A mixture of **11-a** and **11-s** (5.591 g, 12.53 mmol, 1 equiv.) was dissolved in 100 mL of dichloromethane and cooled to 0 °C. Neat boron tribromide (4.75 mL, 50.12 mmol, 4 equiv.) was added to the solution. The reaction mixture was allowed to warm to ambient temperature and stirred for one hour. The mixture was quenched with saturated sodium bicarbonate solution. The organic fraction was collected, contacted with $MgSO_4$, filtered through celite, and concentrated *in vacuo*. The syn and anti isomers were isolated by flash column chromatography on silica gel. 5:1:1/2 hexanes:ethyl acetate: DCM. $^1$H NMR (300 MHz, $CDCl_3$): δ ppm. 7.29 (dd, 2H, J = 8.5, 2.5 Hz, ArH) 7.17 (s, 1H, ArH) 7.04 (d, 2H, J = 2.5 Hz, ArH) 6.92 (d, 2H, J = 8.5 Hz, ArH) 4.55 (s, 2H, OH) 2.07 (s, 6H, $ArCH_3$) 1.75 (s, 3H, $ArCH_3$) 1.30 (s, 18 H, $C(CH_3)_3$)

**12-s**. The syn isomer was collected as the slower eluting fraction of the silica flash column described for **19-s**. $^1$H NMR (300 MHz, $CDCl_3$): δ ppm. 7.24 (dd, 2H, J = 8.5, 2.5 Hz, ArH) 7.15 (s, 1H, ArH) 7.07 (d, 2H, J = 2.5 Hz, ArH) 6.86 (d, 2H, J = 8.5 Hz, ArH) 5.02 (br, 2H, OH) 2.07 (s, 6H, $ArCH_3$) 1.69 (s, 3H, $ArCH_3$) 1.29 (s, 18 H, $C(CH_3)_3$)

**13-s**. The desired material was prepared utilizing a procedure identical to that for **20-s** with **12-s** (1.753 g, 4.21 mmol, 1 equiv.) and bromine (423 μL, 8.21 mmol, 1.95 equiv.) The product was isolated by flash column chromatography on silica gel 5:1:1/2 hexanes:ethyl acetate: DCM (2.489 g, quantitative yield) $^1$H NMR (300 MHz, $CDCl_3$): δ ppm. 7.48 (d, 2H, J = 2.3 Hz, ArH) 7.17 (s, 1H, ArH) 7.07 (d, 2H, J = 2.3 Hz, ArH) 5.31 (s, 2H, ArOH) 2.08 (s, 6H, $ArCH_3$) 1.75 (s, 3H, $ArCH_3$) 1.30 (s, 18 H, $C(CH_3)_3$)

**14-s**. The desired material was prepared utilizing a procedure identical to that for **21-s** with **13-s** (2.489 g, 4.3 mmol, 1 equiv.) allyl bromide (3.7 mL, 43 mmol, 10 equiv.) and sodium hydroxide (1.72 g, 43 mmol, 10 equiv.) The product was isolated by flash column chromatography on silica gel 30:1 hexanes:ethyl acetate (2.2 g, 78% yield) $^1$H NMR (300 MHz, $C_6D_6$): δ ppm. 7.68 (d, 2H, J = 2.5 Hz, ArH) 7.11 (s, 1H, ArH) 6.98 (d, 2H, J = 2.5 Hz, ArH)

5.87 (ddt, 2H, J = 17.2, 10.6, 5.4 Hz, $OCH_2CH=CH_2$) 5.24 (ddd, 2H, J = 17.2, 3.3 1.6 Hz, $OCH_2CH=CH_2$) 4.97 (m, 2H, $OCH_2CH=CH_2$) 4.24 (m, 4H, $OCH_2CH=CH_2$) 2.14 (s, 6H, $ArCH_3$) 2.09 (s, 3H, $ArCH_3$) 1.04 (s, 18 H, $C(CH_3)_3$)

**15-s**. The desired material was prepared utilizing a procedure identical to that for **22-s** with **14-s** (1.000 g, 1.53 mmol, 1 equiv.) nBuLi (1.34 mL, 3.36 mmol, 2.2 equiv.) and dichlorodimethylsilane (1.9 mL, 15.3 mmol, 10 equiv.) The product was used without further purification (720 mg, 69 % yield) $^1$H NMR (300 MHz, $C_6D_6$): δ ppm. 8.08 (d, 2H, J = 2.4 Hz, ArH) 7.34 (d, 2H, J = 2.4 Hz, ArH) 7.02 (s, 1H, ArH) 5.63 (ddd, 2H, J = 22.2, 10.3, 5.0 Hz, $OCH_2CH=CH_2$) 5.13 (dd, 2H, J = 17.2, 1.5 Hz, $OCH_2CH=CH_2$) 4.91 (dd, 2H, J = 10.5, 1.3 Hz, $OCH_2CH=CH_2$) 4.09 (d, 4H, J = 4.9 Hz, $OCH_2CH=CH_2$) 2.21 (s, 6H, $ArCH_3$) 2.21 (s, 3H, $ArCH_3$) 1.22 (s, 18 H, $C(CH_3)_3$) 0.75 (s, 6H, $SiCH_3$) 0.73 (s, 6H, $SiCH_3$)

**16-s**. **15-s** (0.500 g, 0.73 mmol, 1 equiv) was dissolved in THF (10 mL) and added to a suspension of lithium tetramethylcyclopentadienyl (0.207 g, 1.1 mmol, 2.2 equiv) in THF (10 mL). The reaction mixture was stirred for 12 h before filtering through celite, concentrating, taking up in pentane, and filtering again through celite. The product (0.590 g, 95 % yield) was carried on without further purification. $^1$H NMR (300 MHz, $C_6D_6$): δ ppm. 7.59 (d, 2H, J = 2.5 Hz, ArH) 7.31 (d, 2H, J = 2.5 Hz, ArH) 7.05 (s, 1H, ArH) 5.75 (ddd, 2H, J = 15.4, 10.1, 4.7 Hz, $OCH_2CH=CH_2$) 5.31 (dd, 2H, J = 17.3, 1.6 Hz, $OCH_2CH=CH_2$) 5.00 (dd, 2H, J = 10.6, 1.4 Hz, $OCH_2CH=CH_2$) 4.25 (d, 4H, J = 4.7 Hz, $OCH_2CH=CH_2$) 3.69 (s, 2H, $Cp^*H$) 2.34 (s, 3H, $ArCH_3$) 2.30 (s, 6H, $ArCH_3$) 1.92 (s, 12H, $Cp^*CH_3$) 1.88 (s, 12H, $Cp^*CH_3$) 1.22 (s, 18 H, $C(CH_3)_3$) 0.39 (s, 6H, $SiCH_3$) 0.37 (s, 6H, $SiCH_3$)

(**3d**) 2,4-di-*tert*-butyl-1-(methoxymethoxy)benzene. In a 500 mL 3-neck round bottom flask, 2,4-ditertbutylphenol (20.6g, 100 mmol) was dissolved in 200 mL of wet dichloromethane. This solution was stirred and a 2.1 M solution of MOMCl (95 mL, 200 mmol) was added. Next, (26 mL, 150 mmol) of diisopropylethylamine was syringed into the reaction mixture. Upon addition, the solution darkened and fumed. The reaction was stirred open to atmosphere for 48 hours and was checked periodically by GC-MS. The reaction mixture was pumped down to an oil and extracted between DCM and water. The organic layer was washed with sodium bicarbonate. The organic fraction was collected, contacted with $MgSO_4$, filtered through celite, and concentrated *in vacuo*. The product was purified by Kugelrohr distillation to give an off white solid (100 mTorr, 65°C) $^1$H-NMR (300 MHz, $CDCl_3$): δ 7.34 (d, 1H, J = 2.4 Hz, Ar-**H**) 7.16 (dd, 1H, J = 2.4 Hz, J = 8.4 Hz, Ar-**H**) 7.04 (d, 1H, J = 8.4, Ar-**H**) 5.22 (s, 2H, $OC\mathbf{H}_2O$) 3.50 (s, 3H, $OC\mathbf{H}_3$) 1.41 (s, 9H, $C(C\mathbf{H}_3)_3$) 1.31 (s, 9H, $C(C\mathbf{H}_3)_3$

(**3c**) chloro(3,5-di-*tert*-butyl-2-(methoxymethoxy)phenyl)dimethylsilane. Compound **3d** (2.000g, 7.99 mmol) was dissolved in approximately 20 mL of tetrahydrofuran in a 100 mL schlenk tube. This schlenk tube was cooled to -78°C. To this solution was added nBuLi (3.52mL, 8.79 mmol, 2.5M in pentane) by syringe. The solution was allowed to slowly reach room temperature. The schlenk was again cooled to -78°C and the contents were transferred to a second schlenk tube containing dichlorodimethylsilane (2.9 mL, 24.0 mmol) in approximately 10 mL at -78°C. The solution was allowed to warm to ambient temperature slowly and allowed to stir for several more hours. The reaction mixture was pumped down and brought into an inert atmosphere box. The residue was extracted with pentane and filtered through celite. Crystallization from pentane yielded pale yellow crystals $^1$H-NMR (300 MHz, $CDCl_3$): δ 7.52 (d,

1H, J = 2.5 Hz, Ar-**H**) 7.50 (d, 1H, J = 2.5 Hz, Ar-**H**) 5.05 (s, 2H, OC**H**$_2$O) 3.59 (s, 3H, OC**H**$_3$) 1.43 (s, 9H, C(C**H**$_3$)$_3$) 1.32 (s, 9H, C(C**H**$_3$)$_3$) 0.77 (s, 6H, Si(C**H**$_3$)$_2$

(**3b**) (3,5-di-*tert*-butyl-2-(methoxymethoxy)phenyl)dimethyl(2,3,4,5-tetramethylcyclopenta-2,4-dien-1-yl)silane. Previously prepared **3c** (100mg, 0.29 mmol) was dissolved in approximately 4 mL of THF and cooled to -35°C. **LiCp$^{4Me}$**(37 mg, 0.29 mmol) was suspended in approximately two mL of THF and cooled to -35°C. As quickly as possible, the solution of **3c** was pipetted into the suspended lithium salt. The mixture was allowed to reach ambient temperature. Over 24 hours, the mixture changed from heterogeneous to colorless and homogeneous. The final solution was pumped down. The residue was extracted with pentane and filtered through celite. 111 mg 90%. $^1$H-NMR (300 MHz, $CDCl_3$): δ 7.44 (dd, 1H, J = 2.4, Ar-**H**) 7.29 (dd, 1H, J = 2.4 Hz, Ar-**H**) 5.14 (s, 2H, OC**H**$_2$O) 3.69 (s, 3H, OC**H**$_3$) 3.62 (br, 1H, cp-**H**) 1.85 (s, 6H, cp-C**H**$_3$) 1.73 (s, 6H, cp-C**H**$_3$) 1.50 (s, 9H, C(C**H**$_3$)$_3$) 1.35 (s, 9H, C(C**H**$_3$)$_3$) 0.22 (s, 6H, Si(C**H**$_3$)$_2$

(**3a**) (1-((3,5-di-*tert*-butyl-2-(methoxymethoxy)phenyl)dimethylsilyl)-2,3,4,5-tetramethylcyclopenta-2,4-dien-1-yl)lithium: **3b** (200mg, 0.47 mmol) was dissolved in approximately 5 mL of diethyl ether. Next, nBuLi was slowly syringed into the mixture at ambient temperature. Over 5 minutes, the mixture became slightly opaque. The mixture was allowed to stir for 2 hours before pumping off the volatiles and extracting the residue in pentane. A cold precipitation from pentane gave a brilliant white powder. $^1$H-NMR (300 MHz, $CDCl_3$): δ 7.51 ppm (d, 1H, J = 2.7 Hz, Ar-**H**) 7.31 (d, 1H, J = 2.7 Hz, Ar-**H**) 4.80 ((s, 2H, OC**H**$_2$O) 3.45 (s, 3H, OC**H**$_3$) 1.97 (s, 6H, cp-C**H**$_3$) 1.91 (s, 6H, cp-C**H**$_3$) 1.33 (s, 9H, C(C**H**$_3$)$_3$) 1.31 (s, 9H, C(C**H**$_3$)$_3$) 0.56 (s, 6H, Si(C**H**$_3$)$_2$

(**3E**) 2-bromo-4,6-di-*tert*-butylphenol: 2,4-ditertbutyl-phenol (20g, 96.9 mmol) was dissolved in 300 mL of wet dichloromethane and cooled to 0°C. Bromine (5 mL, 96.9 mmol) was dissolved in 100 mL of DCM and transferred to an addition funnel. The bromine solution was slowly added over approximately one hour. The reaction mixture was allowed to warm to ambient temperature and stirred for 12 hours. 300 mL of water was added to the mixture and stirring was continued for several hours. The organic fraction was collected, contacted with $MgSO_4$, filtered through celite, and concentrated *in vacuo*. The material was purified further by Kugelrohr distillation (100 mTorr, 70°C). 13.348 g 96% $^1$H-NMR (300 MHz, $CDCl_3$): δ 7.32 ppm (d, 1H, J = 2.4 Hz, Ar-**H**) 7.24 (d, 1H, J = 2.4 Hz, Ar-**H**) 5.65 (s, 1H, ArO**H**) 1.40 (s, 9H, C(C**H**$_3$)$_3$) 1.28 (s, 9H, C(C**H**$_3$)$_3$)

(**3D**) 2-(allyloxy)-1-bromo-3,5-di-*tert*-butylbenzene: Phenol (**3E**) (5g, 17.5 mmol) was dissolved in about 100 mL of acetone. Allyl bromide (1.67 mL, 19.3 mmol) was syringed into the solution. A second flask was prepared with sodium hydroxide (771 mg, 19.3 mmol) dissolved in approximately 5 mL of water. The acetone solution of phenol was transferred to an addition funnel and slowly added to the sodium hydroxide solution. The mixture was allowed to stir overnight. Volatiles were pumped off and the residue was extracted with toluene, contacted with $MgSO_4$, filtered through celite, and concentrated *in vacuo*. The material was purified by kugelrohr distillation (100 mTorr, 70°C) $^1$H-NMR (300 MHz, $CDCl_3$): δ 7.42 (d, 1H, 2.4 Hz, Ar-**H**) 7.32 (d, 1H, 2.4 Hz, Ar-**H**) 6.15 (ddt, 1H, J = 17.2, 10.4, 5.1 Hz, $OCH_2C\mathbf{H}CH_2$) 5.57-5.42 (m, 1H, $OCH_2CHC\mathbf{H}_2$) 5.33-5.28 (m, 1H, $OCH_2CHC\mathbf{H}_2$) 4.59 (m, 2H, OC**H**$_2$CHCH$_2$) 1.40 (s, 9H, C(C**H**$_3$)$_3$) 1.30 (s, 9H, C(C**H**$_3$)$_3$)

(**3C**) (2-(allyloxy)-3,5-di-*tert*-butylphenyl)chlorodimethylsilane: Previously prepared **3D** (2.000g, 6.15 mmol) was dissolved in ~ 20 mL of dry toluene and cooled to -78°C. nBuLi (2.7 mL, 6.76 mmol, 2.5M in pentane) was added by syringe. Stirred one hour at -78°C before warming to -20°C. This solution was cannula transferred to a solution of dichlorodimethylsilane (2.24 mL, 18.35 mmol) in toluene at -20°C. The mixture was warmed to ambient temperature and stirred for several hours. Volatiles were removed

under vacuum and the schlenk tube was brought into an inert atmosphere box. The residue was extracted with pentane, filtered through celite, and cooled to -35°C. Colorless crystals grew and were collected by decanting away the mother liquor and washing with cold pentane. The first crop of crystals yielded 430 mg of material 20.6 %. Additional crops of crystals can be grown from the mother liquor. $^1$H-NMR (300 MHz, $CDCl_3$): δ 7.51 (d, 1H, J = 2.4 Hz, Ar-**H**) 7.49 (d, 1H, J = 2.4 Hz, Ar-**H**) 6.05 (ddt, 1H, J = 17.3, 10.8, 4.4 Hz, $OCH_2C\mathbf{H}CH_2$) 5.51 (dq, 1H, J = 17.3, 1.9 Hz, $OCH_2CHC\mathbf{H}_2$) 5.29 (dq, 1H, J = 10.7, 1.9 Hz, $OCH_2CHC\mathbf{H}_2$) 4.45 (dt, 2H, J = 3.9, 1.9, $OC\mathbf{H}_2CHCH_2$) 1.40 (s, 9H, $C(C\mathbf{H}_3)_3$) 1.32 (s, 9H, $C(C\mathbf{H}_3)_3$) 0.74 (s, 6H, $Si(C\mathbf{H}_3)_2$)

(**3B**) (2-(allyloxy)-3,5-di-*tert*-butylphenyl)dimethyl(2,3,4,5-tetramethylcyclopenta-2,4-dien-1-yl)silane: Previously synthesized **3C** (435 mg, 1.28 mmol) was dissolved in approximately 3 mL of THF. This solution was pipetted into a suspension of **LiCp$^{4Me}$** (181 mg, 1.41 mmol) and stirred at ambient temperature for 24 hours. The reaction mixture was filtered through celite, pumped down, extracted with pentane, and again filtered through celite. This solution was concentrated *in vacuo* to yield a pale yellow-green solid. $^1$H-NMR (300 MHz, $CDCl_3$): δ 7.37 (d, 1H, J = 2.4 Hz, Ar-**H**) 7.24 (d, 1H, J = 2.4 Hz, Ar-**H**) 6.10-5.99 (m, 1H, $OCH_2C\mathbf{H}CH_2$) 5.54 (dd, 1H, J = 17.3, 1.9, $OCH_2CHC\mathbf{H}_2$) 5.28 (dd, 1H, J = 10.7, 1.8, $OCH_2CHC\mathbf{H}_2$) 4.43-4.38 (m, 2H, $OC\mathbf{H}_2CHCH_2$) 3.36 (br, 1H, cp-**H**) 1.78 (s, 6H, Cp-$C\mathbf{H}_3$) 1.66 (s, 6H, Cp-$C\mathbf{H}_3$) 1.40 (s, 9H, $C(C\mathbf{H}_3)_3$) 1.30 (s, 9H, $C(C\mathbf{H}_3)_3$) 0.15 (s, 6H, $Si(C\mathbf{H}_3)_2$)

(**3**) mono-$TiCl_2$ A solution of **3B** (473mg, 1.11 mmol) was prepared by dissolving **3B** in approximately 4 mL of diethyl ether. A solution of 2.5M nBuLi (490 μL, 1.23 mmol) was syringed into the solution of **3B** and stirred at ambient temperature for 2 hours. The reaction mixture was concentrated under vacuum and the residue was taken up in about 5 mL of toluene and added dropwise into a yellow suspension of $TiCl_4(THF)_2$ in 10 mL of toluene. A color change to deep maroon was immediately observed. This reaction mixture was heated to 90°C in a sealed schlenk tube for 12 hours. Over this period of time, the reaction mixture became a lighter yellow-red color. This mixture was pumped down, the residue was taken up in pentane, filtered through celite, and concentrated *in vacuo*. Multiple recrystallizations from cold pentane/toluene yielded a yellow needle-like material. $^1$H-NMR (300 MHz, $C_6D_6$): δ 7.54 (d, 1H, J = 2.4 Hz, Ar-**H**) 7.44 (d, 1H, J = 2.4 Hz, Ar-**H**) 1.95 (s, 6H, Cp-$C\mathbf{H}_3$) 1.88 (s, 6H, Cp-$C\mathbf{H}_3$) 1.57 (s, 9H, $C(C\mathbf{H}_3)_3$) 1.30 (s, 9H, $C(C\mathbf{H}_3)_3$) 0.38 (s, 6H, $Si(C\mathbf{H}_3)_2$)

2-bromo-4-(*tert*-butyl)-1-(methoxymethoxy)benzene: para-tertbutylphenol (20g, 133.1 mmol) was dissolved in 300 mL of wet DCM. This solution was cooled to 0°C. The flask was fitted with an addition funnel. To this addition funnel was added bromine (6.86 mL, 133.1 mmol) and 60 mL of DCM. Over approximately two hours, the bromine solution was added to the cooled reaction vessel. The reaction was allowed to slowly warm to room temperature. 500 mL of water was added and the mixture was stirred for an additional 4 hours. The organic fraction was collected, contacted with $MgSO_4$, filtered through celite, and concentrated *in vacuo*. The material was further purified by stirring over calcium hydride and then collecting by Kugelrohr distillation (100 mTorr, 60°C) $^1$H-NMR (300 MHz, $CDCl_3$): δ 7.54 (d, 1H, J = 2.1 Hz, Ar-**H**) 7.25 (dd, 1H, J = 8.7, 2.1, Ar-**H**) 7.08 (d, 1H, J = 8.7 Hz, Ar-**H**) 5.23 (s, 2H, $OC\mathbf{H}_2O$) 3.52 (s, 3H, $OC\mathbf{H}_3$) 1.29 (s, 9H, $C(C\mathbf{H}_3)_3$)

(**2f – syn plus anti**) (1*R*,1"*S*)-5,5"-di-*tert*-butyl-5'-methoxy-2,2"-bis(methoxymethoxy)-2',4',6'-trimethyl-1,1':3',1"-terphenyl: The two atropisomers were not separated at this step of the synthesis. 2-bromo-4-(*tert*-butyl)-1-(methoxymethoxy)benzene (5g, 18.30 mmol) was dissolved in 100 mL of THF and frozen in the cold well of an inert atmosphere box. To the thawing solution was added $^t$BuLi (22.6 mL, 38.44 mmol, 1.7M in pentane). This stirring mixture was allowed to reach room temperature before adding $ZnCl_2$ (1.75g, 12.81 mmol). This opaque mixture was stirred for approximately 3 hours before the addition of 3,5-dibromo-2,4,6-trimethylmethoxybenzene (2.54g, 8.24 mmol) followed by the addition of

palladium tetrakis triphenylphosphine (211 mg, 0.183 mmol) with the help of an additional 20 mL of THF. The flask was sealed and heated to 95°C for approximately 3 days. The reaction mixture was pumped down, extracted with dichloromethane, filtered through silica, and concentrated *in vacuo*. The desired product was purified by precipitation out of methanol as a mixture of both the syn and anti atropisomers.

(**2e-Syn**) (1*R*,1"*S*)-5,5"-di-*tert*-butyl-5'-methoxy-2',4',6'-trimethyl-[1,1':3',1"-terphenyl]-2,2"-diol As a mixture of both the syn and anti atropisomers **2f** (1.473g, 2.75 mmol) was suspended in ~100mL of methanol. Dichloromethane was added slowly until the mixture was homogeneous. A few drops of concentrated HCL were added and the reaction was stirred. After several hours a GCMS of an aliquot showed only a small amount of product formation. The reaction was heated to reflux overnight. The reaction mixture was pumped down, extracted with toluene/$H_2O$. The organic fraction was collected, contacted with $MgSO_4$, filtered through celite, and concentrated *in vacuo*. The two atropisomers were isolated by silica gel flash column chromatography (5:1:0.5) hexanes:EtOAc:DCM. Nearly quantitative yield. $^1$H-NMR (300 MHz, $CDCl_3$): δ 7.21 (dd, 2H, J = 8.5, 2.4 Hz, Ar-**H**) 7.04 (d, 2H, J = 2.4 Hz, Ar-**H**) 6.94 (d, 2H, J = 8.5 Hz, Ar-**H**) 5.21 (s, 2H, O**H**) 3.71 (s, 3H, OC**H**$_3$) 2.04 (s, 6H, Ar-C**H**$_3$) 1.60 (s, 3H, Ar-C**H**$_3$) 1.28 (s, 18H, C(C**H**$_3$)$_3$)

(**2e-Anti**) (1*R*,1"*S*)-5,5"-di-*tert*-butyl-5'-methoxy-2',4',6'-trimethyl-[1,1':3',1"-terphenyl]-2,2"-diol. $^1$H-NMR (300 MHz, $CDCl_3$): δ 7.30 (dd, 2H, J = 8.5, 2.4 Hz, Ar-**H**) 7.06 (d, 2H, J = 2.4 Hz, Ar-**H**) 6.92 (d, 2H, J = 8.5 Hz, Ar-**H**) 4.81 (s, 2H, O**H**) 3.78 (s, 3H, OC**H**$_3$) 2.07 (s, 6H, Ar-C**H**$_3$) 1.74 (s, 3H, Ar-C**H**$_3$) 1.32 (s, 18H, C(C**H**$_3$)$_3$)

(**2d-Syn**) (1*R*,1"*S*)-3,3"-dibromo-5,5"-di-*tert*-butyl-5'-methoxy-2',4',6'-trimethyl-[1,1':3',1"-terphenyl]-2,2"-diol: **2e**(400 mg, 0.90 mmol) was dissolved in ~ 5mL of dry dichloromethane and cooled to -78°C. A 0.5M solution of bromine (3.49 mL, 1.75 mmol) was added by syringe over 30 minutes. The mixture was stirred for one hour and then allowed to warm to ambient temperature and stirred for an additional hour. Water was added and stirred for several hours. The organic fraction was collected, contacted with $MgSO_4$, filtered through celite, and concentrated *in vacuo*. The product was collected as a pale yellow oil. Nearly quantitative yield. $^1$H-NMR (300 MHz, $CDCl_3$): δ 7.49 (d, 2H, J = 2.3 Hz, Ar-**H**) 7.07 (d, 2H, J = 2.3 Hz, Ar-**H**) 5.59 (s, 2H, O**H**) 3.80 (s, 3H, OC**H**$_3$) 2.05 (s, 6H, Ar-C**H**$_3$) 1.69 (s, 3H, Ar-C**H**$_3$) 1.31 (s, 18H, C(C**H**$_3$)$_3$)

(**2d-Anti**) (1*R*,1"*S*)-3,3"-dibromo-5,5"-di-*tert*-butyl-5'-methoxy-2',4',6'-trimethyl-[1,1':3',1"-terphenyl]-2,2"-diol: Same procedure as **2d**-Syn. $^1$H-NMR (300 MHz, $CDCl_3$): δ 7.50 (d, 2H, J = 2.3 Hz, Ar-**H**) 7.08 (d, 2H, J = 2.3 Hz, Ar-**H**) 5.24 (s, 2H, O**H**) 3.79 (s, 3H, OC**H**$_3$) 2.06 (s, 6H, Ar-C**H**$_3$) 1.72 (s, 3H, Ar-C**H**$_3$) 1.31 (s, 18H, C(C**H**$_3$)$_3$)

(**2c-Anti**) (1*S*,3'*S*)-2,2"-bis(allyloxy)-3,3"-dibromo-5,5"-di-*tert*-butyl-5'-methoxy-2',4',6'-trimethyl-1,1':3',1"-terphenyl: **2d**-Anti (251 mg, 0.42 mmol) was dissolved in 20 mL of acetone. Allyl bromide (79 μL, 0.91 mmol) was added by syringe. This mixture was added to a solution of sodium hydroxide (36mg, 0.91 mmol) in 1 mL of water. The reaction mixture was stirred for 24 hours before pumping off volatiles. The residue was extracted with toluene, dried with $MgSO_4$, filtered through celite, and concentrated *in vacuo*. $^1$H-NMR (300 MHz, $CDCl_3$): δ 7.53 (d, 2H, J = 2.4, Ar-**H**) 6.98 (dd, 2H, J = 2.4, 0.4 Hz, Ar-**H**) 5.72 (ddt, 2H, J = 10.9, 6.0 5.4 Hz, $OCH_2C$**H**$=CH_2$) 5.05 (m, 4H, $OCH_2CH=C$**H**$_2$) 4.10 (m, 4H, OC**H**$_2$$CH=CH_2$) 3.72 (s, 3H, $OCH_3$) 2.04 (s, 6H, Ar-C**H**$_3$) 1.70 (s, 3H, Ar-C**H**$_3$) 1.29 (s, 18H, C(C**H**$_3$)$_3$)

(**2c-Syn**) 1*S*,3'*S*)-2,2"-bis(allyloxy)-3,3"-dibromo-5,5"-di-*tert*-butyl-5'-methoxy-2',4',6'-trimethyl-1,1':3',1"-terphenyl: The same procedure was used as **2c**-Anti except 10 equivalents of sodium hydroxide and allyl

bromide were used instead and the reaction was allowed to progress for 48 hours. $^1$H-NMR (300 MHz, $CDCl_3$): δ 7.54 (d, 2H, J = 2.4, Ar-**H**) 7.07 (d, 2H, J = 2.4 Hz, Ar-**H**) 5.76 (m, 2H, $OCH_2C\mathbf{H}=CH_2$) 5.20-5.03 (m, 4H, $OCH_2CH=C\mathbf{H}_2$) 4.06 (m, 4H, $OC\mathbf{H}_2CH=CH_2$) 3.75 (s, 3H, $OCH_3$) 2.07 (s, 6H, Ar-$C\mathbf{H}_3$) 1.73 (s, 3H, Ar-$C\mathbf{H}_3$) 1.29 (s, 18H, $C(C\mathbf{H}_3)_3$)

(**2b-anti**) **2c-anti** (122 mg, 0.18 mmol) was dissolved in 5 mL of a mixture of 5:1 Toluene:THF and cooled to -78 °C. nBuLi (2.5 M, 148 μL) was syringed in and stirred for two hours at low temperature. This mixture was cannula transferred to a mixture of dichlorodimethylsilane (8.91 mmol, 1.08 mL). This mixture was allowed to warm slowly to ambient temperature over 8 hours. The volatiles were removed *in vacuo***.** The residue was taken up in pentane and filtered through celite. 127 mg 98% yield. $^1$H-NMR (300 MHz, $C_6D_6$): δ 8.14 (s, 2H, Ar-**H**) 7.45 (s, 2H, Ar-**H**) 5.72-5.48 (m, 2H, $OCH_2C\mathbf{H}=CH_2$) 5.12 (d, 2H, J = 17.1 Hz, $OCH_2CH=C\mathbf{H}_2$) 4.95 (d, 2H, J = 10.3 Hz, $OCH_2CH=C\mathbf{H}_2$) 4.14 (s, 4H, $OC\mathbf{H}_2CH=CH_2$) 3.56 (s, 3H, $OCH_3$) 2.36 (s, 6H, Ar-$C\mathbf{H}_3$) 2.25 (s, 3H, Ar-$C\mathbf{H}_3$) 1.33 (s, 18H, $C(C\mathbf{H}_3)_3$) 0.77 (s, 6H, Si**Me**) 0.75 (s, 6H, Si**Me**)

(**2b-syn**) The same procedure was used as for **2b-anti**. 502 mg 85% yield. $^1$H-NMR (300 MHz, $C_6D_6$): δ 8.10 (d, 2H, J = 2.6 Hz, Ar-**H**) 7.37 (d, 2H, J = 2.6 Hz, Ar-**H**) 5.76-5.48 (m, 2H, $OCH_2C\mathbf{H}=CH_2$) 5.12 (dd, 2H, J = 17.2, 1.7 Hz, $OCH_2CH=C\mathbf{H}_2$) 4.89 (dd, 2H, J = 10.6, 1.6 Hz, $OCH_2CH=C\mathbf{H}_2$) 4.23-3.99 (m, 4H, $OC\mathbf{H}_2CH=CH_2$) 3.50 (s, 3H, $OCH_3$) 2.33 (s, 6H, Ar-$C\mathbf{H}_3$) 2.19 (s, 3H, Ar-$C\mathbf{H}_3$) 1.22 (s, 18H, $C(C\mathbf{H}_3)_3$) 0.76 (s, 6H, Si**Me**) 0.73 (s, 6H, Si**Me**)

(**2a-anti**) **2b-anti** (122 mg, 0.18 mmol) was dissolved in 5 mL of a mixture of 5:1 Toluene:THF and cooled to -78 °C. nBuLi (2.5 M, 148 μL) was syringed in and stirred for two hours at low temperature. This mixture was cannula transferred to a mixture of dichlorodimethylsilane (8.91 mmol, 1.08 mL). This mixture was allowed to warm slowly to ambient temperature over 8 hours. The volatiles were removed *in vacuo***.** The residue was taken up in pentane and filtered through celite. 250 mg 73% yield. $^1$H-NMR $^1$H-NMR (300 MHz, $C_6D_6$): δ 7.60 (d, 2H, J = 2.6 Hz, Ar-**H**) 7.38 (d, 2H, J = 2.6 Hz, Ar-**H**) 5.78-5.58 (m, 2H, $OCH_2C\mathbf{H}=CH_2$) 5.24 (dd, 2H, J = 17.2, 1.8 Hz, $OCH_2CH=C\mathbf{H}_2$) 4.99 (dd, 2H, J = 10.5, 1.8 Hz, $OCH_2CH=C\mathbf{H}_2$) 4.30-4.12 (m, 4H, $OC\mathbf{H}_2CH=CH_2$) 3.62 (s, 3H, $OCH_3$) 3.55 (s, 2H, Cp-**H**) 2.40 (s, 6H, Ar-$C\mathbf{H}_3$) 2.32 (s, 3H, Ar-$C\mathbf{H}_3$) 1.93 (s, 12H, Cp-**Me**) 1.87 (s, 12H, Cp-**Me**) 1.29 (s, 18H, $C(C\mathbf{H}_3)_3$) 0.38 (s, 6H, Si**Me**) 0.35 (s, 6H, Si**Me**)

(**2a-syn**) The same procedure was used as for **2b-anti**. 450 mg 74% yield. $^1$H-NMR (300 MHz, $C_6D_6$): δ 7.61 (d, 2H, J = 2.6 Hz, Ar-**H**) 7.33 (d, 2H, J = 2.5 Hz, Ar-**H**) 5.89-5.58 (m, 2H, $OCH_2C\mathbf{H}=CH_2$) 5.29 (dd, 2H, J = 17.1, 1.8 Hz, $OCH_2CH=C\mathbf{H}_2$) 4.98 (dd, 2H, J = 10.3, 1.7 Hz, $OCH_2CH=C\mathbf{H}_2$) 4.23 (s, 4H, $OC\mathbf{H}_2CH=CH_2$) 3.68 (s, 3H, $OCH_3$) 3.55 (s, 2H, Cp-**H**) 2.41 (s, 6H, Ar-$C\mathbf{H}_3$) 2.32 (s, 3H, Ar-$C\mathbf{H}_3$) 1.93 (s, 12H, Cp-**Me**) 1.88 (s, 12H, Cp-**Me**) 1.23 (s, 18H, $C(C\mathbf{H}_3)_3$) 0.40 (s, 6H, Si**Me**) 0.37 (s, 6H, Si**Me**)

(**1f-syn** and **1f-anti**) 5,5"-di-*tert*-butyl-2,2"-dimethoxy-2',3',5',6'-tetramethyl-1,1':4',1"-terphenyl: 2-bromo-4-$^t$Bu-methoxybenzene (10g, 41.1 mmol) was dissolved in 80 mL of THF and frozen in the cold well of an inert atmosphere box. To the thawing solution was added $^t$BuLi (50.8mL, 86.3 mmol, 1.7M in pentane). This stirring mixture was allowed to reach room temperature before adding $ZnCl_2$ (3.92g, 28.77 mmol). This opaque mixture was stirred for approximately 3 hours before the addition of 1,4-dibromo-2,3,5,6-tetramethylbenzene (5.40g, 18.50 mmol) followed by the addition of palladium tetrakis triphenylphosphine (475 mg, 0.411 mmol) with the help of an additional 20 mL of THF. Heated to 90$^o$C for 2 days after which the yellow color in the solution disappeared, leaving an opaque black solution. The reaction mixture was pumped down, extracted with DCM, filtered through celite, and concentrated *in vacuo*. The residue was taken up in methanol and cooled to -35$^o$C. What precipitated was only the anti-atropisomer. Additional precipitations afforded mixtures of the syn and anti-isomers. (**1f-anti**) 5,5"-di-

*tert*-butyl-2,2"-dimethoxy-2',3',5',6'-tetramethyl-1,1':4',1"-terphenyl (**1f**-anti): see the procedure for **1f**-syn. $^1$H-NMR (300 MHz, $CDCl_3$): δ 7.33 (dd, 2H, J = 8.6, 2.6 Hz, Ar-**H**) 7.16 (d, 2H, J = 2.6 Hz, Ar-**H**) 6.92 (d, 2H, J = 8.6 Hz, Ar-**H**) 3.76 (s, 6H, OC**H**$_3$) 1.96 (s, 12H, Ar-C**H**$_3$) 1.32 (s, 18H, C(C**H**$_3$)$_3$)

(**1e-anti**) 5,5"-di-*tert*-butyl-2',3',5',6'-tetramethyl-[1,1':4',1"-terphenyl]-2,2"-diol (**1e**-anti): **1f**-anti (1.222g, 2.66 mmol) was dissolved in 20 mL of DCM and cooled to 0°C. $BBr_3$ (2 mL, 21.1 mmol) was syringed in. The reaction mixture was stirred for 1 hour and then allowed to warm to room temperature. The reaction was quenched with sodium bicarbonate. The organic fraction was collected, contacted with $MgSO_4$, filtered through celite, and concentrated *in vacuo*. 1.094g 96%. $^1$H-NMR (300 MHz, $CDCl_3$): δ 7.31 (dd, 2H, J = 8.4, 2.4 Hz, Ar-**H**) 7.05 (d, 2H, J = 2.4 Hz, Ar-**H**) 6.94 (d, 2H, J = 8.5 Hz, Ar-**H**) 4.52(s, 2H, O**H**) 1.99 (s, 12H, Ar-C**H**$_3$) 1.32 (s, 18H, C(C**H**$_3$)$_3$)

(**1d-anti**) 3,3"-dibromo-5,5"-di-*tert*-butyl-2',3',5',6'-tetramethyl-[1,1':4',1"-terphenyl]-2,2"-diol (**1d**-Anti): See the procedure for **2d**-anti. $^1$H-NMR (300 MHz, $CDCl_3$): δ 7.49 (d, 2H, J = 2.3 Hz, Ar-**H**) 7.07 (d, 2H, J = 2.3 Hz, Ar-**H**) 5.20(s, 2H, O**H**) 1.98 (s, 12H, Ar-C**H**$_3$) 1.31 (s, 18H, C(C**H**$_3$)$_3$)

(**1c-anti**) 2,2"-bis(allyloxy)-3,3"-dibromo-5,5"-di-*tert*-butyl-2',3',5',6'-tetramethyl-1,1':4',1"-terphenyl (**1c**-Anti): See the procedure for **2c**-anti. The product was purified by crystallization from DCM/hexane. The first crop yielded 930mg 55%. Additional crops of crystals can be collected. $^1$H-NMR (300 MHz, $CDCl_3$): δ 7.55 (d, 2H, J = 2.4 Hz, Ar-**H**) 6.99 (d, 2H, J = 2.4 Hz, Ar-**H**) 5.73 (m, 2H, $OCH_2C$**H**$=CH_2$) 5.05(m, 4H, $OCH_2CH=C$**H**$_2$) 4.08 (m, 4H, OC**H**$_2CH=CH_2$) 1.96 (s, 12H, Ar-C**H**$_3$) 1.32 (s, 18H, C(C**H**$_3$)$_3$)

(**1b-anti**) **1c-anti** (93mg, 0.14 mmol) was dissolved in 5 mL of toluene. One mL of THF was added to the reaction flask. The schlenk tube was cooled to -78°C. After the temperature had equilibrated, nBuLi (116 μL, 0.29 mmol, 2.5M in pentane) was syringed in. The reaction was stirred for one hour at reduced temperature. Then, the reaction mixture was cannula transferred to a schlenk tube containing dichlorodimethylsilane (361 μL, 2.8 mmol) dissolved in 5 mL of toluene at -78°C. The reaction mixture was allowed to slowly reach ambient temperature. The reaction mixture was pumped down. The residue was taken up in pentane, filtered through celite, and concentrated *in vacuo*. A product was a white powder. $^1$H-NMR (300 MHz, $C_6D_6$ ): δ 8.07 (d, 2H, J = 2.6 Hz, Ar-**H**) 7.30 (d, 2H, J = 2.6 Hz, Ar-**H**) 5.49 (m, 2H, $OCH_2C$**H**$=CH_2$) 4.87 (m, 4H, $OCH_2CH=C$**H**$_2$) 4.07 (m, 4H, OC**H**$_2CH=CH_2$) 2.12 (s, 12H, Ar-C**H**$_3$) 1.25 (s, 18H, C(C**H**$_3$)$_3$) 0.71 (s, 12H, Si-C**H**$_3$)

(**1a-Anti). 1b-Anti** (154 mg, 0.22 mmol) was dissolved in 5 mL of THF and added to a suspension of lithium tetramethylcyclopentadienyl (62.4 mg, 0.29) in THF. The mixture was stirred for 12 hours before filtering through celite, concentrating, taking up in pentane and filtering again through celite. The material was carried on without further purification. $^1$H-NMR 83% yield (300 MHz, $C_6D_6$ ): δ 7.62 (d, 2H, J = 2.5 Hz, Ar-**H**) 7.31 (d, 2H, J = 2.5 Hz, Ar-**H**) 5.66 (m, 2H, $OCH_2C$**H**$=CH_2$) 5.11 (d, 2H, J =15.6 Hz, $OCH_2CH=C$**H**$_2$) 5.11 (d, 2H, J = 10.4 Hz, $OCH_2CH=C$**H**$_2$) 4.23 (d, 4H, J = 5.1 Hz, OC**H**$_2CH=CH_2$) 3.68 (s, 1H, Cp*-**H**) 2.24 (s, 12H, Ar-C**H**$_3$) 1.95 (s, 12H, Cp*-**Me**) 1.90 (s, 12H, Cp*-**Me**) 1.30 (s, 18H, C(C**H**$_3$)$_3$) 0.40 (s, 12H, Si-C**H**$_3$)

(**1-Anti). 1a-Anti** (50 mg, 0.058 mmol) was dissolved in 5 mL of $Et_2O$ and cooled to -35 °C. To this solution was added nBuLi (2.5 M, 92μL). This solution as stirred for 2 hours at room temperature before pumping off the volatiles. This yellow residue was taken up in a mixture of 3:1 Toluene:THF and cooled to -35 °C. This solution was added to a solution of $TiCl_4(THF)_2$ in Toluene at -35 °C. The mixture became dark red-orange and was stirred at room temperature for 1 hour before heating to 95 °C for one hour. The volatiles were removed *in vacuo*. The red material was taken up in pentane and filtered through celite. The material was collected by precipitation from methanol. 25% yield $^1$H-NMR (300 MHz, $C_6D_6$

): δ 7.62 (d, 2H, J = 2.4 Hz, Ar-**H**) 7.54 (d, 2H, J = 2.4 Hz, Ar-**H**) 2.24 (s, 12H, Ar-C**H**$_3$) 1.91 (s, 12H, Cp*-**Me**) 1.90 (s, 12H, Cp*-**Me**) 1.34 (s, 18H, C(C**H**$_3$)$_3$) 0.49 (s, 12H, Si-C**H**$_3$)

(**1e-syn**). $^1$H-NMR (300 MHz, $CDCl_3$): δ 7.31 (dd, 2H, J = 8.5, 2.5 Hz, Ar-**H**) 7.06 (d, 2H, J = 2.4 Hz, Ar-**H**) 6.95 (d, 2H, J = 8.5 Hz, Ar-**H**) 4.53 (s, 6H, OC**H**$_3$) 2.01 (s, 12H, Ar-C**H**$_3$) 1.31 (s, 18H, C(C**H**$_3$)$_3$)

(**1d-syn**) 3,3''-dibromo-5,5''-di-*tert*-butyl-2',3',5',6'-tetramethyl-[1,1':4',1''-terphenyl]-2,2''-diol (**1d**-Anti): See the procedure for **2d**-anti. $^1$H-NMR (300 MHz, $CDCl_3$): δ 7.52 (d, 2H, J = 2.3 Hz, Ar-**H**) 7.05 (d, 2H, J = 2.3 Hz, Ar-**H**) 5.27 (s, 2H, O**H**) 2.00 (s, 12H, Ar-C**H**$_3$) 1.32 (s, 18H, C(C**H**$_3$)$_3$)

(**1c-syn**) 2,2''-bis(allyloxy)-3,3''-dibromo-5,5''-di-*tert*-butyl-2',3',5',6'-tetramethyl-1,1':4',1''-terphenyl (**1c**-Anti): See the procedure for **2c**-anti. $^1$H-NMR (300 MHz, $CDCl_3$): δ 7.59 (d, 2H, J = 2.4 Hz, Ar-**H**) 7.12 (d, 2H, J = 2.4 Hz, Ar-**H**) 5.75 (ddt, 2H, J = 17.1, 10.4, 5.6 Hz, $OCH_2C\mathbf{H}=CH_2$) 5.28-5.11 (m, 2H, $OCH_2CH=C\mathbf{H}_2$) 5.10-4.94 (m, 2H, $OCH_2CH=C\mathbf{H}_2$) 4.08 (dt, 4H, J = 5.6, 1.3 Hz, $OC\mathbf{H}_2CH=CH_2$) 2.03 (s, 12H, Ar-C**H**$_3$) 1.34 (s, 18H, C(C**H**$_3$)$_3$)

(**1b-syn**) **1c-anti** See procedure for **1b-anti.** $^1$H-NMR (300 MHz, $C_6D_6$ ): δ 8.13 (d, 2H, J = 2.5 Hz, Ar-**H**) 7.34 (d, 2H, J = 2.5 Hz, Ar-**H**) 5.61 (ddt, 2H, J = 17.2, 10.4, 5.1 Hz, $OCH_2C\mathbf{H}=CH_2$) 5.11 (dd, 2H, J = 17.2, 1.7 Hz, $OCH_2CH=C\mathbf{H}_2$) 4.88 (dd, 2H, J = 10.5, 1.6 Hz, $OCH_2CH=C\mathbf{H}_2$) 4.14-4.07 (m, 4H, $OC\mathbf{H}_2CH=CH_2$) 2.12 (s, 12H, Ar-C**H**$_3$) 1.30 (s, 18H, C(C**H**$_3$)$_3$) 0.79 (s, 12H, Si-C**H**$_3$)

(**1a-syn).** See the procedure for **1a-anti**. 83% yield. $^1$H NMR (300 MHz, $c_6d_6$) δ 7.62 (d, *J* = 2.6 Hz, 2H), 7.29 (d, *J* = 2.6 Hz, 2H), 5.91 – 5.57 (m, 2H), 5.28 (dd, *J* = 17.2, 1.8 Hz, 2H), 4.97 (dd, *J* = 10.6, 1.7 Hz, 2H), 4.22 (d, *J* = 4.9 Hz, 4H), 3.72 (s, 1H), 2.21 (s, 12H), 1.97 (s, 12H), 1.91 (s, 12H), 1.29 (s, 18H), 0.42 (s, 12H).

(**1-syn)** See the procedure for **1-anti.** The material was purified by vapor-diffusion of pentane out of HMDSO to yield yellow crystals. 10% yield $^1$H-NMR (300 MHz, $C_6D_6$ ): δ 7.63 (d, 2H, J = 2.5 Hz, Ar-**H**) 7.37 (d, 2H, J = 2.4 Hz, Ar-**H**) 2.28 (s, 12H, Ar-C**H**$_3$) 1.98 (s, 12H, Cp*-**Me**) 1.95 (s, 12H, Cp*-**Me**) 1.31 (s, 18H, C(C**H**$_3$)$_3$) 0.53 (s, 12H, Si-C**H**$_3$)

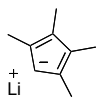


Lithium 2,3,4,5-tetramethylcyclopenta-2,4-dien-1-ide (**LiCp$^{4Me}$**) 1,2,3,4-tetramethyl-1,3-cyclopentadiene (1g, 8.18 mmol) was dissolved in 10 mL of pentane and cooled to -35°C. A solution of nBuLi (3.27 mL, 8.18 mmol) was prepared by dissolving the nBuLi in 3 mL of pentane and cooled to -35°C. The nBuLi solution was slowly added to the Cp-derivative. Initially, the mixture was homogeneous and clear but slowly became cloudy and eventually solidified. The material was pumped down and washed with pentane. What resulted was an off-white material that was incredibly insoluble in available NMR solvents so it was not further characterized.

## A.3 References

1. Ittel, S. D.; Johnson, L. K.; Brookhart, M., Late-Metal Catalysts for Ethylene Homo- and Copolymerization. *Chemical Reviews* **2000,** *100* (4), 1169-1204.

2. McGinty, K. M.; Brittain, W. J., Hydrophilic surface modification of poly(vinyl chloride) film and tubing using physisorbed free radical grafting technique. *Polymer* **2008,** *49* (20), 4350-4357.

3. Delferro, M.; Marks, T. J., Multinuclear Olefin Polymerization Catalysts. *Chemical Reviews* **2011,** *111* (3), 2450-2485.

4. Chen, E. Y. X., Coordination Polymerization of Polar Vinyl Monomers by Single-Site Metal Catalysts. *Chemical Reviews* **2009,** *109* (11), 5157-5214.

5. Motta, A.; Fragala , I. L.; Marks, T. J., Proximity and Cooperativity Effects in Binuclear d0 Olefin Polymerization Catalysis. Theoretical Analysis of Structure and Reaction Mechanism. *Journal of the American Chemical Society* **2009,** *131* (11), 3974-3984.

6. Noh, S. K.; Kim, S.; Yang, Y.; Lyoo, W. S.; Lee, D. H., Preparation of syndiotactic polystyrene using the doubly bridged dinuclear titanocenes. *European Polymer Journal* **2004,** *40* (2), 227-235.

7. Menger, F. M., Enzyme reactivity from an organic perspective. *Accounts of Chemical Research* **1993,** *26* (4), 206-212.

8. Krishnan, R.; Voo, J. K.; Riordan, C. G.; Zahkarov, L.; Rheingold, A. L., Thiolate-Bridged Nickel,àíCopper Complexes:,ÄâA Binuclear Model for the Catalytic Site of Acetyl Coenzyme A Synthase? *Journal of the American Chemical Society* **2003,** *125* (15), 4422-4423.

9. Kanady, J. S.; Tsui, E. Y.; Day, M. W.; Agapie, T., A Synthetic Model of the Mn3Ca Subsite of the Oxygen-Evolving Complex in Photosystem II. *Science* **2011,** *333* (6043), 733-736.

10. Radlauer, M. R.; Day, M. W.; Agapie, T., Bimetallic Effects on Ethylene Polymerization in the Presence of Amines: Inhibition of the Deactivation by Lewis Bases. *Journal of the American Chemical Society* **2012,** *134* (3), 1478-1481.

11. Radlauer, M. R.; Day, M. W.; Agapie, T., Dinickel Bisphenoxyiminato Complexes for the Polymerization of Ethylene and α-Olefins. *Organometallics* **2012**.

12. Hanaoka, H.; Hino, T.; Nabika, M.; Kohno, T.; Yanagi, K.; Oda, Y.; Imai, A.; Mashima, K., Synthesis and characterization of titanium alkyl, oxo, and diene complexes bearing a SiMe2-bridged phenoxy-cyclopentadienyl ligand and their catalytic performance for copolymerization of ethylene and 1-hexene. *Journal of Organometallic Chemistry* **2007,** *692* (21), 4717-4724.

13. Nabika, M.; Katayama, H.; Watanabe, T.; Kawamura-Kuribayashi, H.; Yanagi, K.; Imai, A., ansa-Cyclopentadienyl-Phenoxy Titanium(IV) Complexes (PHENICS): Synthesis, Characterization, and Catalytic Behavior in Olefin Polymerization. *Organometallics* **2009,** *28* (13), 3785-3792.

14. Hanaoka, H.; Hino, T.; Souda, H.; Yanagi, K.; Oda, Y.; Imai, A., Synthesis and characterization of titanium and zirconium complexes with silicone-bridged phenoxycyclopentadienyl ligands. *Journal of Organometallic Chemistry* **2007,** *692* (19), 4059-4066.

15. Senda, T.; Hanaoka, H.; Hino, T.; Oda, Y.; Tsurugi, H.; Mashima, K., Substituent Effects on Silicon of Bridged Tetramethylcyclopentadienyl-Phenoxy Titanium Complexes for Controlling the Regiochemistry and Molecular Weight in 1-Olefin Polymerization. *Macromolecules* **2009,** *42* (21), 8006-8009.

16. Senda, T.; Hanaoka, H.; Nakahara, S.; Oda, Y.; Tsurugi, H.; Mashima, K., Rational Design of Silicon-Bridged Fluorenyl,àíPhenoxy Group 4 Metal Complexes as Catalysts for Producing High Molecular Weight Copolymers of Ethylene and 1-Hexene at Elevated Temperature. *Macromolecules* **2010,** *43* (5), 2299-2306.

17. Senda, T.; Hanaoka, H.; Okado, Y.; Oda, Y.; Tsurugi, H.; Mashima, K., Titanium Complexes of Silicon-Bridged Cyclopentadienyl-Phenoxy Ligands Modified with Fused-Thiophene: Synthesis, Characterization, and Their Catalytic Performance in Copolymerization of Ethylene and 1-Hexene. *Organometallics* **2009,** *28* (24), 6915-6926.

18. Stopper, A.; Goldberg, I.; Kol, M., Bis(aniline-phenolate) complexes of group 4 metals: Coordination chemistry and lactide polymerization catalysis. *Inorganic Chemistry Communications* **2011,** *14* (5), 715-718.

19. Saha, T. K.; Ramkumar, V.; Chakraborty, D., Salen Complexes of Zirconium and Hafnium: Synthesis, Structural Characterization, Controlled Hydrolysis, and Solvent-Free Ring-Opening Polymerization of Cyclic Esters and Lactides. *Inorganic Chemistry* **2011,** *50* (7), 2720-2722.